https://doi.org/10.15388/vu.thesis.116
https://orcid.org/0000-0002-4515-3807

VILNIUS UNIVERSITY
CENTER FOR PHYSICAL SCIENCES AND TECHNOLOGY

Tomas
MURAUSKAS

Transparent and conductive La-doped barium stannate for optoelectronic applications: thin film chemical vapor deposition

DOCTORAL DISSERTATION

Natural Sciences,
Chemistry (N 003)

VILNIUS 2020

This dissertation was written between 2016 and 2020 at Vilnius University.

Academic supervisor:
Assoc. Prof. Dr. Valentina Plaušinaitienė (Vilnius University, Natural Sciences, Chemistry – N 003).

This doctoral dissertation will be defended in a public meeting of the Dissertation Defence Panel:
Chairman – **Prof. Habil. Dr. Rimantas Ramanauskas** (Center for Physical Sciences and Technology, Natural Sciences, Chemistry – N 003).
Members:
Prof. Dr. Ingrida Ancutienė (Kaunas University of Technology, Natural Sciences, Chemistry – N 003);
Assoc. Prof. Dr. Inga Grigoravičiūtė-Puronienė (Vilniaus university, Natural Sciences, Chemistry – N 003);
Dr. Vladimir Sivakov (Leibniz Institute of Photonic Technology, Natural Sciences, Chemistry – N 003);
Dr. Aleksej Žarkov (Vilniaus university, Natural Sciences, Chemistry – N 003).

The dissertation shall be defended at a public meeting of the Dissertation Defense Panel at 2 p.m. on 11 December 2020 at the Inorganic Chemistry auditorium 141 of the Institute of Chemistry, Faculty of Chemistry and Geosciences, Vilnius University.
Address: Naugarduko str. 24, LT-03225, Vilnius, Lithuania
Tel. +370 5 219 3108; e-mail: info@chgf.vu.lt

The text of this dissertation can be accessed at the Libraries of Vilnius University and Center for Physical Sciences and Technology, as well as on the website of Vilnius University: *www.vu.lt/lt/naujienos/ivykiu-kalendorius*

https://doi.org/10.15388/vu.thesis.116
https://orcid.org/0000-0002-4515-3807

VILNIAUS UNIVERSITETAS
FIZINIŲ IR TECHNOLOGIJOS MOKSLŲ CENTRAS

Tomas
MURAUSKAS

Šviesai skaidrus ir elektrai laidus lantanu legiruotas bario stanatas optoelektriniams taikymams: plonų sluoksnių nusodinimas iš cheminės garų fazės

DAKTARO DISERTACIJA

Gamtos mokslai,
Chemija (N 003)

VILNIUS 2020

Disertacija rengta 2016– 2020 metais Vilniaus universitete.

Mokslinis vadovas:
doc. dr. Valentina Plaušinaitienė (Vilniaus universitetas, gamtos mokslai, chemija – N 003).

Gynimo taryba:
Pirmininkas – **prof**. **habil. dr. Rimantas Ramanauskas** (Fizinių ir technologijos mokslų centras, gamtos mokslai, chemija – N 003).
Nariai:
prof. dr. Ingrida Ancutienė (Kauno technologijos universitetas, gamtos mokslai, chemija – N 003);
doc. dr. Inga Grigoravičiūtė-Puronienė (Vilniaus universitetas, gamtos mokslai, chemija – N 003);
dr. Vladimir Sivakov (Leibnico fotoninių technologijų institutas, Vokietija, gamtos mokslai, chemija – N 003);
dr. Aleksej Žarkov (Vilniaus universitetas, gamtos mokslai, chemija – N 003).

Disertacija bus ginama viešame Chemijos mokslų krypties gynimo tarybos posėdyje 2020 m. gruodžio mėn. 11 d. 14 val. Vilniaus universiteto Chemijos ir geomokslų fakulteto Chemijos instituto Neorganinės chemijos auditorijoje 141. Adresas: Naugarduko g. 24, LT-03225, Vilnius, Lietuva, tel. +370 5 219 3108; el. paštas info@chgf.vu.lt.

Disertaciją galima peržiūrėti Vilniaus universiteto, Fizinių ir technologijos mokslų centro bibliotekose ir VU interneto svetainėje adresu: *https://www.vu.lt/naujienos/ivykiu-kalendorius*

ABSTRACT

Transparent conductive oxides (TCO) with high mobility are being investigated for their application in transparent electronics. $BaSnO_3$, in earlier years investigated for its photocatalytic properties and gas-sensing, has recently emerged as a material of great interest. La-doped barium stannate (LBSO) single crystals were reported to achieve electron mobilities as high as 320 $cm^2V^{-1}s^{-1}$ at room temperature. Also, barium stannate demonstrated high-temperature oxygen stability, which gives it an advantage over other TCO materials such as Al-doped ZnO and ITO. Its high optical transmission (>80%) and intermediate conductivity (10^{-8} – 10^3 S cm^{-1}) are essential factors for modern electronic and optoelectronic device components. TCO *pn* junctions, transparent electric channels, field-effect transistors are integrated into solar cells, light-emitting diodes, and gas-sensors. Another advantage of LBSO lies in its perovskite structure. It is structurally similar to a vast number of functional oxide materials such as ferroelectrics, multiferroics, and photovoltaics. This potentially enables a possibility to develop all-perovskite heterostructures with ample physical properties.

Applications of LBSO require viable synthesis methods, which would produce materials with excellent electrical and optical properties. Epitaxial thin films were deposited using laser ablation (PLD), magnetron sputtering, and molecular beam epitaxy (MBE). However, the highest electron mobilities in thin-films of 150 $cm^2V^{-1}s^{-1}$ on $PrScO_3$ and 183 $cm^2V^{-1}s^{-1}$ on $DyScO_3$ are almost two times lower than mobilities in single-crystals. Thin-film carrier mobility decrease was largely attributed to a significant density of defects. Substrate lattice mismatch and the resulting high density of misfit and threading dislocations are discussed as limiting factors of carrier mobilities. To overcome such issues, the use of various buffer layers was proposed. However, mobility was not significantly increased even in homoepitaxial films grown on BSO substrates. This suggests that the origin of reduced mobility is not attributed mainly to threading and misfit dislocations.

Much of the studies to-date focused on dislocations as defects, nearly avoiding the possibly crucial role of point defects and nonstoichiometry. Evidence that these factors are crucial in the LBSO system is the observation of different mobility values for films grown via different synthesis routes despite having similar substrates and doping concentrations. The data on nonstoichiometry and its effects is quite scarce or partially incomplete. Therefore in this work, a major role of nonstoichiometry was investigated.

Thin-film PI-MOCVD method was systematically developed and optimized for the deposition of thin LBSO films allowing easy control of film

composition. The work was started by selecting metalorganic Sn, Ba, and La precursors and investigating their deposition kinetics. SnO_2, undoped, and La-doped single-phase BSO thin-films were successfully deposited on $SrTiO_3$, $LaAlO_3$, and Al_2O_3 substrated with varying Sn/Ba ratios. It was demonstrated that the deviation from near-stoichiometric composition led to significant changes in morphology, microstructure, optical and electrical properties. LBSO films demonstrated only low values of mobility (20 $cm^2V^{-1}s^{-1}$). Therefore, the PI-MOCVD process was optimized further. In the final experiments, high mobility epitaxial thin films of 380 nm were deposited on MgO and $SrTiO_3$ substrates. A shift of the RP-phase formation composition was discovered. At the composition, smoothest and high mobility (120 $cm^2V^{-1}s^{-1}$) films were achieved on $SrTiO_3$ substrates. Even at a high growth rate, the deposited films' electrical properties were comparable to those obtained by MBE and PLD methods. It was demonstrated that sufficient electrical properties on epitaxial substrates could be achieved without buffer layers or highly lattice-matched substrates. Understanding charge compensation mechanisms and control of thin-film composition was the key factor in achieving great electrical properties.

Keywords: transparent conductive oxide, perovskite, barium stannate, stannate, BSO, LBSO, MOCVD, electron mobility, charge compensation mechanism, XRD, SEM, spectroscopy, optical properties, electrical properties.

LIST OF PUBLICATIONS

This thesis is based on the articles included in the Web of Science database:

I. J. Podhorsky, T. Murauskas, C. Hegemann, D. Graf, T. Fischer, M. Babiak, J. Pinkas, V. Plausinaitiene, S. Mathur, A. Abrutis, Z. Moravec, Preparation of Heteroleptic Tin(IV) N,O-β-heteroarylalkenolate Complexes and Their Properties as PI-MOCVD Precursors for SnO_2 Deposition, *European Journal of Inorganic Chemistry*, 10.1002/ejic.201800913 (2018).

II. T. Murauskas, V. Kubilius, Z. Saltyte, V. Plausinaitiene, Metalorganic chemical vapor deposition and investigation of nonstoichiometry of undoped $BaSnO_3$ and La-doped $BaSnO_3$ thin films, *Thin Solid Films*, 692 (2019) 137575.

AUTHOR'S CONTRIBUTION TO THE ARTICLES

I. The author carried out thermogravimetric testing of the commercial and co-authors' synthesized precursors and developed synthesis conditions for SnO_2 thin film deposition using the MOCVD method. Investigated the possibilities of incorporating synthesized novel metalorganic compounds in the synthesis of stannate thin films. The author also carried out structural, optical, and morphology investigation of thin SnO_2 films synthesized at different deposition temperatures. The analysis results were analyzed with the co-authors and published in an article.

II. The author developed optimal conditions and carried out MOCVD synthesis of thin undoped and La-doped barium stannate thin films. The author is responsible for thin-film characterization using multiple analysis methods: X-ray diffraction, elemental analysis, scanning electron microscopy, atomic force microscopy. The results were analyzed with the co-authors and published in an article.

TABLE OF CONTENTS

LIST OF ABBREVIATIONS

acac	-Acetylacetonate group
AcO	-Acetoxy group
AFM	Atomic force microscopy
BSO	Barium stannate ($BaSnO_3$)
BSSO	Antimony-doped barium stannate ($Sb:BaSnO_3$)
Bu	-Butyl group
CVD	Chemical vapor deposition
DMOTFP	-3,3,3-trifluoro(dimethyl-1,3-oxazol-2-yl)propen-2-ol group
HAADF-STEM	High-angle annular dark-field scanning transmission electron spectroscopy
LAO	Lanthanum aluminate ($LaAlO_3$)
LIO	Lanthanum indate ($LaInO_3$)
LAADF-STEM	Low-angle annular dark-field scanning transmission electron spectroscopy
LBSO	Lanthanum-doped barium stannate
DME	2,2-dimethoxyethane (monoglyme) or dimethoxyethane
O_tBu	Tert-butyl alcohol group
EDX	Energy-dispersive X-ray spectroscopy
ICP-MS	Inductively induced plasma mass spectrometry
PI-MOCVD	Pulsed-injection metalorganic chemical vapor deposition
PyTFP	-3,3,3-trifluoro(pyridin-2-yl)propen-2-ol group
SEM	Scanning electron microscopy
STO	Strontium titanate ($SrTiO_3$)
TEM	Transmission electron microscopy
TGA	Thermogravimetric analysis
thd	-2,2,6,6-tetramethyl-2,5-heptanedionate group
Triglyme	Triethylene glycol dimethyl ether
Tetraglyme	Tetraethylene glycol dimethyl ether
XRD	X-ray diffraction
XPS	X-ray photoelectron spectroscopy

INTRODUCTION

This Ph.D. dissertation is devoted to the PI-MOCVD synthesis development of single material: La-doped $BaSnO_3$ (LBSO). Barium stannate has drawn great attention in the field of oxide electronics after reported high electron mobility of 320 $cm^2V^{-1}s^{-1}$ in bulk La-doped $BaSnO_3$ single crystal [1]. Superior oxygen stability and unparalleled charge carrier mobility has never been reported in any other perovskite oxide materials and surpassed a long-standing limit of mobility at room temperature. Materials with perovskite structure have exhibited a wide range of physical properties such as large photovoltaic effects [2, 3], superconductivity [4-7], colossal magnetoresistance [8, 9], ferroelectricity [10, 11], and multiferroicity [12, 13]. Wide-scale research has been performed to utilize such versatile physical properties in the form of single-layered thin films and their heterostructures [14, 15]. There is also growing interest in new perovskite-type transparent conductive oxides in which carrier doping and structural modification can be more flexible than in conventional binary oxides such as indium doped tin oxide. The most studied perovskite oxides in this context are doped $SrTiO_3$ and $KTaO_3$, in which electron mobility μ values at ∼2 K are as high as 32667 and 23000 $cm^2V^{-1}s^{-1}$, respectively [16-20]. Such high mobilities are partly due to high dielectric constants $\varepsilon(SrTiO_3) \approx 20\ 000$ and $\varepsilon(KtaO_3) \approx 4500$ at cryogenic temperatures, which help reduce the ionic dopant scattering due to dielectric screening. However, at room temperature, perovskites show much lower mobility (∼1 – 30 $cm^2\ V^{-1}\ s^{-1}$) even in compared to binary oxides, hindering their practical device applications.

Bulk barium stannate materials have shown very promising electrical properties. However, obtaining high mobility in thin films at room temperature remains a challenge. So far, obtained films have demonstrated significantly lower mobilities compared to bulk LBSO. Undoped (BSO) and doped BSO films have been deposited using magnetron sputtering [21, 22], pulsed laser deposition (PLD) [23], and molecular beam epitaxy (MBE) [24, 25] methods. The best results in terms of mobility were obtained by MBE. The highest mobility values were demonstrated by Paik et al., achieving the highest mobility of 183 $cm^2\ V^{-1}\ s^{-1}$ in MBE grown LBSO films on $DySnO_3$ [26]. High mobilities of 150 $cm^2\ V^{-1}\ s^{-1}$ and 100 $cm^2\ V^{-1}\ s^{-1}$ were also achieved by Raghavan et al. on $PrScO_3$ and $SrTiO_3$, respectively. The reduced mobilities in LBSO films have been primarily attributed to the substrate-induced misfit/threading dislocations in films [27] acting as charge carrier scattering centers at the grain boundaries. Also, worse electrical properties in

LBSO films resulted from point defects formed by the deviation from stoichiometry (Sn/(Ba + La)=1).

Nonstoichiometry resulted in a significant reduction in the concentration and mobility of n-type carriers due to formed compensating point defects in this material [28]. La_{Ba} donors can be compensated by acceptor-type native point defects, such as Ba or Sn vacancies, or by anti-site defects La_{Sn} as self-compensation acceptors. Thus, the possibility to control composition, the concentration of nonstoichiometric compensating acceptor-type point defects, and the density of threading dislocations would possibly contribute to producing high mobility and conductivity LBSO films. La_{Sn} anti-site defect negative contribution, on the other hand, could theoretically be suppressed in cation-rich and oxygen-poor conditions in La–Ba–Sn–O system, as shown in theoretical calculations by Weston et al. [28]. Also, control of factors, such as substrate structure, deposition conditions contributing to film microstructure, and stoichiometry, would result in better electrical properties as well. Using an optimized deposition process, LBSO films with excellent electrical properties were obtained by MBE and PLD methods. However, the results' reproducibility was not high, as films grown by the same technique showed large variation in electrical properties, especially in mobility. This might be related to difficulties in controlling the precise stoichiometry of LBSO films in these techniques. In addition, little to no results are reported regarding a wide range of stoichiometry in BSO or LBSO films.

In this dissertation, the main attention is given to the detailed development of PI-MOCVD synthesis and stoichiometry-related properties. The work is started by selecting tin, barium, and lanthanum precursors and their thermogravimetric analysis. Tin precursors are tested by varying deposition conditions. Surface morphology and deposition kinetics are determined at different deposition temperatures ranging from 400 °C to 900°C. Films are characterized using X-ray diffraction analysis, atomic force microscopy, and scanning electron microscopy.

After the selection of suitable precursors ($Sn(thd)_2$, $Ba(thd)_2$*triglyme, $La(thd)_3$), thin barium stannate film deposition is carried out. The optimal BSO formation temperature of 850°C is determined. Main deposition conditions affecting structural, optical, and electrical properties of BSO and LBSO are discussed in later sections. The influence of the increasing lattice mismatch of $LaAlO_3$ (100), $SrTiO_3$ (100), and Al_2O_3 (0006) substrates on the film's structural properties is investigated. In the last chapters, the structural, electrical properties of „thick" (380 nm) La-doped films deposited on $SrTiO_3$ (100) and MgO(100) are investigated in the narrowed stoichiometric region,

showing a very strong influence of slight deviation from stoichiometric composition.

The aim of this Ph.D. thesis was to apply the PI-MOCVD method for the deposition of thin barium stannate films and investigate thin film properties and the influence of deposition conditions on structural and electrical properties. In order to achieve this aim, the following tasks were formulated:

1. To select and compare suitable metalorganic precursors for pulsed-injection metalorganic chemical vapor deposition (MOCVD) for the deposition of La-doped barium stannate thin films.
2. To characterize and compare thin tin oxide film properties and growth kinetics using commercially available, synthesized, and novel metalorganic precursors for the synthesis.
3. Develop and optimize the deposition conditions for thin $BaSnO_3$ thin film deposition in terms of deposition temperature, substrate lattice mismatch, and Sn/Ba non-stoichiometry.
4. To achieve n-type electrical conductivity in thin La-doped barium stannate films and characterize the electrical properties using Van der Pauw four-point probe method and Hall measurements.
5. To investigate the influence of Sn/Ba nonstoichiometry influence on microstructure, morphology, and electrical properties of thin $BaSnO_3$ thin films.
6. To achieve carrier mobility values comparable to values achieved in films deposited by physical deposition methods.

Statements to be defended:

1. Volatile and thermally stable metalorganic precursors $Ba(thd)_2$*triglyme, $La(thd)_3$*monoglyme and $Sn(thd)_2$ are suitable for the PI-MOCVD synthesis of La-doped and undoped $BaSnO_3$ deposition.
2. The PI-MOCVD method is suitable to grow thin undoped and La-doped epitaxial and polycrystalline films.
3. Undoped and La-doped thin film properties (morphology, phase composition, optical, electrical) are greatly dependent on the Sn/Ba ratio in the film.
4. Thin-film (Sn/Ba) composition control is a crucial factor in achieving high carrier concentration and carrier mobility.

1. LITERATURE REVIEW

1.1. The brief history of barium stannate research

Before BSO's breakthrough as a wide bandgap semiconductor, BSO has been reported in various papers for its technical applications. The first record of barium stannate is mentioned in the U.S. patent of 1944 regarding BSO use in glass enamels to increase alkali resistance [29]. In a few years, more patents written by Weiner followed. In order to increase the dielectric constants and thermal stability, the use of barium stannate in $BaTiO_3$ ceramics was reported [30-32].

In 1952 barium stannate has been used in fundamental studies of tetragonal-cubic $BaTiO_3$ (BTO) systems [33]. $BaTiO_3$ showed a temperature-dependent variation of dielectric permittivity and the existence of a ferroelectric state in which the material is also piezoelectric. The ferroelectric state persisted from absolute zero to a definite phase transition temperature at which thermal agitation destroyed spontaneous polarization [34]. In the vicinity of this temperature, a sharp increase in permittivity was observed. This temperature, called Curie temperature, dielectric permittivity, and capacitance coefficients, were highly affected by the concentration of introduced $BaSnO_3$ (BSO) and $SrTiO_3$ (STO) in BTO-BSO-STO ceramic systems. The increase of BSO in BTO ceramics lowered the Curie temperature significantly compared to STO. This was explained by the substitution of Ti by Sn ions in the BTO lattice, changing the volume and the BTO lattice's polarizability. Sn ions' introduction created local structure disorder, diffused the transition temperature, and broadened temperature-dependent dielectric functions. In 1954 Smolensky and Isupov investigated temperature-dependent properties of $BaTi_{1-x}Sn_xO_3$ (BTSO) ceramics. They also investigated the stability of dielectric constant and Sn incorporation into the BTSO structure [35]. After BTSO was recognized as a functional material for various applications, decades of its research followed [36-40]. BTSO ceramics had also been studied for practical applications such as grain boundary layer capacitors [41], piezoelectric bending actuators [42], and gas sensors [43]. Recently, the BSO's dielectric constant was reported to be stable up to 450 K, showing oxygen stability in the BSO system itself [44].

BSO research related to its semiconductor properties was arguably the most critical study that followed its early research. In 1976 Prokopalo paper evaluating various perovskites' electrical properties reported n-type conductivity in BSO ceramics [45]. A year later, B. Ostick reported another essential study. Hall mobility measurements at elevated temperatures of

1000°C were carried out on BSO ceramic samples. Carrier density was measured by changing the partial pressure of oxygen. Their research showed that carrier density decreased from 10^{23} cm^{-3} to 10^{19} cm^{-3} when oxygen partial pressure was reduced from 10^4 to 10^2 Pa [46]. In the following paper, thin BSO films deposited on Al_2O_3 substrates were reported. The same measurements at lower temperatures of 700 °C were carried out. No significant difference in electrical properties from ceramics was reported [47]. Oxygen stability in high temperatures of both ceramics and thin films led to research related to gas-sensing applications. BSO was discussed in various papers as possible sensitive material for O_2, NO, NO_2 [48], CO [49, 50], CO_2 [51], CH_4 [52], H_2S [53], and other gases [54, 55].

Doping of barium stannate with metal impurities was arguably first reported by J.M. Hermann in 1982. Sb was selected as a dopant, which replaced Sn^{4+} ions in the stannic position [56]. It was argued that the Sb dopant acts as an electron donor in the Sb^{5+} state. The maximum solubility of the dopant in the BSO was determined at 17 %. In 1989 a paper on antimony-doped barium stannate (BSSO) was published confirming the Sb^{5+} ionic state using XPS spectroscopy. A favorable bandgap of E_g = 3.4 eV was reported, signifying doped BSO possible use in photovoltaic applications. However, Sb doping reduced the visible range's optical transparency, greatly hindering its use as TCO [57]. In 1991 Cava et al. published a comparative study regarding $BaSn_{1-x}Sb_xO_3$ and $La_{1-x}Sr_xNiO_4$. The absence of superconductivity was discovered in BSSO up to 0.05 K. This was explained by mixed Sb^{3+}/Sb^{5+} states acting as deep donors and impurities, which also trapping charge carriers [58]. Following Cava's work, based on local density approximation Singh published the first calculated electronic band structure, which supported the existence of mixed Sb states [59]. In 1993, the mixed Sb state explanation was argued by R. Claessen when core-level XPS spectra of Sb $3d_{3/2}$ demonstrated no chemical shift related to Sb^{3+} species [60]. A new doping mechanism has been proposed in BSSO that Sb-5s electrons actually could get into the conduction band as a displacement of O^{2-} ions towards Sb^{5+} ions raised the energy of Sb-5s states and lowered that of Sn-5s states. The existence of Sb^{3+} states was eventually demonstrated using the recent results of Mössbauer spectroscopy of BSSO measured at 4.2 K [61].

After the use of antimony in BSO, an array of dopants were introduced. BSO systems such as $Ba_{1-x}Sr_xSnO_3$ were investigated but showed no promising results regarding electron mobility or electrical conductivity [62, 63]. Other elements were used as dopants occupying either A-site or B-site position in perovskite ABO_3 structure of BSO: Co (B) [64, 65], Cr (B) [66], Fe (B) [67, 68], Ge (B) [69], Mn (B) [70, 71], Ni (B) [66], Nb (B) [72], Pb (A)

[73], Pr (B) [74], Si (B) [75], Te (B) [76]. Mainly B-site dopants were considered. In 2009 an atomistic simulation by Wang was published, again demonstrating the low energies needed for B-site doping for many elements (Fe, Sc, Y, Gd). The lowest energies for the A-site doping were considered for Nd, Sm, and La [77]. While only in 2008, a first-principle theoretical study was published on hydration and incorporation of Sm, In, Y, Gd into the BSO system [78], La was already experimentally investigated in 1994. Trari et al. doped polycrystalline samples of BSO with La. In their report, La solubility was only less than 2 % in $Ba_{1-x}La_xSnO_3$ [79]. LBSO showed no improvement in the electrical properties compared to BSSO. A midgap band and Anderson type localization were proposed to explain the absence of superconductivity and lack in conductivity at r.t. LBSO system has been disregarded for more than a decade. Even in 2007 a comparative study on Sb and La doped BSO was published demonstrating carrier mobility of $\mu = 0.69$ $cm^2V^{-1}s^{-2}$ at carrier concentration of $n = 10^{21}$ cm^{-3} in LBSO system (lower than BSSO).

In 2012 a breakthrough in the LBSO system was reported. In a paper published in Applied Physics Express, H. J. Kim et al. reported 320 cm^2V^{-1} s^{-1} and 70 $cm^2V^{-1}s^{-1}$ as the electron mobility of BLSO single crystals and epitaxial films, respectively [80]. The recorded mobility was higher than the mobility of any wide-bandgap semiconductor at r.t., even GaN. After this report, LBSO regained the interest of scientific society. In a few years, many papers on thin-film fabrication and detailed theoretical and experimental studies of various properties were published. In the topic of thin-film synthesis, the best mobility results were obtained by MBE. The highest mobility values were demonstrated by Paik et al., achieving the highest values of 183 cm^2 V^{-1} s^{-1} in MBE grown LBSO films on $DySnO_3$ [26]. High mobilities of 150 cm^2 V^{-1} s^{-1} and 100 cm^2 V^{-1} s^{-1} were also achieved by Raghavan et al. on $PrScO_3$ and $SrTiO_3$, respectively. The rapid progress of BLSO research led it ultimately to becoming one of the "post-silicon" candidates [81].

1.2. Crystal structure of $BaSnO_3$ and common defects

Barium stannate is one of the alkaline earth perovskite stannates having $ASnO_3$ (A = Ca, Sr, Ba) structure. While other alkaline earth stannates such as $CaSnO_3$ [82] and $SrSnO_3$ [83] have an orthorhombic structure, $BaSnO_3$ (as well as La-$BaSnO_3$) is known to be cubic at room temperature and ambient pressure [84]. In the BSO structure, Sn ions form an octahedron with oxygen. SnO_6 octahedra are linked in three-dimensional networks with corner-sharing oxygen. Ba atoms occupy the space in the planes of shared oxygen atoms. The

electronic valence configuration for each atomic species corresponds to Ba-$5s^2 5p^6 6s^2$, Sn-$4d^{10} 5s^2 5p^2$, and O-$2s^2 2p^4$ [85]. Goldschmidt tolerance factor, according to Shannon's ionic radii, equals to t=1.02 [86]. Its value shows that the structure theoretically has no polar distortions and is probably too high to have SnO_6 octahedral tilts in the lattice. BSO space group in Hermann Maugain system is $Pm\bar{3}m$ (221). Its lattice parameter a of 4.117 Å [23, 87, 88] was determined experimentally and theoretically [89, 90] and reported in various papers. BSO has a lattice volume of 73.5 $Å^3$. The average linear thermal expansion coefficient of BSO is 9.3×10^{-6} K^{-1} from 300 K to 1773 K [84]. With the increasing temperature cubic symetry is maintained. Simple depiction of BSO lattice and oxygen octahedra is given in Fig. 1.

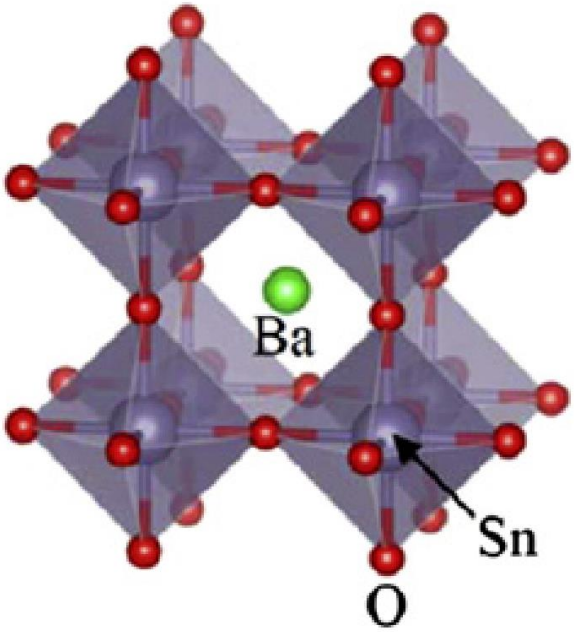

Fig. 1. $BaSnO_3$ lattice with highlighted SnO_6 octahedra and barium atoms in between the octahedra [85].

$BaSnO_3$ is of high symmetry cubic lattice. The symmetry is maintained when the structure is doped with lanthanum [79]. However, various defects are relevant to this material. The native point defects in consideration for undoped n-type BSO include oxygen vacancies (V_O), Sn on Ba antisite (Sn_{Ba}), tin interstitial (Sn_i), and barium interstitial (Ba_i). In contrast, the p-type BSO defects include barium vacancy (V_{Ba}), tin vacancy (V_{Sn}), Ba on Sn antisite (Ba_{Sn}), and oxygen interstitial (O_i). Native defect formation has been studied using computational analysis methods such as DFT [91]. In the highly

comprehensive study of Scanlon, two types of conditions are set: A, which corresponds to Sn-rich, Ba-rich, and O-poor conditions, and is expected to be optimum for n-type defect formation, whereas B represents the Sn-poor/O-rich limit with Ba also poor, and is expected to favor the formation of p-type defects. Figure 2 (a) and (b) show a plot of formation energy as a function of the Fermi level for all intrinsic defects under two chosen chemical potential environments.

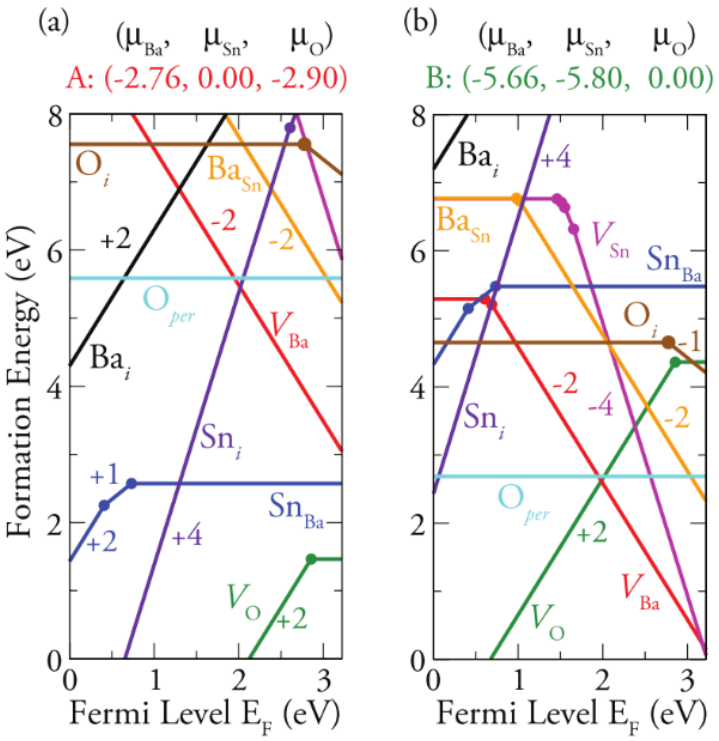

Fig. 2. Formation energies for intrinsic defects under condition A(Sn-rich, Ba-rich, O-poor) (a), and B(Sn-poor/O-rich limit, Ba-poor) (b). The slope lines denote the charge site; the larger the slope, the bigger the charge site. The solid dots represent transition levels [91].

Under condition A(Sn-rich, Ba-rich, O-poor), V_O is the lowest energy intrinsic donor. This behavior is consistent with that of V_O in other wide-bandgap n-type transparent conductive oxides (TCOs), i.e., ZnO [92-95], SnO_2 [96], Ga_2O_3 [97], and In_2O_3 [98, 99]. In this case, however, the 2+/0 transition level for the V_O is farther from the conduction band minimum (CBM) (~3.6 eV); below the CBM V_O is unlikely to provide high levels of conductivity in this system. Sn_{Ba} is the next most stable defect and acts as an

ultradeep donor with +1/0 and +2/+1 transitions levels 0.73 eV and 0.41 eV above the VBM, respectively. It should be noted that although "self-doping" by cation-on-cation antisites can dominate conductivity in other ternary TCOs [100], this is not the case for $BaSnO_3$. The Ba site is $BaSnO_3$ is so large that it can stabilize Sn in the 2+ charge state, and this is the origin of its deep donor nature. Sn_i and Ba_i both act as shallow donors but are considerably higher in energy and are unlikely to play a large role in conductivity in $BaSnO_3$. The lowest energy native acceptor defect is the V_{Ba}, but it is too high in energy to compensate the V_O and the Sn_{Ba}. Under oxygen-rich conditions (condition B), the native acceptor defects are much lower in energy and can compensate the native donors. The lowest energy acceptor defect is oxygen interstitial (O_i). However, it relaxes from the ideal interstitial site towards lattice oxygen, displacing it to form a peroxide (O-O dumbell-like) species, which is denoted as O_{per}. An O_i on the perfect interstitial site is quite unstable relative to the O_{per}. This type of behavior has also been noted previously for other wide-bandgap oxides [101]. Although the formation energy of $O_{per} \sim 2{,}40$ eV under typical p-type conditions is much lower than that of the neutral formation energies of V_{Ba}, V_{Sn}, and Ba_{Sn}, its ionization levels are deep in this conduction band. This indicates that it will not act as an effective charge compensating defect in $BaSnO_3$. V_{Ba} is clearly a dominant acceptor defect for all growth conditions. Under metal-poor and oxygen-rich conditions, the Fermi level will be fixed in the bandgap with two primary defects V_O^{2+} and V_{Ba}^{2-}. Under typical p-type conditions, $BaSnO_3$ will be an insulator, with n-type conductivity fully compensated. None of the native defects in $BaSnO_3$ can act as shallow defects, and under O-rich conditions, native n-type defects will be compensated. The only introduction of an extrinsic dopant such as lanthanum can make BSO into a degenerate semiconductor.

$BaSnO_3$, as well as other perovskite materials, were shown to form a two-dimensional defect called Ruddlesden-Popper stacking faults or RP phase. The idea behind the RP phase is the existence of additional layers inserted in the long-range periodic BaO-SnO_2 layered structure along the <100> direction or parallel to (l00) planes of BSO lattice. The empirical representation of RP phase correspond to $Ba_{n+1}Sn_nO_{3n+1}$, where n=0,1,2,3… The experimental parameters and spacegroups are cubic $BaSnO_3$ ($Pm\bar{3}m$, a = 4.116 Å), body-centered tetragonal Ba_2SnO_4 (I4/mmm, a = 4.141 Å, c = 13.2834 Å) [102] and body-centered tetragonal $Ba_3Sn_2O_7$ (I4/mmm, a = 4.129 Å, c = 21.460 Å) [74]. RP phase depiction is given in Figure 3, showing BSO and the first two series members. RP phase is primarily formed during nonhomogenous and nonstoichiometric growth of thin films. It is shown to

worsen thin films' electric properties as additional BaO layers act as an insulator. A fourth member of the series $Ba_4Sn_3O_{10}$ is also hypothetically possible but has not been demonstrated experimentally. First principle calculations have been employed to investigate in-plane plasma frequency (Ω_p) dependence of RP series members. The conductivity (σ) of degenerately doped semiconductors depends on the plasma frequency, $\sigma \propto \Omega^2\tau$ where τ is an inverse effective scattering rate. It has been demonstrated that in terms of similar scattering rates, the conductivity follows a perhaps expected trend relevant to the density of Sn ions (i.e., falling as the concentration of insulating BaO increases). Specifically, for in-plane conduction, $\sigma(BaSnO_3) > \sigma(Ba_3Sn_2O_7) > \sigma(Ba_2SnO_4)$. The volumes per Sn ions in the lattice are 69.73 $Å^3$, 91.47 $Å^3$, and 113.90 $Å^3$, for $BaSnO_3$, $Ba_3Sn_2O_7$, and Ba_2SnO_4, respectively. The barium oxide (BaO) layers, while not contributing to conduction, also would not be expected to contribute to optical absorption. Therefore, this suggests that the layered compounds could theoretically be good TCO as well. Optical phonon calculations apply to higher members of the RP series, but this is not the case for Ba_2SnO_4. This implies a problematic trend experimentally – small deviation from stoichiometry, which would result in the formation of the first member of the RP series (Ba_2SnO_4), would quite largely contribute to decreased conductivity in the films.

Besides the RP phase formation, dislocations and stacking faults (SFs) are persistent in thin BSO/LBSO films. Generally, the lattice mismatch between the substrate and the film is released by generating misfit dislocations (MD) at or near the interface [19-22]. The formation of the MD's is often related to the evolution of threading dislocations (TDs) [23]. Due to a large mismatch of LBSO/BSO and, e.g., $SrTiO_3$ (~5 %), a large number of MDs and TDs are expected. This is mainly caused by strain relaxation. As an example, a cross-sectional LAADF-STEM image of the entire LBSO film thickness is shown in Fig. 4 (a). The high sensitivity of LAADF to strain and dislocations makes it easy to see the threading dislocations [103]. They are the vertically running defects with dark contrast in the $BaSnO_3$ film; one is indicated by a yellow arrow in Fig. 4 (a). The HAADF-STEM images in Fig. 4 (b) and 4 (c) show the fully relaxed interface between the $DyScO_3$ substrate and the $BaSnO_3$ film. In this case, the spacing between the edge dislocations is, on average, 23 unit cells of $DyScO_3$ vs. 22 unit cells of $BaSnO_3$, which is consistent with that calculated from the ratio of the relaxed lattice parameters.

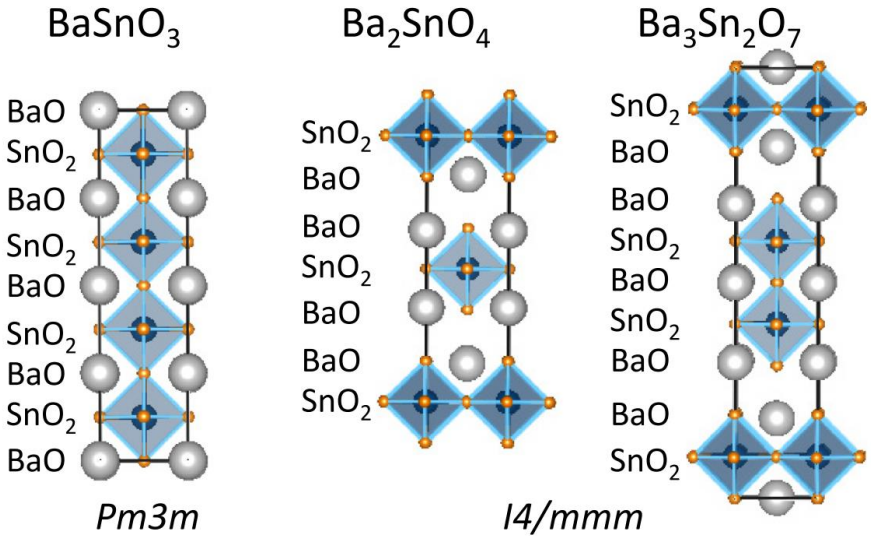

Fig. 3. Cubic perovskite structure and the first to members of the Ruddlesden-Popper series, showing she stacking of BaO and SnO_2 layers [104].

Extended dislocations can also be seen, as indicated by the yellow arrow in Fig. 4 (b). Figure 4 e) is a low magnification HAADF-STEM image of a plan-view sample only containing the BSO film in [001] direction. The SFs labeled by A indeed lie precisely on (100) planes, and they appear in regular shapes. One of the SF is marked in yellow contour. The translational displacement projection along (100) plane can be deduced to be ½ a <110>. In perovskite materials, there are normally two kinds of translational displacements involved with the stacking faults: ½ a < 111 > [105, 106] and ½ a < 110 > [107]. In the former case, the projected translational displacements along < 100 > direction are always ½ a < 110 > , while in the latter case it should contain projected translational displacements of ½ a <100> along one of the < 100 > directions. Since all the SFs that both plan-view and cross-sections are with projected translational displacements of ½ a < 110 >, the translational displacements of the SFs here in the film should be ½ a < 111 >. And such kind of SFs is all on (*l*00) planes they are normally named in terms of Ruddlesden-Popper faults [26,28].

For the TDs in Fig. 4 (e), extended dislocation of a < 110 > (B_2) is identified. The extended dislocation includes two ½ a <110> type partial dislocations (marked in Fig. 4 (e) by the white arrow on the right) connected with a short SF. The short SF lies on (110) planes and has a translational displacement of ½ a <110>, which is the same as the partial dislocation. The formation of such SFs is proposed to be associated with the climbing of a ½ a < 110 > partial TD.

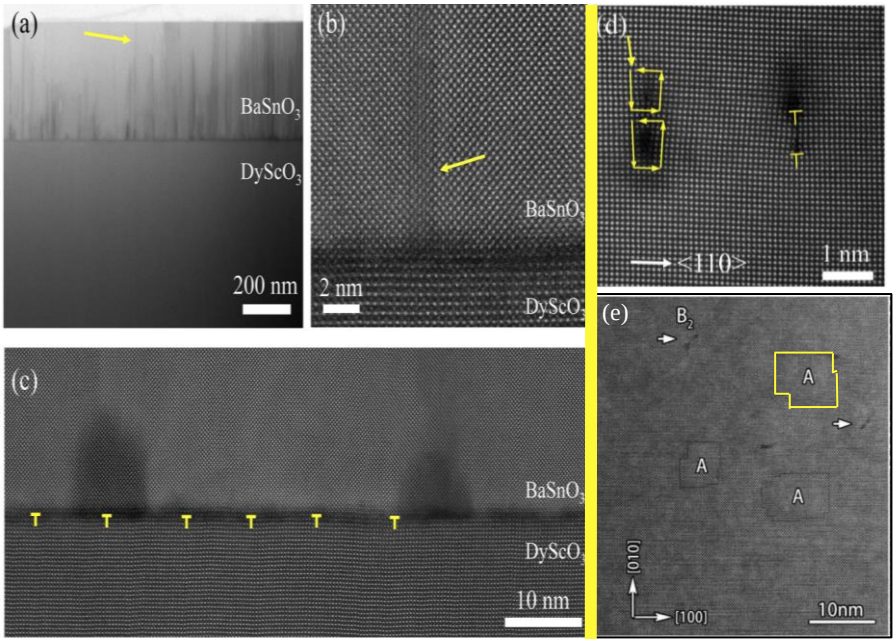

Fig. 4. Cross-sectional STEM images of La-doped $BaSnO_3$ film characterized in (a) LAADF-STEM image showing the entire film thickness. The yellow arrow indicates a threading dislocation; (b) edge dislocations; (c) HAADF-STEM images of the $BaSnO_3/DyScO_3$ interface are shown; d) The Burgers circuits drawn on the left, revealing two partial edge dislocations, each with a Burgers vector with an in-plane projection of ½ a <110>. The arrowed dislocation is not hollow, whereas the dislocation below it is hollow; e) low magnification of HAADF-STEM image of plan-view sample only contains [001] direction. Polygon shapes comprised of SFs are labeled A, B denotes a <100> type threading dislocations. B_2 denotes partially terminated extended threading dislocation [26, 108].

The dislocation density of MDs, TDs, and SFs, associated with decreased conductivity, is dependent on the substrate lattice parameter and has been calculated for some substrates, e.g., 4.9×10^{10} cm^{-2} LBSL||STO [109], 2.1×10^{10} cm^{-2} LBSO||(Ba,Sr)SnO_3||STO [23]. In order to decrease dislocation density, the substrate of a very similar lattice parameter should be selected. However, there are no commercial substrates whose parameter is close to ~ 4.116 Å. Moreover, due to the highly evaporating and decomposing nature of constituent elements, the growth of large $BaSnO_3$ single crystals (as a substrate) has been somewhat challenging. Another way to improve thin film electrical properties is the addition of buffer layer. $BaSnO_3$, (Ba,Sr)SnO_3

buffers have been succesfully employed in improving electric properties and remains the main tool to enhance the electrical properties [110-112].

1.3. LBSO thin film synthesis methods

Extensive efforts have been put into the synthesis methods of La-doped barium stannate. In this chapter, a short review of this topic is given. A vast number of publications of its synthesis methods have been published of BSO and LBSO. However, only the most comprehensive research of doped LBSO will be discussed further, starting from bulk crystals and thin films.

Powders, ceramics, and other powder-like materials have also been synthesized and reported in many publications but will not be discussed here [87, 113-118]. Thin-film synthesis is aimed to produce films of similar quality to the monocrystal. Furthermore, in this work, two classes and their properties are mostly relevant – crystals and thin films. Therefore, in this dissertation, powder topics will be omitted.

Bulk single crystals of LBSO with superior electrical properties were discovered in 2012 by Kim et al. Small crystals of $Ba_{1-x}La_xSnO_3$ (x = 0.037) were synthesized using the flux method. High-purity $BaCO_3$, SnO_2, and La_2O_3 powders were weighed in stoichiometric ratio, thoroughly mixed, and sintered at 1250 °C for 6 hours. Ground powders were pressed into a pellet and were again sintered at 1400-1450 °C for 24-28 hours. For LBSO single crystal growth, sintered powders and Cu_2O flux were placed in a Pt crucible with a molar ratio of 15:1 and fired at 1250 °C. Cube-shaped crystals were produced, showing excellent n-type carrier mobility of 320 $cm^2V^{-1}s^{-1}$ at a doping concentration of $n = 8.0 \times 10^{19}$ cm^{-3}. [119]. XRD analysis confirmed a single-phase LBSO single-crystal structure with ω-scan FWHM values of 0.09°. Later in 2012, a similar study was conducted by Luo et al. The flux method was used as well, but PbO-based flux was used. Samples were prepared by mixing stoichiometric amounts of Ba, Sn, and La oxides. Sintering conditions of 1500 °C for 20 h were selected. Small (6 mm^3) LBSO crystals were successfully grown using the PbO flux. Although, their color varied from light reddish to grey. The color indicated that a small portion of the flux was soluble in the BSO and occupied Ba and Sn positions in the lattice as a dopant. Pb-doping was also evident in the decrease in carrier mobility - 103 $cm^2V^{-1}s^{-1}$ at room temperature. Crystals doped with 4% lanthanum showed $La_2Sn_2O_7$ XRD patterns. Therefore, it was argued that lanthanum solubility does not exceed 4 %. This was contradicted in later years by demonstrating La solubility of 5 – 7 %, depending on whether LBSO was oxygen-depleted or not. Crystals were also heat-treated to evaluate oxygen stability and its effect

on electrical properties. Crystal annealing at 1300 °C in nitrogen or argon increased oxygen vacancies' concentration and improved the electrical properties [1, 120]. It was demonstrated that the resistance could be modified depending on the annealing atmosphere, lowering in oxygen-rich and increasing in oxygen-free atmospheres. The benefits of LBSO annealing was also discussed in numerous publications [23, 121-123].

Sb-doped $BaSnO_3$ crystals were also prepared using the Cu_2O flux method. Similar experimental conditions were applied. BSSO crystal also showed n-type semiconductor properties in a degenerate doping regime. The highest mobility was found to be 79.4 $cm^2V^{-1}s^{-1}$ in a carrier density of 1.02×10^{20} cm^{-3}. The prepared crystals were mainly black. Although, measurements of optical transmission suggested that BSSO could become transparent in a thin-film state. It was well established that a $Ba(Sb,Sn)O_3$ system showed a steep decrease in mobility with the increase of carrier density. This relationship could be expressed as $\mu \sim n^{-1}$. The increase of carrier density lowered the mobility 2 – 5 times compared to $(Ba,La)SnO_3$ system. Based on this behavior, it was argued that electron scattering due to neutral impurity scattering exists significantly in the BSSO system in addition to ionized dopant scattering. Only the latter seems to be dominant in $(Ba,La)SnO_3$ system. The presence of Sb dopants in the middle of the SnO_6 octahedral network's conduction paths was attributed to the increase of free carrier-trapping. The main implications of this study were that Ba-site doping was more effective than the Sn-site doping in order to realize high electrical mobility in the doped BSO system [124].

The melt growth method was also demonstrated to succeed in the synthesis of LBSO [125]. The stoichiometric ratio of $BaCO_3$ and SnO_2 was used with an additional 10 % SnO_2 and La_2O_3. Because $BaSnO_3$ is unstable in very high temperatures, a surplus amount of SnO_2 was added. In a temperature higher than 1300 °C, SnO_2 decomposes to $SnO + ½ O_2$. The decomposition was slightly suppressed using higher pressure of oxygen in the inductively heated iridium crucible. LBSO crystals of larger dimensions (~5×5×5 mm) were produced. Depiction of 4 cm Ir crucibles and obtained melts is given in Fig. 5. XRD 2θ scans and rocking curve measurements confirmed the pure phase and high crystalline quality (FWHM = 0.007 °). Measured electrical parameters were consistent with previous flux-grown LBSO crystals showing electron mobility values scattering in an uncorrelated way over a range from 200 to 300 $cm^2V^{-1}s^{-1}$ for electron concentrations between 1×10^{19} cm^{-3} and 4×10^{20} cm^{-3}. Due to the larger scale and comparable results, the melt growth method might be a viable route to LBSO substrate synthesis.

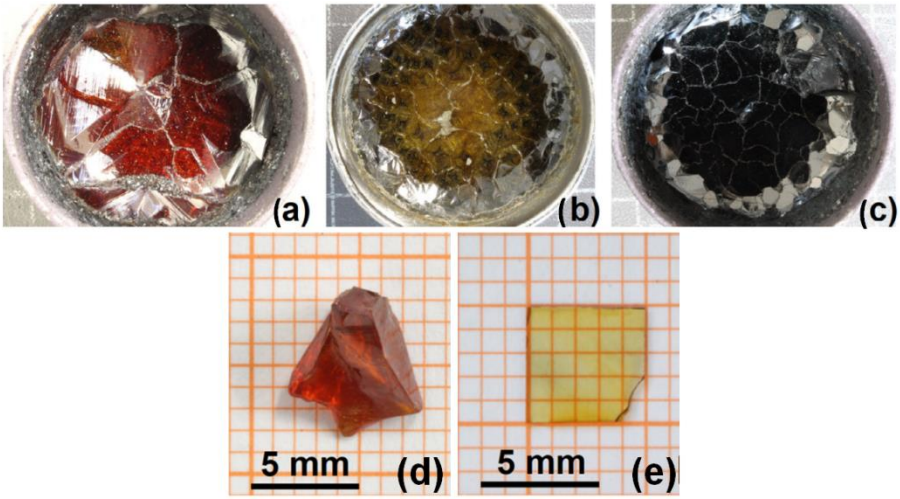

Fig. 5. Undoped $BaSnO_3$ obtained at 1858 °C (a) and 1987 °C (b), and La-doped $BaSnO_3$ obtained at 1915 °C (c). The material is within an Ir crucible of inner diameter of 4 cm. Undoped bulk $BaSnO_3$ single crystals: (d) irregular (approximately 6 × 6 × 5 mm^3) after annealing at 1200 °C in air for 40 h, and (e) polished wafer of 5 × 5 × 0.3 mm^3 from an as-grown crystal [125].

One necessary step for future applications of the La-doped $BaSnO_3$ system is the ability to grow high-quality thin films with high mobility (μ). In 2012, epitaxial LBSO films (200 nm) were deposited on $SrTiO_3$ substrates using pulsed laser deposition (PLD), using $BaSnO_3$, $Ba_{0.96}La_{0.04}SnO_3$, and $Ba_{0.93}La_{0.07}SnO_3$ targets. Thin films were grown in an O_2 pressure of 0.1 Torr at 750 °C. After the deposition, the samples were cooled in oxygen at a pressure of 0.6 Torr. [1]. Film structural investigation showed well-oriented epitaxial films without any impurity phase. An interesting trend was noticed, showing a decrease in films' μ when n decreases but an increase in μ in single-crystals as n decreases. This opposite behavior can be attributed to many grain boundaries and dislocations present in the films. It was argued that structural defects acted as carrier trapping and scattering centers and decreased n and μ simultaneously. Even with number scattering centers, a μ of 70 $cm^2V^{-1}s^{-1}$ was reported. Another issue regarding mobility was the crystallinity of the films. Wang et al. deposited thin LBSO films (300 nm) on $SrTiO_3$ (100) and MgO (100) substrates using a 248nm KrF laser ablation method and $Ba_{0.93}La_{0.07}SnO_3$ targets. Deposition temperature was kept at 600-760 °C and $p(O_2)$= 10 – 40 Pa. Even though single-phase LBSO films were deposited, the achieved mobility was much lower, reaching a maximum value

of 0.69 $cm^2V^{-1}s^{-1}$. However, the FWHM of the rocking curve was 0.57 °, whereas it was 0.09 ° in Kim's et al. work. Therefore, the mobility was largely associated with superior structural properties [119, 126].

Liu et al. investigated the composition-dependent metal-semiconductor transition by depositing thin LBSO films also by laser ablation method [127]. Ablation targets were prepared using a conventional solid-state reaction between $BaCO_3$, SnO_2, and La_2O_3. Ceramic ($La_xBa_{1-x}SnO_3$, x=0; 0.02; 0.05; 0.07; 0.10; 0.15; 0.20) targets were acquired using final sintering temperature of 1450 °C. During the deposition, the temperature and oxygen pressure were kept at 780 °C and 20 Pa. Films were later annealed at the same atmosphere. Thick films of 520 ± 30 nm were deposited. Again using laser ablation, the mobilities were not improved. The carrier density and Hall mobility were 1.79 × 10^{21}; 4.62 × 10^{21}; 5.54 × 10^{21}; 2.63 × 10^{22}; 4.09 × 10^{21}; 1.20 ×10^{21} cm^{-3}, and 0.215; 0.219; 0.923; 0.013; 0.057; 0.013 $cm^2V^{-1}s^{-1}$ for films at x = 0.02; 0.05; 0.07; 0.10; 0.15; 0.20, respectively. As MgO (100) was used as a substrate, a larger amount of defects were possibly formed. Therefore, PLD-deposited thin-film electrical properties were greatly dependent not only on deposition

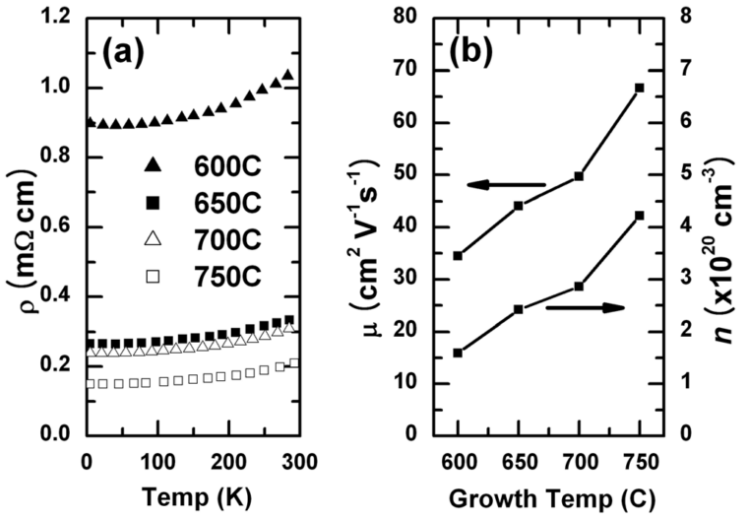

Fig. 6. (a) Resistivity–temperature curves and (b) carrier concentrations and Hall mobilities of BLSO/STO (001) films grown at various temperatures [109].

conditions but also on the substrate. In further publications about PLD-based synthesis, a lot of attention was given to dislocation density related to the substrate temperature during deposition [109]. Fig 6 (a) shows the temperature dependence of resistivity for LBSO films grown at a temperature varying from

600 °C to 750 °C. The four curves are almost parallel to each other, suggesting that additional impurity scattering increases as the growth temperature decreases. Furthermore, all specimens show metallic behavior, indicating that they are in the degenerately doped regime. In Fig. 6 (b), the BLSO films' mobilities decrease from 70 to 34 $cm^2V^{-1}s^{-1}$ as the growth temperature decreases, suggesting that there are higher densities of defects, which interrupts carrier movement in films grown at low temperatures. Better electrical properties are again related to improved crystallinity. ω-scan rocking curves of the BLSO (002) peaks were measured, showing FWHM values from 0.110 ° to 0.086 ° as the growth temperature increased (Fig 7 (a,b)). This signifies the importance of higher temperature, better lattice-matched substrate, and optimized deposition conditions when using the PLD method.

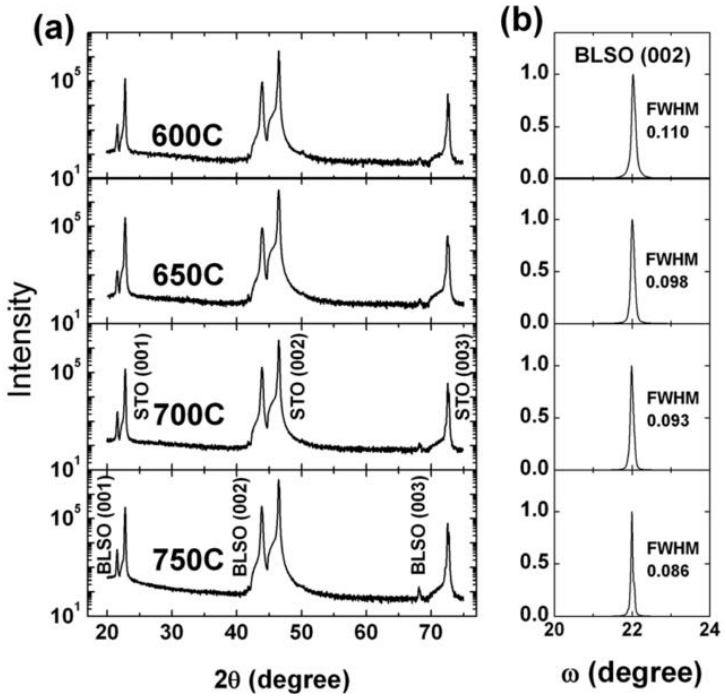

Fig. 7. (a) X-ray θ–2θ pure phase patterns of LBSO films on STO(100) substrates with different growth temperatures. (b) ω-Scan for BLSO (002) reflection [109].

In later years the PLD method was used to deposit LBSO thin films on better-matched $LaInO_3$ (LIO) substrate. Its pseudo-cubic parameters are a_{LIO}=4.124 Å, b_{LIO}=4.108 Å, while a_{LBSO}=b_{LBSO}=4.116 Å, which attributes to a lattice mismatch of -0.19 %. In comparison, the STO substrate lattice mismatch is ~5.1 %. The deposition conditions included a high temperature

of 750 °C, higher oxygen partial pressure of 100 mTorr as well as BSO buffer layer. Using LIO, BSO, and LBSO, the first reported field-effect transistor was demonstrated.

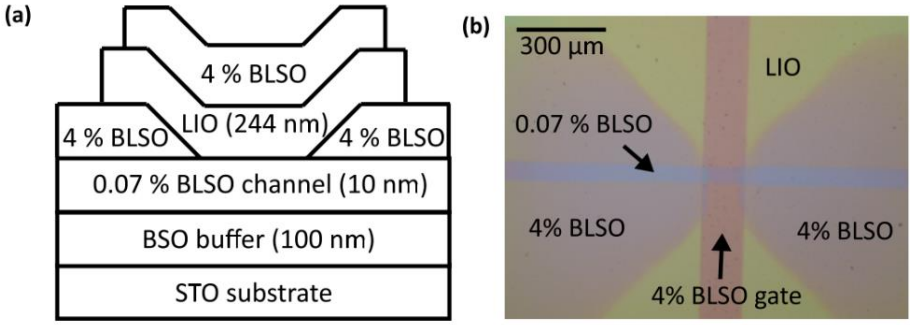

Fig. 8. Structure and I-V characteristics of the LIO/BLSO heterostructure field-effect device. (a) The schematic of the structure of the field-effect transistor device is presented. (b) The top view of the device was pictured by an optical microscope [128].

The heterostructure is depicted in Fig. 8. The mobility values of LBSO in the composite structure reached 90 $cm^2V^{-1}s^{-1}$. A few years later, the PLD's progress was pushed further by depositing LBSO films on polished insulating BSO (*l*00) crystals grown using Cu_2O-CuO and $KClO_4$ flux. The temperature of 790 °C was used. Films grown on BSO substrates showed supreme crystalline orientation of rocking curve FWHM values of 0.029 ° for (002) peaks. Using grown BSO (*l*00) single crystals as a substrate, the highest reported PLD method LBSO mobility of ~100 $cm^2V^{-1}s^{-1}$ was achieved. Slightly increasing µ behavior with the decrease of *n* was qualitatively similar to the single crystal behavior [88].

One of the best film synthesis methods in terms of mobility results was the molecular beam epitaxy (MBE). To test the effect of dislocations in thin LBSO films (30 nm), a series of films with varying from 30 to 250 nm BSO buffer layer thickness were deposited on STO substrates. Dopant density in the active LBSO layer was kept constant by fixing La effusion cell temperature at 1230 °C. Fig. 9 shows room temperature carrier concentration (n_{3D}) and mobility $\mu_{300\ K}$ as a function of buffer layer thickness t_{buffer}. n_{3D} increases monotonically between 2.5×10^{20} cm^{-3} and 4×10^{20} cm^{-3}, whereas $\mu_{300\ K}$ first increases to 115 $cm^2V^{-1}s^{-1}$ at t_{buffer} = 124 nm and then decreases. The fact that n_{3D} increases with increasing t_{buffer}, which decreases dislocation density in the active layer, suggests charge compensation is operative and that threading dislocations act as acceptor-like defects. The optimal buffer layer thickness is related to buffer layer surface roughness, as a thicker layer would

induce additional structural defects from the rougher surface. The study's new outcome was that room temperature mobility in BSO films was limited by both defects and electron-phonon scattering. The study results placed doped-BSO on par with highly successful III-nitrides in terms of mobility but with the added benefit of having high carrier concentrations for high-power oxide electronics working at room temperature [112].

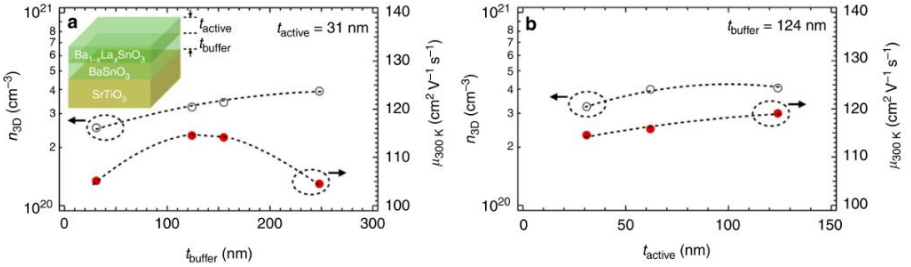

Fig. 9. Effect of buffer and active layer thickness on room temperature carrier density and mobility. A variation on n_{3D} (black open circles) an $\mu_{300\ K}$ (solid red circles) in La-doped $BaSnO_3$ films as a function of (a) t_{buffer} for fixed t_{active} = 31 nm, and (b) t_{active} for fixed t_{buffer} = 124 nm. The inset shows a schematic of the structure [112].

Further improvement in the MBE thin film synthesis was achieved by Raghavan et al. using a modified oxide molecular beam epitaxy (MBE) approach. This technique addressed issues in the MBE of ternary stannates related to volatile SnO formation [129]. In their work, all growths were performed using oxygen plasma with a beam equivalent pressures (BEP) of 1×10^{-5} Torr, and samples were cooled down under the same oxygen plasma. The growth rate was 32 nm/hour. In their study's first samples, TEM measurements showed a defective interface layer. The most likely explanation for the initial defective layer was Sn metal droplets' formation on the substrate. Sn metal droplets are a common problem in MBE of SnO_2 from an Sn metal source that has been documented before [130]. To avoid Sn formation, either the oxygen flux must be increased or more reactive oxygen species (i.e., ozone) introduced. It was argued that this would risk damaging the MBE system. More importantly, high-quality perovskite films' growth required high substrate temperatures to achieve sufficient ad-atom mobility, typically in the range of 800 – 900 °C. Growths at higher substrate temperatures (above 550 °C) avoided the droplets. Still, they caused excessive evaporation of SnO, which was also observed in the MBE of SnO_2. Sn incorporation was seen above 600 °C, but only SnO was deposited. A modified MBE approach was adopted to address these issues, namely, supplying pre-oxidized Sn from a

SnO_2 source. Only a few studies in the oxide MBE literature use the evaporation of the metal oxide from an effusion cell [131] [132]. Vapor pressure data indicated that SnO_2 sublimed in the form of suboxides (SnO_x) [133]. Supplying pre-oxidized Sn in the form of SnO_x in the presence of activated oxygen allowed for the growth of epitaxial, stoichiometric, high-quality $BaSnO_3$, showing mobility values of 150 $cm^2V^{-1}s^{-1}$ on $PrScO_3$.

In Paik's study, adsorption-controlled growth molecular beam epitaxy was used for the deposition of LBSO thin films. Barium, tin dioxide, and lanthanum effusion cells were used combined with a molecular beam of oxidant (the ~10% ozone + oxygen output of a commercial ozone generator). Films were deposited on many substrates: (100) $SrTiO_3$, (001) $DyScO_3$, (110) $DyScO_3$, (110) $TbScO_3$, (110) $GdScO_3$, (110) $Nd_{0.5}Sm_{0.5}ScO_3$, (110) $NdScO_3$, and (110) $PrScO_3$. The substrate temperature was kept between 830 °C and 850 °C. Fully relaxed epitaxial films of 320 nm on the $BaSnO_3$ buffer layer were deposited. The highest mobility values were achieved on $DyScO_3$, reaching a record of 183 $cm^2V^{-1}s^{-1}$ at room temperature in the adsorption-controlled deposition mode. It is noteworthy that $DyScO_3$ was not the best lattice-matched substrate having a mismatch value of 4.2 %. After this result, it was argued that mismatch induced dislocations and order in the deposition process were not the only parameters responsible for electrical properties. A large impact of stoichiometry was discussed as the main issue, as well as the partial pressures of the oxidant. In general, it was demonstrated that minimizing variation in the stoichiometry and achieving precise control over it might be a possible way to produce outstanding mobilities [26].

In summary, LBSO deposition (PLD, MBE) was successful using better-matched substrates and slow deposition rates. Important factors, such as dislocation density, annealing, and partial oxygen pressure during the growth process, were emphasized. A tendency of a large variation in electrical properties was demonstrated, which is most likely dependent on the stoichiometry. In respect to demonstrated results, control of stoichiometry is crucial. To achieve better control over this factor, chemical deposition methods might be a plausible solution. One such method is chemical vapor deposition, in which the supply of reactive species is supplied very precisely. Only one work by M. Veith in the area of metal-ceramic synthesis was reported in 1994. In this work, a simple MOCVD process using thermally evaporated single Sn and Ba mixed precursor bis[*tert*-butoxi-stannate(II)] ($BaSn_2(OtBu)_6$) is used. The aim of this work was not precisely $BaSnO_3$ films but a composite of $BaSnO_3$ and Sn metal. The reactor scheme is provided in Figure 10.

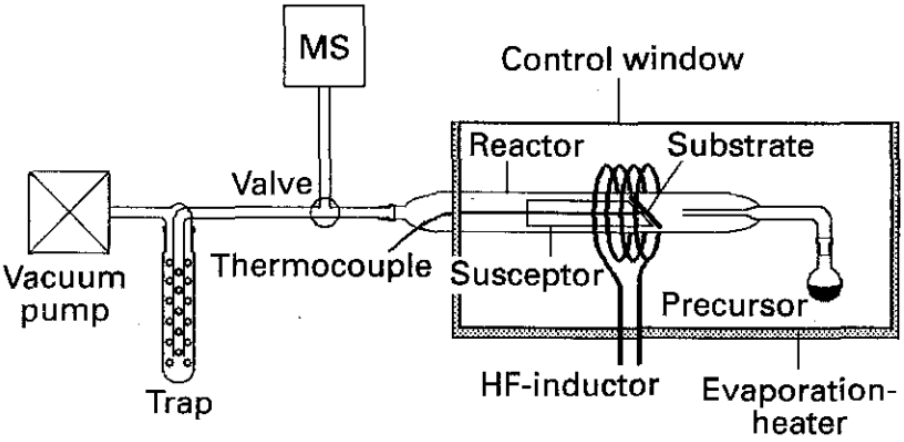

Fig. 10. Schematic of the CVD equipment. It consists of a cylindrical reaction tube in which the substrate is situated on a glass support. The whole reactor is situated in a furnace, necessary to promote the precursors' volatility at pressures of 0.1-1000 Pa. As substrates, nickel, graphite, or silicon plates are used. The substrate is heated inductively at temperatures of 300-500 °C. The temperature of the substrate is measured by a thermocouple connected to a high-frequency source. The quadrupole mass spectrometer is linked to the system and enables controlling the reaction gases [134].

In the reported experiment, ball-shaped particles were produced. EDX analysis showed a Ba:Sn ratio equal to 2. The only crystalline beta-Sn component was detected. Over a few days at 500 °C, the crystalization of $BaSnO_3$ was observed. The Sn was incorporated in the shell of $BaSnO_3$, as shown in Fig. 11. The partially successful formation of BSO is demonstrated. Therefore, a more optimized MOCVD system, such as PI-MOCVD, is hypothetically applicable for the thin film LBSO synthesis. It might provide promising results due to its superior stoichiometry control, significant control over the reaction parameters, and in-situ annealing possibilities.

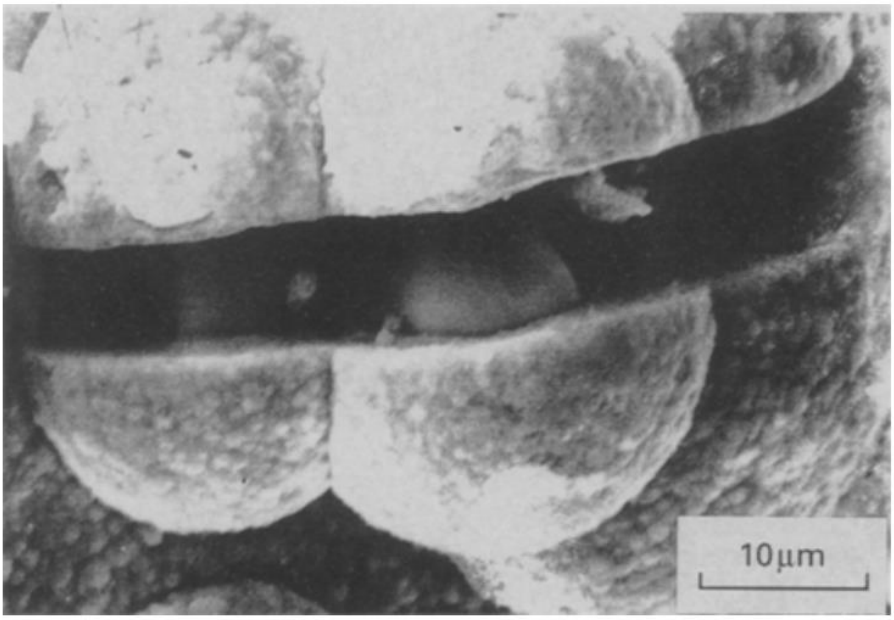

Fig. 11. Scanning Auger microscope image of the obtained composite after freezing at -195 °C. Some balls are broken in half, so the core, made up of β-Sn, can be seen inside [134].

2. EXPERIMENTAL PART

2.1. Reagents

Stannate synthesis via metalorganic chemical vapor deposition requires stable and volatile metalorganic compounds. Therefore, the following Sn, Ba, and La precursors metalorganic compounds were synthesized in Vilnius University MOCVD group laboratory by Zita Šaltytė: $Sn(acac)_2(Bu)_2$, $Sn(Bu)_2(AcO)_2$, $Sn(thd)_2$, $Ba(thd)_2*H_2O$, $Ba(thd)_2$*triglyme, $Ba(thd)_2$*tetraglyme, $La(thd)_3$*monoglyme. Different ligand-containing precursors $Sn(Bu)_4$, $Sn(O_tBu)_4$ were purchased from Strem Chemicals, Inc. $Sn(O_tBu)_2(PyTFP)_2$ (PODA) and $Sn(O_tBu)_2(DMOTFP)_2$ (PODB) were synthesized in Masaryk University, Faculty of Science, Department of Chemistry (Czech Republic) and sent in nitrogen sealed vials as probable precursors for PI-MOCVD process. 1,2-dimethoxyethane (DME) used to dissolve the precursors was purchased from Applichem, Germany. In order to prevent any undesirable reactions in the precursor solution, the DME solvent was dried over metallic sodium and distilled to remove stabilizing compounds and any traces of water.

Crystalline one/double-side polished $SrTiO_3$ (100), $LaAlO_3$ (100) (LAO), Al_2O_3 (Sapphire-C) (0006), MgO (100) substrates were purchased from CrysTec GmbH, Germany. A substrate size of 5×5 mm^2 was used in the experiments. Substrates were glued using Silver metal paste Du Pont, UK.

2.2. PI-MOCVD reactor design and principle

Thin-film deposition has been carried out using a modified metalorganic chemical vapor deposition system equipped with pulse-injection (PI-MOCVD). PI-MOCVD is a low-pressure system composed of three major temperature-controlled zones: evaporation chamber, central path, and furnace. The evaporation chamber is coupled with electronically controlled injectors that deliver microdoses of metalorganic compound solution. Precisely controlled portions of the solution are injected into the evaporation chamber where they undergo flash-evaporation. Metalorganic and solvent vapor is transported through the central path to the high-temperature reaction zone in the furnace using Ar and Ar + O_2 carrier gas. Due to high-temperature conditions and the introduced oxygen, precursor vapor decomposes, and thin oxide films are deposited onto the substrates. Crystalline substrates are glued to the sample holder using silver paste. All of the gases and products of decomposition are evacuated and condensed in the liquid nitrogen cooled

catchers. The reactor design for this thesis is given in Fig. 12. The specific conditions for each experiment will be described in each results section.

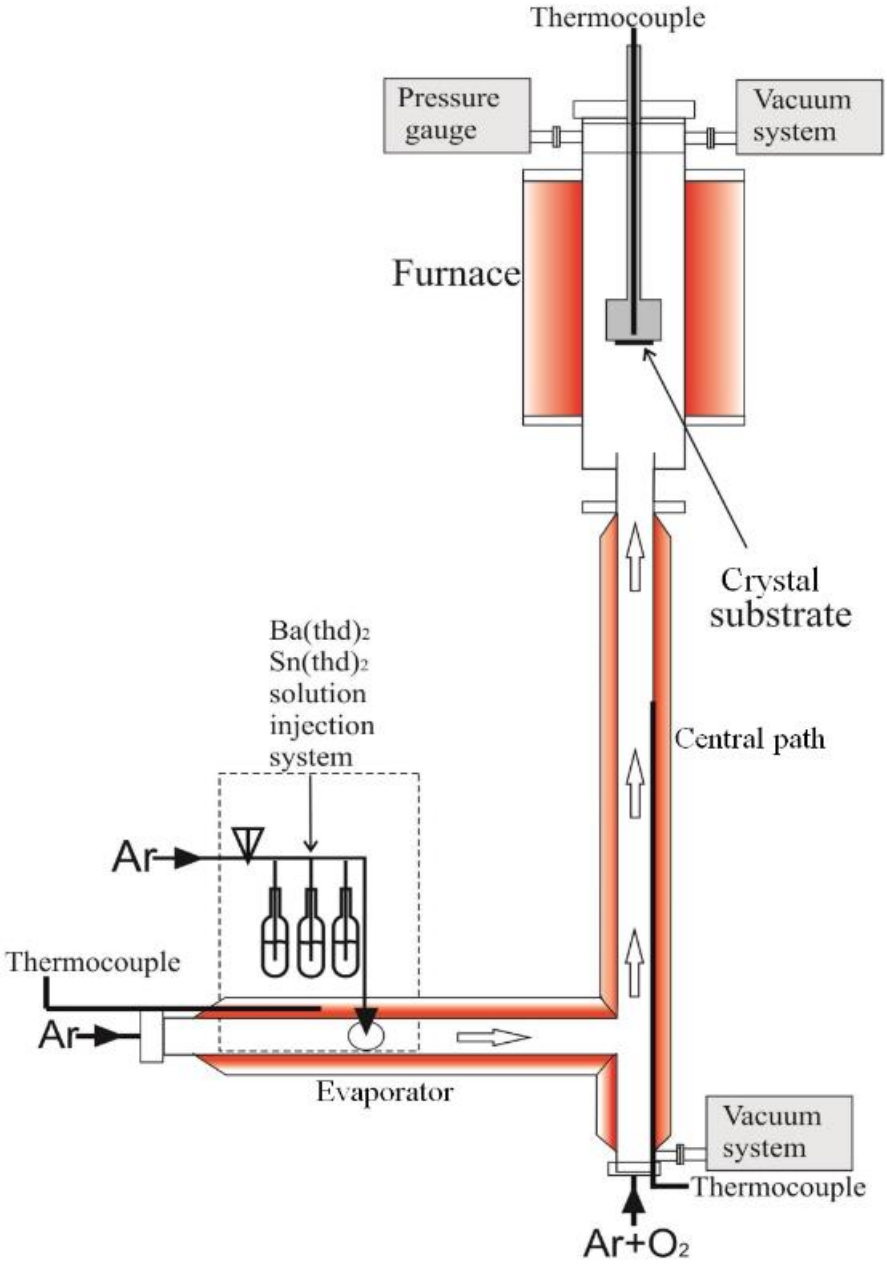

Fig. 12. Pulsed-injection metalorganic chemical vapor deposition system scheme.

2.3. Characterization of the samples

2.3.1. Thin-film X-ray diffraction analysis

X-ray diffraction (XRD) measurements of thin films discussed in this work have been carried out at room temperature using the Miniflex II tabletop diffractometer (Rigaku). θ-2θ XRD patterns have been recorded in Bragg-Brentano measuring geometry. Epitaxial samples' texture analysis and the pole figure measurements have been carried out using D8 Advance diffractometer (Bruker) with monochromatizing optics. Both diffractometers were operated with Cu anode (CuKα), linear 1D detector, and Ni metal filter. Grazing incidence X-ray (GIXRD) experiments were performed for polycrystalline samples using D8 Advance (Bruker) diffractometer with Goebel mirror monochromatizing optics at an angle of $\alpha = 0.45$ °.

Lattice parameters of epitaxial samples were determined in a specific sequence. First, the reflection angle (2θ) of (200) crystallographic plane was refined for MgO, $LaAlO_3$, $SrTiO_3$ crystalline substrates to obtain the highest signal intensity of the substrate. After the 2θ refinement, the Ψ angle was checked and optimized. The samples in the refined Bragg conditions were then measured to acquire a thin-film lattice parameter. The acquired patterns were analyzed by aligning the substrate (200) peaks at fixed values and by the deconvolution of the XRD patterns using Bruker's TOPAS software package. LeBail method was used for the deconvolution and modeling of the data.

2.3.2. Scanning electron microscopy and energy-dispersive X-ray spectroscopy

To acquire detailed surface images of deposited films, Hitachi SU70 Analytical scanning electron microscope (SEM) with cold field-emission source has been used. The accelerating voltage was varied from 5 kV to 15 kV. SEM TM 3000 tabletop microscope (Hitachi) was routinely used to determine and monitor the samples' approximate elemental composition. Energy dispersive X-ray analysis (EDX) spectra were collected using an accumulation time of 5 min measuring the largest possible surface area of the sample. Spectra were recorded using a silicon drift detector (Si(Li)) cooled by the Peltier element.

2.3.3. Transmission electron microscopy

Structural high-resolution transmission electron microscopy (TEM) measurements of the films formed on STO substrates were carried out by Tecnai G2 F20 X-TWIN TEM (FEI) operating at 200 kV. Helios Nanolab 650 dual beam microscope (FEI) equipped with an Omniprobe manipulator was used to prepare the cross-sectional TEM specimens. TEM lamella thickness was determined to be 60 nm by using convergent beam electron diffraction pattern analysis.

2.3.4. Atomic force microscopy and profilometry

The samples' surface roughness was measured using the Nanoscope III scanning atomic force microscope (Veeco) (AFM) in the intermittent contact mode. Sample thickness was also determined using the Taylor-Hobson profilometer measuring through the etched sample surface.

2.3.5. UV-VIS and Variable angle spectroscopic ellipsometry

The optical properties of thin films were characterized in the UV-Visible range. Transmission measurements have been carried out using PerkinElmer Lambda 35 spectrometer in the range of 190-1000 nm. A variable angle spectroscopic ellipsometry (VASE) technique was performed on J.A. Wollam M-2000 spectroscopic ellipsometer with a rotating compensator. VASE was used to determine the thickness of the sample films. The samples were measured using three incident angles of 65 °, 70 °, 75 °. A model consisting of three Lorentz oscillators and one Drude component was used to analyze barium stannate and La-doped barium stannate thin films. The model included in the original software was used to determine the thickness of thin oxide films.

2.3.6. Thermogravimetric analysis

The thermal decomposition of tin, barium, lanthanum metalorganic precursors was analyzed using thermogravimetry and differential scanning calorimetry (TG-DSC) analysis. 20 mg of each precursor sample sealed in nitrogen vials were transported into Perkin Elmer STA 6000 Simultaneous Thermal Analyzer and heated from 25 to 450 – 550 °C at a heating rate of 5 °C/min in dry flowing nitrogen (20 mL/min). The thermal behavior of the precursors was analyzed through simultaneous thermogravimetry and

differential thermal analysis (TGA-DTA) to evaluate combustibility, volatility and to determine the residual solids after the heating process.

2.3.7. Electrical measurements of conductive LBSO samples

The electrical characterization of the samples was carried out using the standardized Van der Pauw four-probe method, according to the National Institute of Standards and Technology (NIST, Germany). Electrical contacts on the samples were formed using liquid InGa alloy in four corners of the samples. The Hall measurements took place in a magnetic field of 0.57 T. To minimize and increase Hall measurements' sensitivity, novel and fully automatic system was constructed to switch the magnetic field directions. Using this system, thin LBSO film carrier mobility, resistance, and carrier concentration were investigated.

3. RESULTS AND DISCUSSION

3.1. Analysis and selection of metalorganic precursors for tin-based oxide materials

The significant impact of the MOCVD synthesis of multicomponent oxide layers has the choice of metalorganic (MO) precursors. In the classical MOCVD process, the volatile MO compound is evaporated at a certain temperature. The vapors are transferred to a hot substrate, where their decomposition occurs, and the oxide layer is formed. In the case of multicomponent oxide layers, MO complexes' vapor decomposition rates and thermal stability are different. The vapor phase and, consequently, the composition of the layer depend on their compatibility. In addition, the PI-MOCVD method is described as a single liquid-vapor source MOCVD. In this case, the MO precursors are firstly dissolved in an organic solvent. Because microdose spraying requires injections, one of the key requirements is the transparency of the solution. Thus, the main criteria for MO compounds are volatility, thermal stability, and compatibility with each other both in solution and in the vapor phase. To evaluate the precursor suitability, TGA and mixing of the precursor solutions were used. Additionally, tin kinetics of tin precursor decomposition were investigated by depositing thin SnO_2 at various temperatures.

3.1.1. Thermogravimetric analysis and comparison of metalorganic precursors

The basis of metalorganic chemical vapor deposition is the evaporation of metalorganic compounds as precursors. To synthesize thin barium stannate films, various tin, barium, and lanthanum precursors were tested using thermogravimetric analysis. This analysis is very useful in optimizing the evaporator temperatures for the deposition process. Also, all of the compounds were dissolved in DME and mixed in pairs to determine whether a stable solution without any solid residue could be formed. Due to PI-MOCVD reactor construction, only soluble precursors can be used.

Barium precursor $Ba(thd)_2$ has been selected due to its previous use in PI-MOCVD synthesis of high-temperature superconductor yttrium barium copper oxide. $Ba(thd)_2$ was also suitable due to its moderate vapor pressure, stability in the air, and solubility in DME solvent [6, 135]. Adducts used with $Ba(thd)_2$ prolong its shelf-life and prevent degradation. When heated, the first decrease of mass, as shown in Fig. 13 (a), is related to adduct loss. H_2O,

triglyme, and tetraglyme adducts are removed in respective temperatures of 60 – 127 °C, 95 – 220 °C, 120 – 250 °C. The increasing temperatures and wider loss intervals are related to the increasing molecular masses and boiling temperatures of each respective adduct [136]. Following the loss of stabilizing additives, a steep decrease of mass related to the evaporation and decomposition occurs. $Ba(thd)_2*2H_2O$, $Ba(thd)_2$*triglyme, $Ba(thd)_2$*tetraglyme precursors demonstrate low percentage of solid residue of 15.1 %, 13.2 %, 6.6 % respectively. Even though tetraglyme adduct shows the lowest residue, a precursor with triglyme adduct has been selected for further experiments due to clear and stable DME solutions and its compatibility with tin, lanthanum precursors.

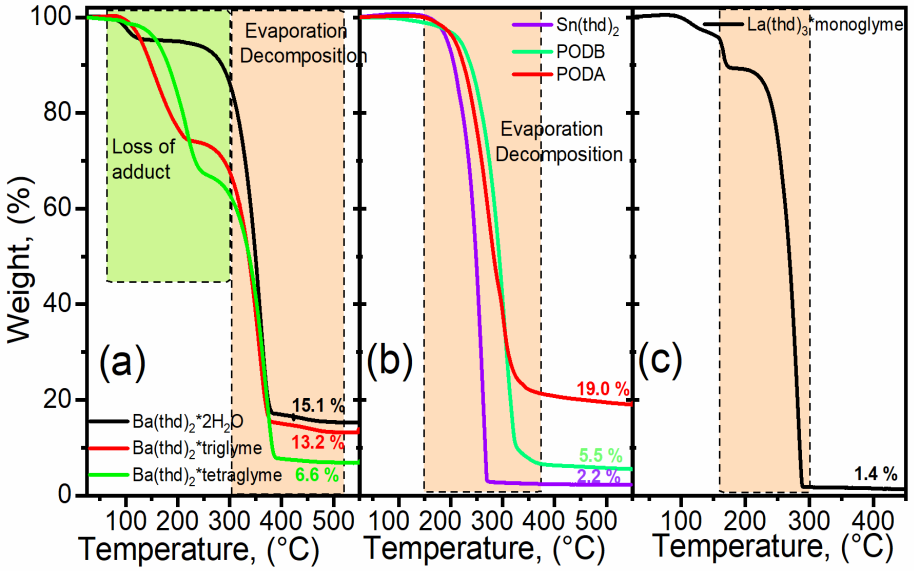

Fig. 13. TGA curves of metalorganic precursors: (a) $Ba(thd)_2$ with water, triglyme, tetraglyme adducts; (b) $Sn(thd)_2$, PODA, and PODB; (c) $La(thd)_3$ with monoglyme adduct.

A great variety of tin precursors has been tested in order to obtain suitable tin compound compatible with barium and lanthanum compounds: $Sn(OtBu)_4$, $Sn(AcO)_2(Bu)_2$, $Sn(Bu)_2(acac)_2$, $Sn(thd)_2$, $Sn(OtBu)_2(PTFP)_2$ (PODA) and $Sn(OtBu)_2(OTFP)_2$ (PODB). $Sn(OtBu)_4$, $Sn(AcO)_2(Bu)_2$ have been eliminated due to instability and sensitivity to air and moisture. Also, none of these compounds were compatible with Ba or La precursors and formed a precipitate. $Sn(Bu)_2(acac)_2$ is liquid at room temperature and was not very convenient to handle, but formed clear solutions with other Ba and La precursors. Although, due to its liquid form, it has not been tested using TGA.

Thermogravimetric analysis has been carried out only for solid and moderately reactive compounds - $Sn(thd)_2$, PODA, PODB. Each compound demonstrated only evaporation/decomposition with respective residual masses of 2.2 %, 19.0 %, 5.5 %, (Fig 13 (b)). However, a larger residual mass was observed in the PODA case, making it unsuitable for its further applications. For further CVD experiments, the liquid $Sn(Bu)_2(acac)_2$, and solid PODA, PODB, $Sn(thd)_2$ were used.

Lanthanum metalorganic compound $La(thd)_3$*monoglyme was also tested using thermogravimetric analysis (Fig. 13 (c)). The residual solvent or adsorbed water evaporated in the temperature range of 100 – 145 °C, followed by the adduct's loss at 145 – 180 °C. Evaporation/decomposition step for $La(thd)_3$ occurs at 210 – 280 °C. Only a small residual of 1.4 % indicated thermal stability.

3.1.2. Tin oxide thin film deposition and characterization

To test the suitability of tin precursors for further mixed stannate oxide synthesis, a series of depositions were carried out using four different precursors: $Sn(thd)_2$, PODA, PODB, and $Sn(Bu)_2(acac)_2$. $Sn(Bu)_2(acac)_2$ was selected as a commercially available comparison due to its prior application in $CdSnO_3$ thin film synthesis [137]. Successful barium stannate depositions using PLD or MBE methods reported high substrate temperatures reaching 850 °C [47]. Therefore, various deposition temperatures ranging from 400 °C to 900 °C were used for the deposition of SnO – SnO_2 oxides. Optimized conditions used in the experiments are given in Table 1.

Table 1. Deposition parameters used for the deposition of thin SnO_2 films.

Solvent	Solvent vol., (ml)	Conc., (M)	Evap. T, (°C)	Substrate T, (°C)	$Ar+O_2$ press., (Torr)	O_2 press., (Torr)	Injection freq., (Hz)	Injectors	Gas flow, (ml/min)
DME	10-15	0.01	200	400-900	10	2	2	1	1000

Thin oxide films were deposited on double-side polished Al_2O_3 (Sapphire-C) (0006) substrates, which are highly resistant to high temperatures and transparent in the UV-Vis-IR spectra region. Samples were analyzed using X-ray diffraction. The main properties of SnO_2 films deposited at different temperatures are presented in Table 2.

Table 2. SnO_2 thin film growth and structural properties using different deposition temperatures ranging from 400 °C to 900 °C.

Precursor	Temp., (°C)	Thickn., (nm)	Growth rate v, (nm/min)	Rough-ness, (nm)	Lattice param. *a*, (Å)	ω-scan FWHM, (°)	φ-scan FWHM, (°)	Bandgap, (eV)
PODA	600	151	6.4	3.3	4.682	0.18	4.72	4.06
	700	152	11.9	2.8	4.705	0.26	5.56	4.07
	800	172	11.7	2.5	4.730	0.34	6.85	4.07
	900	168	13.2	>20	4.745	0.16	1.43	4.06
PODB	600	91	10.6	6.6	4.695	0.33	4.41	3.89
	700	152	10.6	2.2	4.696	0.20	5.60	4.10
	800	185	13.3	2.5	4.729	0.30	7.26	4.09
	900	238	15.3	>20	4.745	0.23	1.30	3.73
$Sn(Bu)_2(acac)_2$	600	160	10.0	3.3	4.687	0.29	4.63	4.01
	700	166	10.9	4.7	4.715	0.24	6.71	4.04
	800	150	12.8	6.9	4.738	0.41	7.61	4.07
	900	244	12.4	>20	4.737	0.27	4.88	4.08
$Sn(thd)_2$	600	117	7.7	3.0	4.687	0.26	4.65	3.99
	700	137	8.9	25.7	4.700	0.19	7.61	3.71
	800	162	10.5	11.5	4.732	0.82	6.53	4.09
	900	145	9.1	12.8	4.742	0.26	4.32	3.95

Films grown from all four precursors in the temperature range of 600 – 900 °C were well crystallized and contained (*l*00) textured and in-plane oriented crystallites. This is demonstrated in Figure 14 (b), taking the films grown from PODA as an example. Presented XRD patterns show dominating (200) and (400) peaks of the tetragonal SnO_2 phase. A shift of the peaks to the left may be visible when the growth temperature increases, demonstrating the lattice *a* parameter's increase, which gradually approaches the value of the bulk stoichiometric SnO_2 (4.74 Å). A similar effect was observed in other reports. This effect is attributed to either an increased strain relaxation of the films at higher deposition temperatures or that films grown at lower temperatures are oxygen deficient [138, 139]. The well-defined in-plane orientation of SnO_2 crystallites was visible in XRD φ-scans for (101) reflection (not shown here). Very similar XRD results were obtained for SnO_2 films, grown on Al_2O_3 substrates by pulsed laser deposition [140]. Full width at half maximum (FWHM) values of XRD rocking curves (ω-scans) for SnO_2 (200) reflection varied in the range of 0.15 – 0.4 °, without any dependency

on precursor and deposition temperature (Table 2). The films obtained from the new precursors exhibited slightly smaller FWHM values of peaks in (101) φ-scans compared to the films from the commercial precursor. The films grown using PODA and PODB at 900 °C had the best in-plane orientation among deposited films. However, the surface of all films produced at such high temperatures was rough (AFM roughness average R_a >10 nm, Table 2). The lowest surface roughness (R_a ~ 2 – 3 nm) was measured for the films deposited from PODA and PODB at 700 – 800 °C (Table 2).

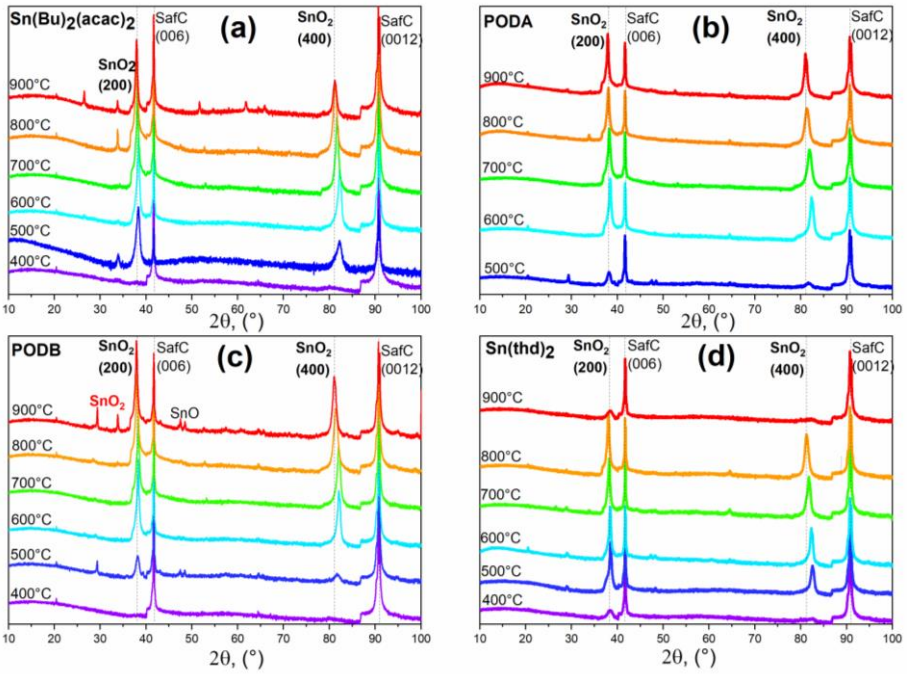

Fig. 14. XRD patterns of thin SnO_2 films deposited on the Al_2O_3 (0006) substrate using different deposition temperatures. Precursors used: (a) $Sn(Bu)_2(acac)_2$; (b) PODA; (c) PODB; (d) $Sn(thd)_2$. SnO_2 phase PDF card nr.: 00-041-1445.

3.1.3. Metalorganic tin precursor kinetics in PI-MOCVD thin film growth

In the PI-MOCVD process, precursors' thermal stability is an important factor determining the film growth rate at different temperatures. Figure 15 shows the SnO_2 growth rate (v, nm/min) as a function of the substrate temperature, presented as Arrhenius plots.

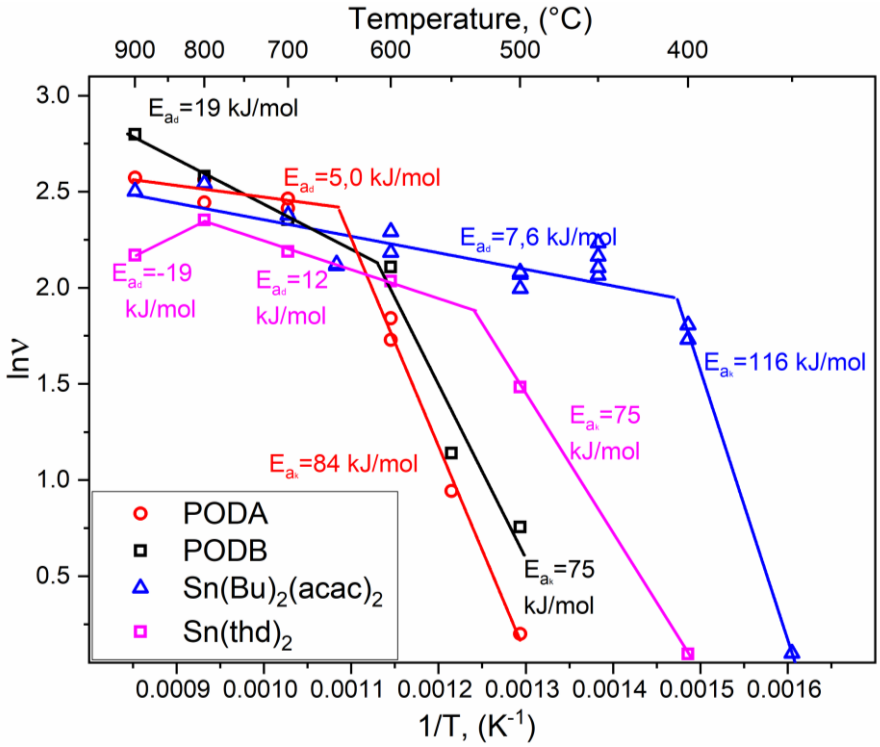

Fig. 15. SnO_2 thin film growth kinetics using PODA, PODB, $Sn(Bu)_2(acac)_2$, $Sn(thd)_2$ metalorganic precursors. Growth kinetics are represented as Arrhenius plots.

Three main regions might be visible in these graphs. At lower temperatures, the growth rate rapidly increases with temperature. In this kinetic region, the film growth rate is mainly determined by the thermally activated decomposition process of precursors at the substrate surface. At higher temperatures, the film growth rate becomes less dependent on temperature and is limited mainly by diffusion of precursor molecules to the substrate surface. The positions of the kinetic regions in the temperature scale show higher thermal stability of the newly synthesized precursors PODA, PODB, and $Sn(thd)_2$, so the film growth requires higher temperatures than when using the commercial $Sn(Bu)_2(acac)_2$. Higher thermal stability of new precursors may be a useful property in the case of deposition of complex tin-containing perovskite materials (e.g., stannates), which usually require high deposition temperatures [26]. All new precursors showed somewhat similar thermal behavior in the PI-MOCVD process, with a slightly higher thermal stability for PODA. In contrast, a third decomposition in the volume region can be determined when using $Sn(thd)_2$ precursor in a temperature higher than

800 °C. The growth rate is decreasing for this precursor but should still be usable for further experiments. Due to solid-state at room temperature and higher decomposition temperature, PODA, PODB, and $Sn(thd)_2$ were selected for further stannate synthesis experiments. Only $Sn(thd)_2$ was synthesized in our laboratory and for extended experiments, its supply could easily be ensured.

Therefore, $Sn(thd)_2$, $Ba(thd)_2$*triglyme, and $La(thd)_3$*DME precursors were selected for PI-MOCVD growth and doped barium stannate layers. It should be noted that all selected precursors are synthesized in our laboratory. This ensures the availability and quality of the complexes, as well as the repeatability of the results obtained.

3.2. Thin $BaSnO_3$ and La-$BaSnO_3$ film deposition and investigation

3.2.1. Undoped barium stannate deposition optimization

Chemical vapor deposition (CVD) methods are more versatile than physical deposition methods in terms of film composition control. However, the possibilities of depositing barium stannate films by CVD methods have not been thoroughly studied. Therefore for the following research, low-pressure pulsed injection liquid CVD modification was used. This method was applied to grow various functional oxide materials, including perovskites [141, 142]. PI-MOCVD, based on the flash evaporation principle, precise precursor dosing into the reactor, provides versatile control options of thin-film composition compared to physical deposition methods. These features are of high importance, considering the importance of stoichiometry control in BSO and LBSO films. In this work, deposition conditions for epitaxial BSO films were established. The influence of deviation from stoichiometry on microstructure, morphology, optical and electrical properties was studied in a wide range of compositions.

Conditions that were used for tin oxide film deposition have been selected. Optimal precursors evaporation temperatures, carrier gas composition, and overall pressure in the reactor were kept exact to prior experiments. In order to achieve the optimal lowest synthesis temperature, the deposition chamber temperature was varied in the range of 800 – 900 °C. To grow epitaxial thin films, $SrTiO_3$ (100) and $LaAlO_3$ (100) substrates were selected. For polycrystalline films and determination of optical properties, a lattice-mismatched Al_2O_3 was used. In the first experiments, only abundant $LaAlO_3$ (100) was used. PI-MOCVD process parameters are given in Table 3.

In the initial deposition experiments, the solution's tin and barium ratio was adjusted to achieve a near-stoichiometric ratio of the films (Sn/Ba ~ 1.00). Films of 160 – 175 nm were deposited on STO, LAO, and Al_2O_3. X-ray diffraction measurements revealed that films deposited using 800 °C were of poor crystalline quality (Fig. 16). In comparison, (l00) oriented pure phase BSO films were obtained at 825 °C and higher, respectively. The lattice parameter of 0.4118 ± 0.0006 nm well corresponded with reported values [143].

Table 3. Deposition parameters of thin barium stannate films.

Solvent	Solvent vol., (ml)	Conc., (M)	Evap. T, (°C)	Substrate T, (°C)	$Ar+O_2$ press., (Torr)	O_2 press., (Torr)	Injection freq., (Hz)	Injectors	Gas flow, (ml/min)
DME	10-15	0.01	200	800-900	10	2	2	1	1000

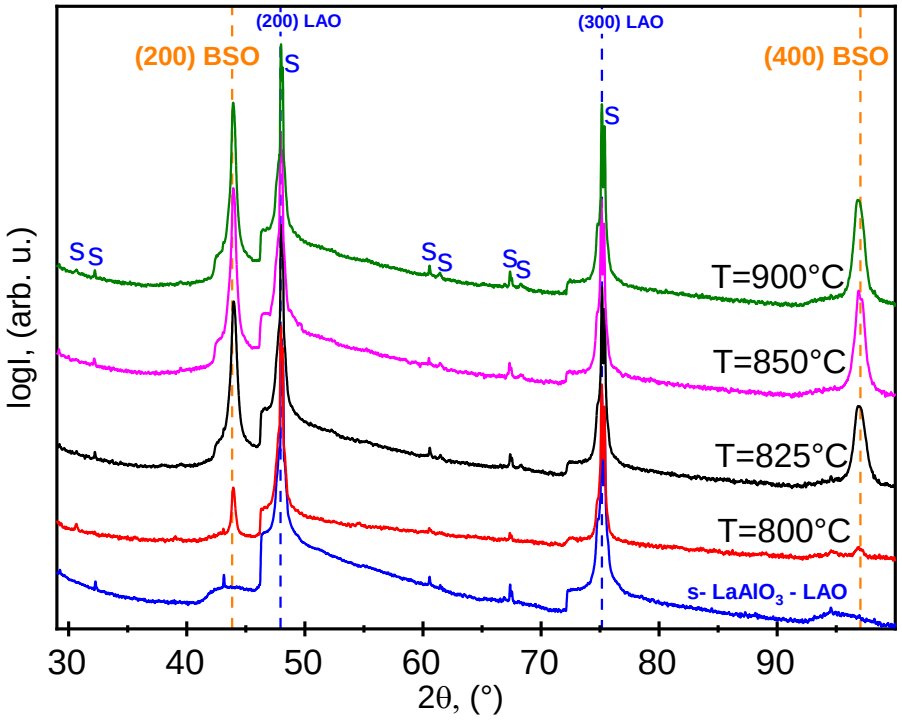

Fig. 16. (a) X-ray diffraction patterns of $BaSnO_3$ thin (~160 nm) films deposited on LAO. Substrate temperature: 800 °C, 825 °C, 850 °C, and 900 °C. Dashed orange lines: BSO reflection angles. PDF card no.: 00-042-1468. Dashed blue lines represent the scattering pattern of LAO substrate.

While XRD measurements showed similar results, SEM micrographs revealed significant morphological changes (Fig. 17). Depositions at 825 °C resulted in a vast amount of defects, possibly different crystal orientations and chaotic morphology. In comparison, films deposited at temperatures of 850 °C and 900 °C were composed of cubic compact crystallites with protruding characteristic pyramid-shaped inclusions, suggesting the formation of textured BSO films. These results show that thin film formation is limited by BSO formation temperature rather than precursor decomposition temperature or diffusion. For further experiments, the most feasible temperature of 850 °C was chosen.

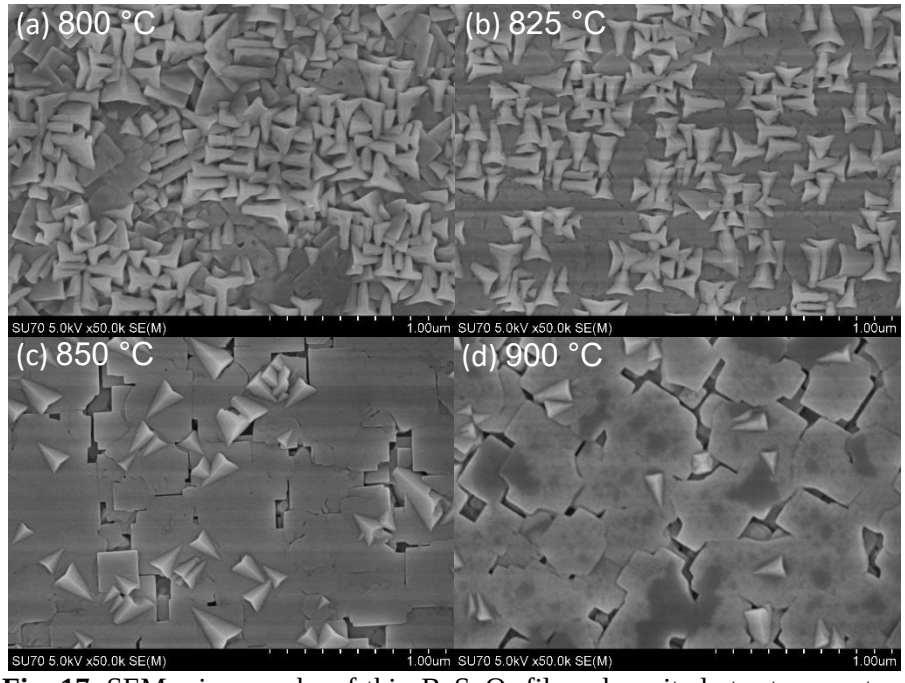

Fig. 17. SEM micrographs of thin $BaSnO_3$ films deposited at a temperature of: (a) 800 °C, (b) 825 °C, (c) 850 °C, (d) 900 °C.

3.2.2. Undoped $BaSnO_3$: stoichiometry influence on film phase composition

$BaSnO_3$ films are widely discussed in terms of crystalline quality, defects, doping effects, and conductance. However, attention to films in wide compositional range and its effects is discussed moderately [25]. This can be explained by the fact that tuning of the film composition requires the change of the target in physical methods. Therefore, stoichiometric targets are usually considered as the most suitable option. In respect, the liquid injection PI-MOCVD method offered a possibility to easily tune the film composition

and, consequently, deposited films' physical/structural properties. One of the primary aims of this dissertation was to investigate the effects of wide range nonstoichiometry on film properties. Therefore, the molar Sn/Ba ratio in the solution was adjusted from 0.3 to 0.7, resulting in film composition with nonstoichiometric molar Sn/Ba ratios of 0.54 to 1.3. In attempts to further optimize the deposition process and investigate various properties affected by layer composition, films with different Sn/Ba ratios were deposited on STO, LAO, and Al_2O_3 substrates. Parameters that could influence the results, such as gas flow rate, substrate temperature, solution injection rate, precursor net concentration, and reaction chamber pressure, were fixed. XRD thin-film crystal structure analysis carried out in Bragg–Brentano measuring geometry is given in Fig. 18. Ba-poor layer composition was primarily dominated by the cubic $BaSnO_3$ phase formation, followed by residual tetragonal SnO_2 phase. Such a result was well expected as an additional Sn precursor was not incorporated in the formation of the ternary phase.

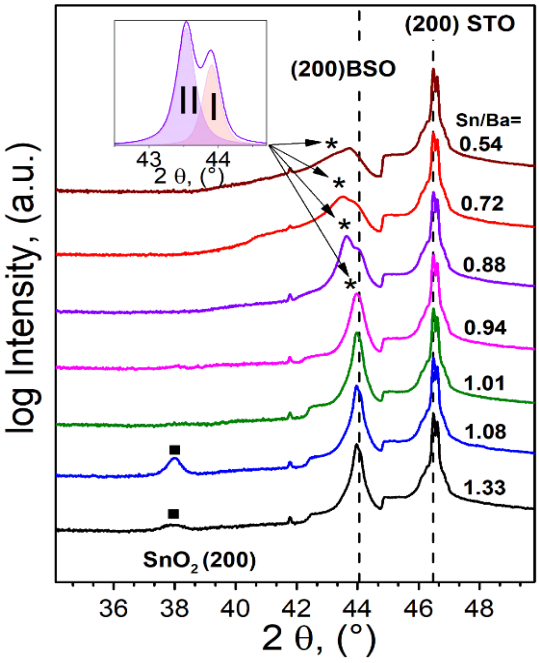

Fig. 18. Structural information of BSO films deposited at 850 °C with varying Sn/Ba ratio in the films: XRD patterns thin BSO films deposited on STO substrates with Sn/Ba ratios ranging from 0.54 to 1.3. (■) marks SnO_2, (*) marks additional reflection unresolved from BSO (200). Inset: pseudo-Voigt fitting model, where I – BSO (200) reflection, II – additional unresolved reflection.

Deposited near-stoichiometric BSO (Sn/Ba = 1.01) films were of single-phase and *a*-axis textured on STO and LAO substrates. Texture analysis revealed that films on either substrate were epitaxial. Polycrystalline film orientation was observed on the Al_2O_3 substrate. XRD measurements of Ba-rich films showed textured (*l*00) orientation of the BSO films and broadening of (200) diffraction peaks. Additionally, increasing the Ba content resulted in characteristic satellite peaks observed as Sn/Ba ratio was lower than the 0.97. Such peak splitting and broadening were consistent with two structural factors (Fig. 18):

a) Ruddlesden–Popper (RP) stacking faults are rather known to form in thin BSO films. This has been demonstrated in LBSO films deposited by PLD [123] and MBE [26] methods. RP faults are explained by periodic insertion of (BaO) periodic layers in the $BaSnO_3$ lattice on {100} planes with translational displacements of ½ a < 111 > [144]. Films with extended RP defects are described by $Ba_{n+1}Sn_nO_{3n+1}$ composition where $\infty > n > 1$ [108, 145]. In the case of Sn/Ba < 1 composition, Ba_2SnO_4 (a = 4.1411 Å) phase formation is theoretically possible, increasing the lattice parameter corresponding to satellite (l00) peak [104] (Fig. 19). Although, this hypothesis is mostly valid if the RP-phase formed planes parallel to the substrate surface and might not be enough to explain the doublet fully.

b) Substrate-film lattice mismatch at room temperature extends to ~5 % and ~8 % for STO||BSO and LAO||BSO, respectfully. High lattice mismatch in textured films is known to induce not only dislocations but can be responsible for residual strain as well. A detailed XRD study of similar perovskite $LaSrMnO_3$ thin films on STO substrates proposed a relevant in-plane strain relaxation model. It has been demonstrated that with the evolution of film thickness from 10 to 110 nm, periodic twin domains tilted by a slight angle to surface normal are formed. Such relaxation of strain resulted in X-ray satellite reflections more distinguishable in films of higher thickness [146]. Peak splitting in strained perovskite films could also originate from two different lattice structures along the growth direction – the strained layer near the substrate surface and relaxed above this strained layer [147]. Likewise, a study of perovskite $LaNiO_3$ thin films of 560 nm on the LAO substrate reported a similar strain relaxation behavior. Reported a and c lattice parameters were dependent on substrate-lattice mismatch as well as the oxygen content in the films [148]. Higher lattice mismatch produced lower peak separation. Similar results were obtained in this study. Peak separation decreased with the larger lattice mismatch, and in the case of Al_2O_3, no separation was observed. The determined increase of lattice parameter a in Ba-rich samples, could also be related to oxygen vacancy formation. Oxygen

vacancy (intrinsic defect) has low formation energy compared to possible Ba^{2+}, Sn^{4+} vacancies [77]. It should be noted that this behavior is consistent with that of V^{O} in other wide bandgap n-type TCOs, i.e., ZnO [92-94], SnO_2 [96], Ga_2O_3 [149], and In_2O_3 [150]. Oxygen vacancy formation has been demonstrated as a possible cause of the lattice parameter increase in BSO as well as other types of perovskites [151].

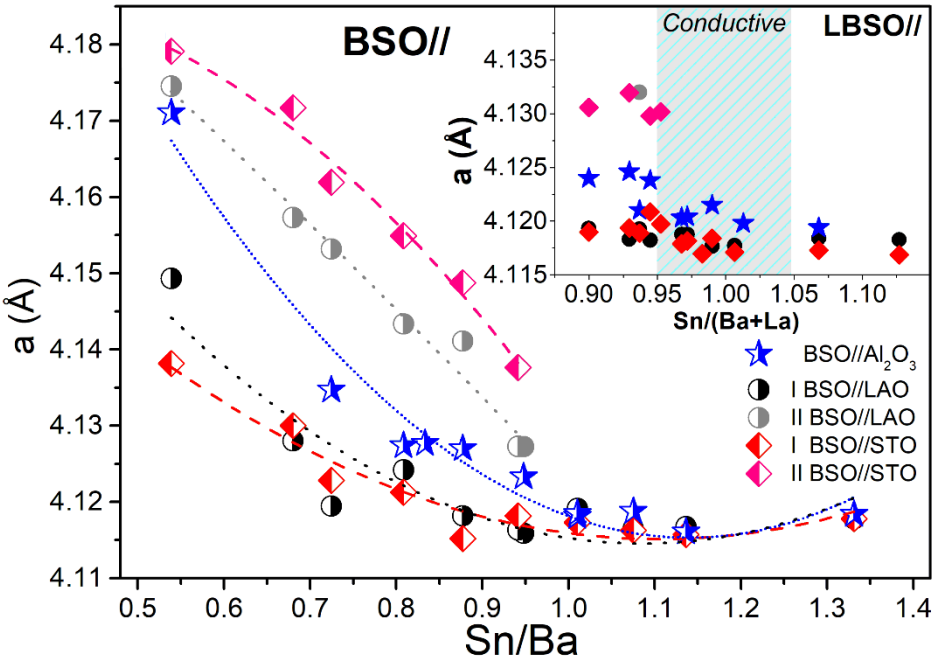

Fig. 19. Structural information of BSO films deposited at 850 °C with varying Sn/Ba ratio in the films: Pseudocubic lattice *a* parameter dependence on Sn/Ba ratio of thin BSO and LBSO films deposited on LAO, STO, and Al_2O_3 substrates. BSO on the Al_2O_3 lattice parameter was fitted using the LeBail method [22]. Inset shows near-stoichiometric LBSO film lattice *a* parameter. The grey area represents a composition region of conductive LBSO films deposited on STO substrates.

In order to check the phase purity of the films on STO and LAO, X-ray pole figures of the (110) and (200) reflections were measured using Schultz geometry (θ–θ) configuration (Fig. 20). Near-stoichiometric (Sn/Ba = 1.02) and Ba-rich (Sn/Ba = 0.81) samples were selected. Well-aligned thin BSO films were achieved in near stoichiometric composition corresponding to the full width at half maxima values of 0.3 ° and 0.8 ° measuring ω-scan (rocking curve) and φ-scan, respectfully. In comparison, an increase in barium resulted

in crystallites' disorientation with respective values of 1.0 ° and 1.5 °. Epitaxial relationship of BSO(*l*00)||STO(*l*00) and BSO(*l*00)||LAO(*l*00), for both substrates was determined. Although different low-intensity crystal orientation signals were detected for BSO samples on LAO substrates showing {221} crystal plane family reflections. {221} reflections were well defined in films with higher barium content. Such orientation crystallites were clearly observed on the film surfaces (Fig. 17 (c)). It should be noted that detailed XRD analysis of near-stoichiometric and Ba-rich thin BSO films revealed no secondary phases in a wide range of compositions. Furthermore, cubic symmetry was maintained significantly deviating from the ideal Sn/Ba ratio. This can be observed in either epitaxial and polycrystalline BSO thin films.

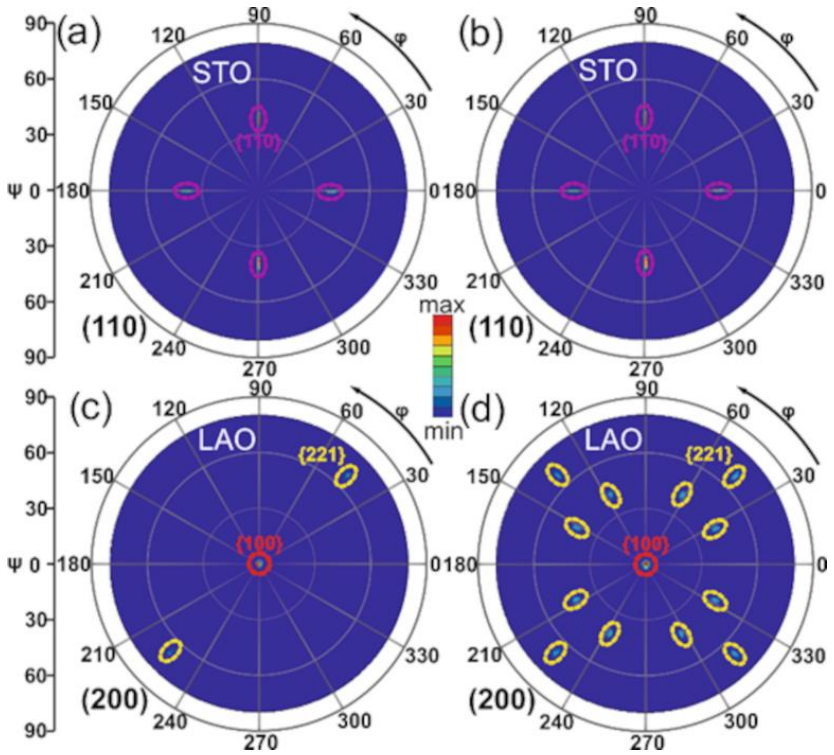

Fig. 20. (110), (200) Pole figures of thin BSO films deposited on STO, LAO substrates. (a, c) Pole figures of near-stoichiometric (Sn/Ba = 1.02). (b, d) Pole figures of Ba-rich film (Sn/Ba = 0.81).

3.2.3. Undoped and La-doped $BaSnO_3$: comparison of morphology and phase composition

In order to compare doped and undoped film properties, a series of La-doped thin films were deposited on STO, LAO, and Al_2O_3 substrates. Films of different molar Sn/(Ba + La) ratios were obtained. La content was kept at a constant doping level (2.5 ± 0.2 $\%_{atomic}$) as determined by EDX analysis. XRD diffraction analysis in Bragg–Brentano and Schultz geometry configurations revealed that La-doped thin films were similarly epitaxial on both STO and LAO. Doping at small levels had no observable effect on the lattice parameter. Its dependence on Sn/(Ba+La) ratio remained similar to undoped BSO films (Fig. 19, inset). Furthermore, XRD analysis of Ba-rich LBSO samples showed satellite (*l*00) peaks demonstrated in BSO. A clear lattice parameter increase was determined only in polycrystalline LBSO films on Al_2O_3. As La^{3+} ions radius in a 12-fold coordination (R (La^{3+}) = 1.36 Å) is smaller than Ba^{2+} ion radius (R (Ba^{2+}) = 1.61 Å) exchanging the A-site of ABO_3 perovskite structure would decrease the lattice parameter. However, only an increase of the unit cell was determined [86]. This phenomenon was known and explained by Sn^{4+} ion conversion into Sn^{2+} to maintain electric neutrality causing Sn–O bond extension. Similar results were demonstrated by Liu et al. [127]. To further investigate doping effects, both BSO and LBSO films deposited on STO substrates were investigated using scanning electron microscopy. In the case of Ba deficiency, the BSO film surface was uneven and made of small-sized separate crystallites (Fig. 21 (a)). Such film formation could be attributed to the slower nucleation process and formation of islands. Near-stoichiometric (Sn/Ba = 1.02) BSO films were uniform and compact. Although, typically defined thread dislocations terminating at the surface were clearly visible [27]. In comparison, SEM images revealed different surfaces in the case of Ba-rich composition. A uniform film matrix with protruding irregular faceted tetrahedral crystallites was observed. The density of these structural defects increased with the decreasing molar Sn/Ba ratio and could be attributed to increasing BSO||STO lattice mismatch and formation of (221) oriented crystallites.

LBSO films shown in Fig. 21 (d–f) demonstrated very similar morphologies. Although a uniform and continuous film surface was achieved at Ba-rich compositions, films of Sn/(Ba + La) = 0.97 were, in turn, the most conductive. This could be related to the lower carrier scattering due to a lesser amount of visible grain boundaries and dislocation sites. On the other hand, the most uniform surfaces were produced at slightly larger Sn/(Ba + La) ratios (~0.90), which revealed a shift in the film composition corresponding to

uniform surfaces. TEM cross-section images of the most uniform sample show columnar growth of the films typical for CVD methods [152]. It is important to notice that film is not uniform throughout its growth direction. In Fig. 21 (g) TEM image reveals two distinguishable growth regions: STO||LBSO interface followed by epitaxial layer and more defective morphology at film thickness higher than 70 nm. In the HRTEM image of the film-substrate interface, well-oriented epitaxial film growth is demonstrated (Fig. 21 (h)). However, at a larger thickness region of 70 – 170 nm, clearly visible threading dislocations have formed, seen as contrasted vertical lines. Dislocation formation is possibly the result of strain relaxation mechanism as a lattice mismatch between film and the substrate is known to induce residual stress at similar interfaces.

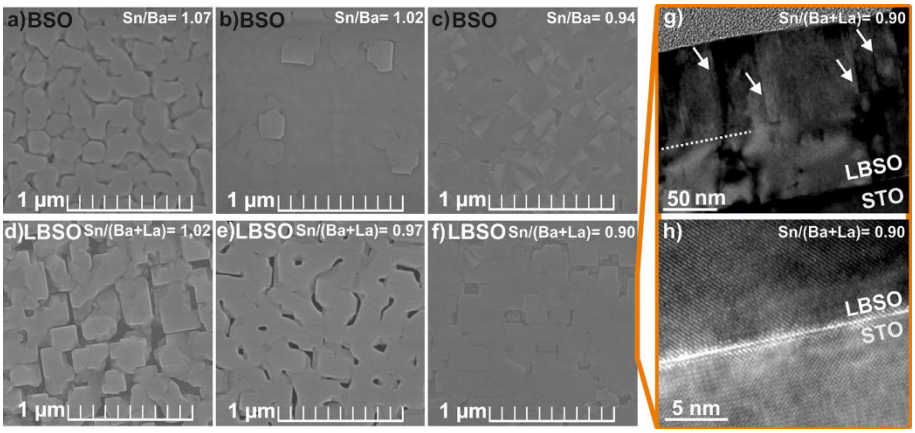

Fig. 21. Thin film, deposited on STO substrate, morphology: (a-c) SEM images of BSO film surfaces; (d-f) SEM images of LBSO film surfaces. Film composition corresponds to respective Sn/Ba (1.07; 1.02; 0.94), Sn/(Ba + La) (1.02; 0.97; 0.90) ratios. Surface roughness determined using AFM: (a) 9.7 nm, (b) 3.79 nm, (c) 9.4 nm, (d) 27.4 nm, (e) 22.0 nm, (f) 5.1 nm. (g) TEM cross-section image of LBSO film along $[l00]_{STO}$ direction. The dotted white line separates the defective region above the thickness of 70 nm. White arrows mark threading dislocations. (h) HRTEM image of epitaxial thin LBSO film-substrate interface.

3.2.4. Nonstoichiometry effect on optical and electric properties

Optical transmittance spectra of multiple thin BSO and LBSO films deposited on Al_2O_3 substrate were recorded (Fig. 22 (a)). To visualize the nonstoichiometry effect on optical properties, distinctive data points are given. For BSO and LBSO films, higher than 80 % transmittance was achieved in the visible range. In the UV region, the absorption edge was highly dependent

on film composition and shifted towards lower wavelengths as barium content increased. Calculated optical bandgap (E_g > 3.42 eV) values of near-stoichiometric films exceeded a single crystal value of 3.33 eV [1] and increased further with higher Ba content. As-grown films could be affected by high-temperature growth conditions at low pressures generating point defects, such as oxygen vacancies. Optical bandgap representing the indirect transition from the valence to conduction band could also be linked to change in A–O and B–O bonding site characteristics, which could be attributed to ionized oxygen vacancy formation and chemical expansion of the unit cell [153]. Such a result is further supported by the increasing lattice parameter tendency with increasing Ba content in the films (Fig. 19). LBSO films showed similar E_g behavior, although an overall E_g was slightly shifted to higher energies indicating Burstein–Moss effect, observed in degenerate semiconductors (Fig. 22, right inset). Hall measurements of thin LBSO films revealed that the highest values of carrier mobility (20 $cm^2V^{-1}s^{-1}$), as well as carrier density (2.6 × 10^{20} cm^{-3}), were achieved at film composition corresponding to Sn/(Ba + La) ratio of 0.97 (Fig. 22 (b, c)). Carrier mobility is usually determined by film morphology. High values were determined in the sample Fig. 21 (e) of continuous channel-like flat morphology.

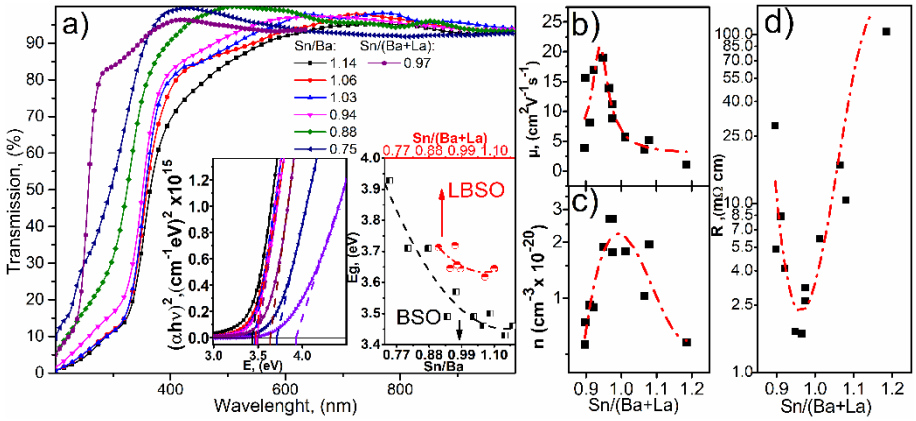

Fig. 22. Optical transmission of thin BSO and LBSO films deposited on Al_2O_3 (0006) substrates at different compositions. Left inset: Tauc plots of BSO and LBSO thin films. Right inset – bandgap dependence on different BSO (in black color) and LBSO (in red color) film compositions. Electric properties of thin LBSO films: (b) carrier mobility (μ); (c) carrier density (n); (d) specific resistance (R).

Decreasing mobility in other samples (Fig. 21 (d), (f)), on the other hand, could be attributed to an emerging grain-like structure leading to increasing carrier scattering at multiple grain boundaries. In stoichiometric n-type LBSO films, the carrier density is mostly determined by La doping in A-site (La_{Ba}^{+}). In nonstoichiometric conditions with a fixed La-doping level, an evident decrease in carrier density could be determined by two self-compensation mechanisms. In case of wide composition range conditions carrier compensation occurs by either V_{Ba}^{2-} (Sn/(Ba + La) > 1) or by La_{Sn}^{-} (Sn/(Ba+La) < 1) acceptor type defects (Fig. 22 (c)). In addition, a slight mobility and carrier concentration shift toward Ba-rich composition could probably be related to the increase of ionized oxygen vacancies in Ba-rich conditions. The highest carrier concentration and mobilities resulted in the lowest measured resistance of 1.75×10^{-3} Ωcm.

3.3. Well-optimised La-doped $BaSnO_3$ film PI-MOCVD deposition

Succesful thin (~160 nm) LBSO film synthesis has been achieved using the PI-MOCVD method. Although, the first measurements of electric properties showed low mobilities of ~ 20 $cm^2V^{-1}s^{-1}$. Such mobility values suggested that the thin film deposition process was far from optimized in terms of film morphology and control over the stoichiometry. In previous experiments, it was noticed that a solution containing both tin and barium precursors became cloudy after 24 hours. Slight precipitation, which could not be noticed in short deposition time, meant that one of the elemental species concentration varied over time, and accurate control of the film composition could not be achieved. It was determined that $Sn(thd)_2$ precursor possibly formed $Sn(OH)_2$ with the leftover water bound to $Ba(thd)_2$ metalorganic complex. The issue was solved by separating Sn precursor to different injection units, injecting Sn simultaneously with Ba and La.

Also, to enhance surface morphology, carrier gas flow was increased. In theory, this should have suppressed the diffusion layer and enhanced chemical transport at the substrate surface. The deposition parameters are given in Table 4 below.

Table 4. Deposition parameters used for the deposition of thin LBSO films.

Solvent	Solvent vol., (ml)	Conc., (M)	Evap. T, (°C)	Substrate T, (°C)	$Ar+O_2$ press., (Torr)	O_2 press., (Torr)	Injection freq., (Hz)	Injectors	Gas flow, (ml/min)
DME	40	0,019	200	850	10	1	2	2	1200

The factors mentioned above were purely technical issues related to the deposition conditions. However, further steps were needed to enhance thin films' quality and investigate LBSO sensitivity to nonstoichiometry.

A decrease in thin films' mobility could be attributed to a significant density of defects such as misfit and threading dislocations, various point defects, and residual stress. Although substrate lattice mismatch and the resulting high density of misfit and threading dislocations, among other extended defects, were discussed as the main limiting factors of carrier mobilities. In other studies, such issues were overcome by using barium stannate (BSO) buffer layers, which reduced the dislocation density [26]. A BSO layer of 330 nm was discussed as the most optimal thickness related to threading dislocations' annihilation to form only misfit dislocations. Other suggested options were high-temperature grown buffer layers of $SrZrO_3$ [154]. However, even homoepitaxial films, grown on BSO substrates, demonstrated much lower mobilities than bulk single crystals [88]. Also, it was demonstrated that LBSO film thickness played a major role in the films' mobility. Relatively thick layers of 350 nm and higher showed maximum mobility values, independently of the substrate-induced structural defects [155]. This suggests that the origin of reduced mobility is not attributed mainly to threading and misfit dislocations.

Much of the studies focused on structural defects, nearly avoiding the possibly crucial role of point defects and nonstoichiometry. Evidence that these factors are crucial in the LBSO system is the observation of different mobility values for films grown via different synthesis routes despite having similar substrates and doping concentrations [120, 156, 157]. The data on nonstoichiometry and its effects are quite scarce or partially incomplete. In this context, the following experiments on thick (~380 nm) films with widely varying elemental ratios were carried out to elucidate the role of point-defects in the LBSO system and the origin of point-defect-related properties. To compare the possible effect of substrate, STO and MgO were used as substrates with a lattice mismatch of 5.4 % and -2.3 %. A large number of nonstoichiometric samples were deposited using a modified precise control of Sn, Ba, and La. LBSO films were doped with 2.3 ± 0.3 % lanthanum. Such dopant concentration was suffiecient to achieve carrier concentration at order of $\sim 10^{20}\,cm^{-3}$.

3.3.1. Morphology of La-doped barium stannate films

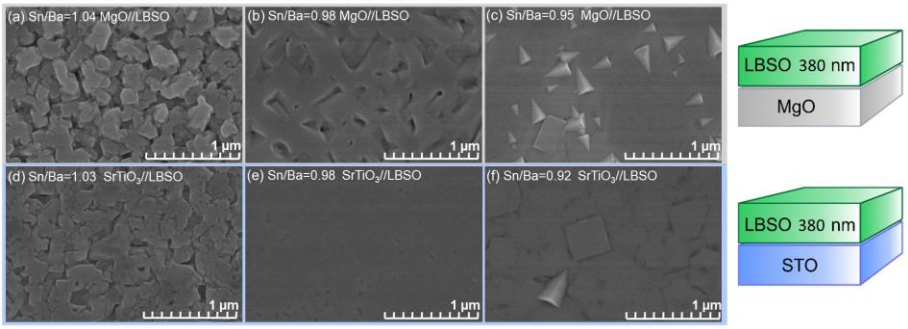

Fig. 23. SEM micrographs of thin La-doped barium stannate films deposited (a-c) MgO (*l*00) and (d-e) $SrTiO_3$ (*l*00) substrates with different molar Sn/Ba ratios corresponding to: (a) 1.04; (b) 0.98; (c) 0.95; (d) 1.03; (e) 0.98; (f) 0.92.

In an attempt to investigate the nonstoichiometry in thin LBSO films deposited in different Sn and Ba ratios, all of the samples were characterized using SEM analysis. Three distinct composition zones were observed in the epitaxial layers: Sn-rich, near stoichiometric, and Ba-rich. (Fig. 23). In the tin-rich phase region, films in any deposition conditions did not form uniform surfaces either on STO or MgO substrates, as seen in Fig. 23 (a) and (d). While films remain textured in (*l*00) plane, the surface is fragmented, and crystallites grow in rounded-like cubic columns (determined from TEM – not shown here). A small deviation from the stoichiometric composition showed no evidence of SnO_x formation. However, the tin-rich phase in larger tin quantities showed a tendency to form a SnO_x species phase, as demonstrated by other authors [24]. SnO_x formation in the BSO phase most likely hinders the formation of a periodically ordered structure as the films are grown and forms separate crystallization centers yielding a chaotic structure independent of the substrate-induced effects.

The second zone of highly ordered and homogeneous films was achieved at the Sn/Ba ratio of 0.98 shown in Fig. 23 (b) and (e). LBSO films on STO substrates demonstrated smooth surfaces with no visible features or apparent defects. The surface roughness of STO||LBSO films corresponded to 0.28 nm, as determined by atomic force microscopy. Uniform surface formation and epitaxy are likely related to ordered phase formation at the film-substrate interface and an inherently lower concentration of misfit and threading dislocations. Growth evolution in near-stoichiometric conditions is similar to the adsorption-controlled process in hybrid MBE. The overabundance of Ba, Sn, La, in near-stoichiometric ratios, and adsorption-

driven process results in nearly atomically flat surfaces. Although, at the growth rate of ~10 nm per minute, a very well controlled supply of elements is necessary. In the conditions optimized for STO-substrate, films on MgO were not nearly as smooth as expected at any deposition conditions, and minimum R_a roughness of ~5 nm was determined. In the MgO substrate case, the film is formed in a channel-like structure with deep ridges and in-grown crystallites.

The third compositional region was observed in Ba-rich conditions, producing a flat matrix on both MgO and STO substrates. However, a typical {221} orientation crystallites were visible on the sample surface, as well as misfit/threading dislocations in the form of polyhedral shapes on the surface. Typical Ba-rich morphology was already reported in thin films of ~160 nm (Section 3.1.1.). The demonstrated SEM morphologies were highly reproducible and varied consistently with varying Sn/Ba ratio in a large number of samples. It is noteworthy that the lowest roughness values and even matrix samples were produced at the near-stoichiometric composition of Sn/Ba = 0.98.

3.3.2. Microstructure of La-doped barium stannate films

Large differences in the morphology suggested that thin-film microstructure was also very sensitive to nonstoichiometry of thin films. To investigate the Sn/Ba influence, the 2θ scans were recorded for all thin films. It was determined that films on both $SrTiO_3$ and MgO substrates were of pure LBSO phase in Sn-rich and Ba-rich regions. Solely (*l*00) reflections were detected, as seen in Fig. 24 (a), typical of epitaxially grown LBSO. The most notable effect of nonstoichiometry was detected in the position of LBSO reflections. A slight shift in LBSO (200) peak was detected as thin-film composition deviated from 0.98 to Sn-rich composition. This is reflected in the LBSO out-of-plane lattice parameter *a*, which decreases only by 0.001 Å. LBSO lattice parameter is higher when using MgO substrates compared to STO at ~4.120 [127, 159]. In general, an undoped barium stannate lattice constant is reported at 4.117 Å. La-doping in the Ba position was reported to increase the lattice parameter slightly to 4.118 Å. Our LBSO||STO parameter in near stoichiometric and Sn-rich composition well agree with other author reports of stoichiometric film parameters regarding La doping of 2.3 ± 0.3 % [65, 79].

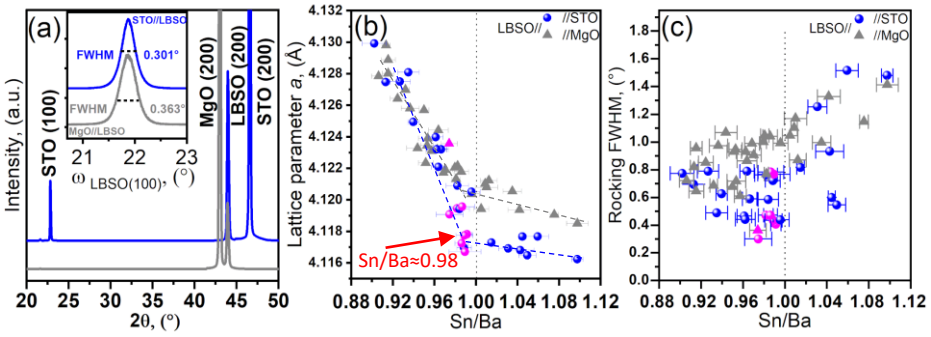

Fig. 24. XRD scans of thin La-doped $BaSnO_3$ films deposited on $SrTiO_3$ (*l*00) and MgO (*l*00) substrates: (a) θ-2θ scans of films deposited on $SrTiO_3$ (*l*00) and MgO (*l*00) substrates showing (*l*00) LBSO peaks and epitaxial growth. Inset illustrates narrow rocking curve peaks of thin LBSO films; (b) La-doped $BaSnO_3$ lattice parameter dependence on thin-film Sn/Ba ratio. Purple points mark the samples with the highest electron mobilities; (c) LBSO rocking curve (002) peak linewidth of thin La-doped $BaSnO_3$ films with different Sn/Ba ratio.

Ba-rich composition zone, however, shows two distinct tendencies. The lattice parameter in Ba-rich regions increases for both LBSO||STO and LBSO||MgO as the Sn/Ba decreases from 0.98 to 0.89, showing no particular effect of the substrate. The abrupt increase in the lattice parameter is evidently at 0.98. This break in the *a*~Sn/Ba curve signifies a crucial transition in the LBSO system. In terms of structural factors, the Sn-rich LBSO phase does not incorporate SnO_2 fragments, and the formation of SnO_x in the structure is known to interrupt the long-range periodicity of LBSO [26]. Although due to a very low deviation, SnO_x was most likely undetectable.

In contrast, the Ba-rich LBSO structure was shown to incorporate BaO layers in the structure, forming a type Rudlesden-Popper phase [108]. Theoretically, as the BaO is incorporated into the structure, the overall lattice of LBSO is increasing gradually (Fig. 24 (b)). The stoichiometric composition would theoretically be the middle-state between SnO_x and RP-phase formation in the LBSO system. Although an unexpected composition of 0.98 is the ratio for such a transition. Of course, the theoretical stoichiometry concept in La-doped LBSO is used very cautiously due to possible La incorporation in either A or B sites in the ABO_3 structure. To some extent, the B site could be occupied in the Ba-rich region. This might be supported by a similar effect described in the $SrTiO_3$ system [160]. The RP-phase formation was evident only at excessive nonstoichiometry of $Sr/Ti \geq 0.95$. The excessive strontium formed energetically favorable antisite defect Sr_{Ti}. In contrast, Ba_{Sn} antisite defects in the LBSO system were discussed as energetically

unfavorable [91]. However, La_{Sn} antisite defects were more favorable than Ba_{Sn} compared by their respective formation energies [91]. Therefore, La might arguably occupy the B site, and such antisite defect formation would explain the RP-phase formation shift to Sn/Ba ≈ 0.98 in the Ba-rich composition region.

Overall crystal orientation was investigated by measuring the rocking curves of thin LBSO film reflections. To correctly compare the film and the substrate, including all instrumental errors, ω-scans were carried out to characterize the substrates. The linewidths of 0.13 ° and 0.14 ° were determined for STO and MgO, respectively. The determined ω-scan FWHM values of LBSO (200) peaks varied from 0.30 ° (Sn/Ba ≈ 0.98) to 1.52 ° (Sn/Ba ≈ 1.06) for thin films deposited on $SrTiO_3$ substrates. In comparison, linewidths ranging from 0.36 ° (Sn/Ba ≈ 0.98) to 1.33 ° (Sn/Ba ≈ 1.04) were determined when using MgO substrates. φ-scans of LBSO (101) planes of films on $SrTiO_3$ and MgO were also recorded showing similar distribution, with FWHM values ranging from 0.60 ° to 2.35 ° with lowest values at Sn/Ba ≈ 0.98. In both STO and MgO cases, thin films' highest crystalline order was achieved at slightly Ba-rich composition demonstrated in Fig. 24 (c). The deviation from Sn/Ba ≈ 0.98 composition increased the disorder in the thin films. This is well illustrated in already shown surface morphology, which becomes more chaotic at highly Ba-rich and Sn-rich samples. The highly ordered thin films had the best electron mobility properties as well as carrier mobility values.

3.3.3. Electric properties of La-doped barium stannate films

The Hall-effect measurements confirmed that the LBSO films behave as n-type electric conductors. It was determined that thin-film electrical properties, such as carrier density and mobility μ, were highly dependent on thin films' composition at room temperature. At the optimal composition of Sn/Ba ≈ 0.98, high carrier density and high mobility values were determined. Mobility of $\mu = 121\ cm^2V^{-1}s^{-1}$ and $\mu = 85\ cm^2V^{-1}s^{-1}$ at carried density of $n = 3.0 \times 10^{20}\ cm^{-3}$ and $n = 2.2 \times 10^{20}\ cm^{-3}$ were achieved using STO and MgO substrates, respectively (Fig. 25 (a)). Such mobility values are comparable to MBE deposited films [26]. Although thin films were grown at considerably high growth rates of 5 nm/min and exhibit a lower microstructural quality compared to those obtained when using MBE.

Characterization of electrical properties highly correlated to the film nonstoichiometry. The highest mobility values were achieved in a narrow compositional region with Sn/Ba ~ 0.98.

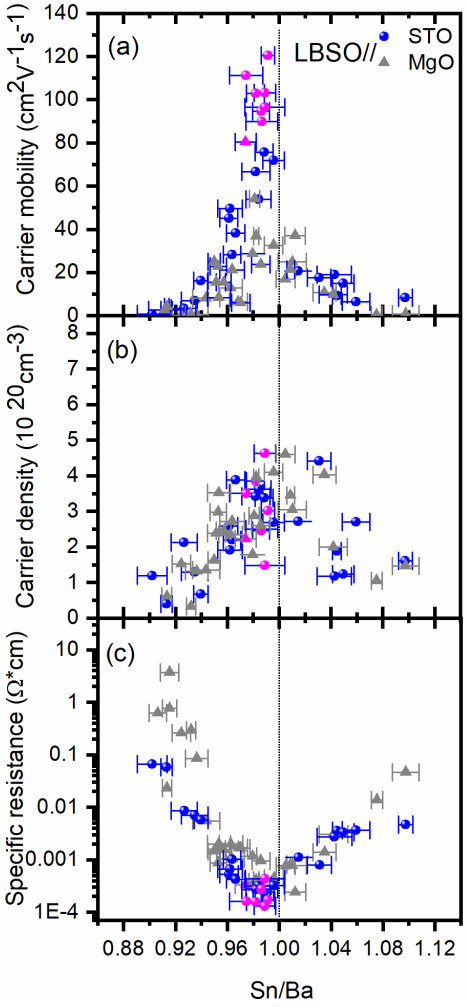

Fig. 25. Room temperature electrical properties of LBSO films deposited on STO and MgO substrates with different Sn/Ba ratio: (a) electron mobility; (b) carrier density n; (c) specific resistance. Pink points mark the highest mobility values of the thin films on both $SrTiO_3$ and MgO substrates.

However, the carrier density demonstrated a rather large distribution with maximum values at Sn/Ba ~ 1. Variation in carrier concentration values is probably a direct result of inaccurate La doping at respective Sn/Ba ratios (Fig. 25 (b)). However, the nature of the change itself is closely related to various other non-stoichiometric defects. Their influence could be based on three competing charge compensation mechanisms in the Sn/Ba-rich compositional zones.

In the Sn-rich growth conditions, it is expected that Ba vacancies ($Ba_{1-3x}La_{2x}V_{Ba.x}O_3$) are formed, creating two holes, which could compensate electrons due to lanthanum doping. Possible defect reaction in the Sn-rich (Ba-deficient) governing electrical behavior are:

$$Ba_{Ba}^{\times} \xrightarrow{La} (1-3x)Ba_{Ba}^{\times} + 2xLa_{Ba}^{\times} + xV_{Ba}^{\times}\ ; \quad (1)$$

Defect ionization:

$$2La_{Ba}^{\times} \rightarrow 2La_{Ba}^{\bullet} + 2e\ ; \quad (2)$$

$$V_{Ba}^{\times} \rightarrow V_{Ba}^{''} + 2h^{\bullet}. \quad (3)$$

Two competing mechanisms might occur in the Ba-rich conditions and sufficiently high oxygen partial pressure ($p(O_2)$ = 2 Torr) by forming Sn

vacancies $Ba_{1-4x}La_{4x}Sn_{1-x}V_{Sn,x}O_3$ (A) or by lanthanum substitution in the Sn site and the formation of oxygen vacancies $BaSn_{1-2x}La_{Sn,2x}O_{3-x}V_{O,x}$ (B). Defect reactions for process A can be written as:

$$Ba_{Ba}^{\times} + Sn_{Sn}^{\times} \xrightarrow{La} (1-4x)Ba_{Ba}^{\times} + 4xLa_{Ba}^{\times} + (1-x)Sn_{Sn}^{\times} + xV_{Sn}^{\times}; \quad (4)$$

Defect ionization:

$$4La_{Ba}^{\times} \rightarrow 4La_{Ba}^{\bullet} + 4e^{'}; \quad (5)$$

$$V_{Sn}^{\times} \rightarrow V_{Sn}^{''''} + 4h^{\bullet}. \quad (6)$$

Defect reactions for process B can be written as:

$$Sn_{Sn}^{\times} \xrightarrow{La} (1-2x)Sn_{Sn}^{\times} + 2xLa_{Sn}^{\times} + xV_{O}^{\times}; \quad (7)$$

Defect ionization:

$$2La_{Sn}^{\times} \rightarrow 2La_{Sn}^{'} + 2h^{\bullet}; \quad (8)$$

$$V_{O}^{\times} \rightarrow V_{O}^{\bullet\bullet} + 2e^{'}. \quad (9)$$

It is important to notice that the oxygen partial pressure can highly influence both A and B mechanisms. Higher $p(O_2)$ lowers oxygen vacancy concentration, and at the same time, by acting on the laws of equilibrium, it promotes all the processes during which oxygen vacancies are formed ($½O_2^{\times} + V_O^{\times} \rightarrow O_O^{\times}$). Therefore, oxygen-rich conditions are more favorable for the process B. Type A compensation mechanism was proposed for the MBE deposited films discussing asymmetric carrier concentration on nonstoichiometry relationships [25]. Although, compared to the MBE method, the partial oxygen pressure in the PI-MOCVD process is higher. It is a likely reason for the carrier concentration's symmetrical character when Sn/Ba ratio is varied. In addition, mechanism B might well agree with the proposed Sn/Ba shift of RP-phase and the formation of La_{Sn} antisite defects.

On the other hand, the highest carrier density did not constitute the highest mobility values. This is demonstrated by pink color markings in Fig. 25 (a-c). Best mobility and lowest specific resistance of 1.3×10^{-4} Ωcm corresponded to the Sn/Ba ratio of 0.98. This ratio represents the smoothest surface morphology films, the highest crystalline order, and possibly the beginning of RP-phase formation composition. This suggests that mobility is mainly determined by stoichiometry-dependent structural factors and the films' structural transition [155]. However, the exact structural processes in the structure remain elusive.

Summarizing all the performed studies, it can be stated that the PI-MOCVD method was successfully optimized and applied for the synthesis of thin layers of SnO_2, $BaSnO_3$, La: $BaSnO_3$ thin films. The dependence of the morphology and microstructure of the La-Ba-Sn-O oxide system layers on the little-studied factor - stoichiometry - were thouroughly investigated. By

optimizing and combining deposition conditions and various crystalline substrates, the achieved high values of carrier mobility are comparable with the ones achieved using physical methods. The obtained results are important for further research on the possible wider application of these materials in various functional oxide electronics.

CONCLUSIONS

1. Four potential tin precursors for LBSO synthesis MOCVD methods were selected from a wide range of metalorganic compounds: PODA, PODB, $Sn(thd)_2$, $Sn(Bu)_2(acac)_2$. Their decomposition kinetic studies by depositing SnO_2 films at different temperatures showed that their thermal stability can be arranged in the following order: PODA > PODB > $Sn(thd)_2$ > $Sn(Bu)_2(acac)_2$.
2. Volatile, thermally stable, and compatible $Sn(thd)_2$, $Ba(thd)_2$*triglyme, and $La(thd)_3$*monoglyme metalorganic precursors were suitable for the synthesis of PI-MOCVD of thin undoped and lanthanum-doped barium stannate layers.
3. For the first time, the PI-MOCVD method was applied to synthesize undoped barium stannate and La-doped barium stannate layers on different substrates. At a deposition temperature of 850 °C, epitaxial layers were grown on $LaAlO_3$ (l00), $SrTiO_3$ (l00), MgO (l00) substrates. Polycrystalline - on Al_2O_3 (0006) substrates.
4. By changing the Sn/Ba ratio in epitaxial layers, three different layer morphologies were identified: 1) rough surface consisting of individual crystallites, in the case of an Sn-rich composition; 2) the morphology of a smooth matrix or channel-like network in the case of a near-stoichiometric composition; 3) smooth surface with pyramidal ({221} orientation) crystals on the surface in the presence of an excess of Ba.
5. It was found that the lattice parameter of BSO and LBSO layers increased significantly with increasing barium content when Sn/Ba < 0.98. Meanwhile, the lattice parameter change in the range of 0.98 <Sn / Ba < 1.10 was insignificant.
6. XRD and TEM studies showed a dual microstructural nature of thin (~ 160 nm) BSO and LBSO layers at Sn/Ba < 1. At the beginning of film growth (~ 70 nm), the layer grows epitaxially and is stressed until ~70 nm. The remaining upper part of the layer is relaxed, characterized by colonial growth and structural defects such as crystallite grain boundaries and dislocations.

7. As the Sn/Ba ratio in the BSO layers changes, so does the UV absorption. Hypsochromic shift of the UV absorption edge and an increase in the optical bandgap (E_g) were observed when the Sn/Ba ratio was reduced. LBSO layers had higher Eg values than undoped BSO layers.
8. It was found that the thickness (160 – 380 nm) of LBSO layers deposited on $SrTiO_3$ substrates did not affect their morphology and microstructure. On the other hand, the composition of the layers (~ 380 nm) (Sn / Ba) was strongly influenced the electrical properties of the layers.
9. The carrier concentration variation of the n-type LBSO films from the Sn/Ba composition was characterized by a broad parabolic-type symmetric dependence. The highest charge carrier concentration values were achieved at Sn/Ba ≈ 1 composition: $n = 3 \div 5 \times 10^{20}$ cm^{-3}. Meanwhile, the layers' morphology had a significant effect on the carrier mobility. The highest mobility values comparable to the mobility values of the MBE-grown layers were determined in the most uniform morphology layers in the narrow Sn/Ba ≈ 0.98 range: $\mu = 120.5 \pm 0.6$ $cm^2V^{-1}s^{-1}$ and $\mu = 84.6 \pm 0.2$ $cm^2V^{-1}s^{-1}$, respectively, on STO and MgO substrates.

REFERENCES

[1] K. Hyung Joon, K. Useong, K. Hoon Min, K. Tai Hoon, M. Hyo Sik, J. Byung-Gu, H. Kwang Taek, L. Woong-Jhae, J. Chanjong, K. Kee Hoon, C. Kookrin, Applied Physics Express, 5 (2012) 061102.
[2] A. Kojima, K. Teshima, Y. Shirai, T. Miyasaka, Journal of the American Chemical Society, 131 (2009) 6050-6051.
[3] M. Liu, M.B. Johnston, H.J. Snaith, Nature, 501 (2013) 395-398.
[4] C.A. Hancock, J.M. Porras-Vazquez, P.J. Keenan, P.R. Slater, Dalton Transactions, 44 (2015) 10559-10569.
[5] F. Ryosuke, Y. Hiroko, O. Shingo, U. Yoshiaki, B. Ausrine, F. Mamoru, N. Yukio, Japanese Journal of Applied Physics, 51 (2012) 09LB01.
[6] C. Jimenez, F. Weiss, J.-P. Senateur, A. Abrutis, M. Krellmann, D. Selbmann, J. Eickemeyer, O. Stadel, G. Wahl, IEEE transactions on applied superconductivity, 11 (2001) 2905-2908.
[7] L.F. Schneemeyer, J.V. Waszczak, S.M. Zahorak, R.B. van Dover, T. Siegrist, Materials Research Bulletin, 22 (1987) 1467-1473.
[8] P. Wagner, G. Wackers, I. Cardinaletti, J. Manca, J. Vanacken, physica status solidi (a), 214 (2017) 1700394.
[9] R.N. Mahato, K. Sethupathi, V. Sankaranarayanan, Journal of Applied Physics, 107 (2010) 09D714.
[10] G.H. Haertling, Journal of the American Ceramic Society, 82 (1999) 797-818.
[11] J. Ryu, A.V. Carazo, K. Uchino, H.-E. Kim, Japanese Journal of Applied Physics, 40 (2001) 4948.
[12] T. Kimura, T. Goto, H. Shintani, K. Ishizaka, T.-h. Arima, Y. Tokura, nature, 426 (2003) 55-58.
[13] C.-W. Nan, M. Bichurin, S. Dong, D. Viehland, G. Srinivasan, Journal of applied physics, 103 (2008) 1.
[14] J. Wang, J. Neaton, H. Zheng, V. Nagarajan, S. Ogale, B. Liu, D. Viehland, V. Vaithyanathan, D. Schlom, U. Waghmare, science, 299 (2003) 1719-1722.
[15] S. Mathews, R. Ramesh, T. Venkatesan, J. Benedetto, Science, 276 (1997) 238-240.
[16] A. Ohtomo, H. Hwang, Applied physics letters, 84 (2004) 1716-1718.
[17] B. Himmetoglu, A. Janotti, H. Peelaers, A. Alkauskas, C.G. Van de Walle, Physical Review B, 90 (2014) 241204.
[18] H.-h. Wang, D.-f. Cui, S.-y. Dai, H.-b. Lu, Y.-l. Zhou, Z.-h. Chen, G.-z. Yang, Journal of Applied Physics, 90 (2001) 4664-4667.
[19] J. Son, P. Moetakef, B. Jalan, O. Bierwagen, N.J. Wright, R. Engel-Herbert, S. Stemmer, Nature Materials, 9 (2010) 482.
[20] S. Wemple, Physical Review, 137 (1965) A1575.
[21] M. Wu, S. Yu, L. He, L. Yang, W. Zhang, Scientific Reports, 7 (2017) 103.

[22] H. Yun, K. Ganguly, W. Postiglione, B. Jalan, C. Leighton, K.A. Mkhoyan, J.S. Jeong, Scientific Reports, 8 (2018) 10245.
[23] J. Shiogai, K. Nishihara, K. Sato, A. Tsukazaki, AIP Advances, 6 (2016) 065305.
[24] S. Raghavan, T. Schumann, H. Kim, J.Y. Zhang, T.A. Cain, S. Stemmer, APL Materials, 4 (2016) 016106.
[25] A. Prakash, P. Xu, X. Wu, G. Haugstad, X. Wang, B. Jalan, Journal of Materials Chemistry C, 5 (2017) 5730-5736.
[26] H. Paik, Z. Chen, E. Lochocki, A.S. H., A. Verma, N. Tanen, J. Park, M. Uchida, S. Shang, B.-C. Zhou, M. Brützam, R. Uecker, Z.-K. Liu, D. Jena, K.M. Shen, D.A. Muller, D.G. Schlom, APL Materials, 5 (2017) 116107.
[27] U. Kim, C. Park, T. Ha, R. Kim, H.S. Mun, H.M. Kim, H.J. Kim, T.H. Kim, N. Kim, J. Yu, K.H. Kim, J.H. Kim, K. Char, APL Materials, 2 (2014) 056107.
[28] L. Weston, L. Bjaalie, K. Krishnaswamy, C.G. Van de Walle, Physical Review B, 97 (2018) 054112.
[29] R.F.M. C. J. Harbert, US Patent 2,356,317, (1944).
[30] E. Wainer, US Patent 2399082, URL: https://www.google.com/patents/US2399082,, (1946).
[31] E. Wainer, US Patent 2402515, URL: https://www.google.com/patents/US2402515, , (1946).
[32] E. Wainer, US Patent 2402518., URL https://www.google.com/patents/US2402518. (1946).
[33] R. Dungan, D. Kane, L. Bickford Jr, Journal of the American Ceramic Society, 35 (1952) 318-321.
[34] S.L. Swartz, IEEE Transactions on Electrical Insulation, 25 (1990) 935-987.
[35] G. Smolensky, V. Isupov, Zh. Tekh. Fiz, 24 (1954) 1375.
[36] S. Nomura, Journal of the Physical Society of Japan, 10 (1955) 112-119.
[37] T. Wang, X. Chen, X. Zheng, Journal of Electroceramics, 11 (2003) 173-178.
[38] J. Donohue, S.J. Miller, R.F. Cline, Acta Crystallographica, 11 (1958) 693-695.
[39] V. Mueller, H. Beige, H.-P. Abicht, Applied Physics Letters, 84 (2004) 1341-1343.
[40] V. Mueller, L. Jäger, H. Beige, H.-P. Abicht, T. Müller, Solid state communications, 129 (2004) 757-760.
[41] R. Vivekanandan, T. Kutty, Materials Science and Engineering: B, 6 (1990) 221-231.
[42] R. Steinhausen, A. Kouvatov, H. Beige, H. Langhammer, H.-P. Abicht, Journal of the European Ceramic Society, 24 (2004) 1677-1680.
[43] Z. Zhi-Gang, Z. Gang, W. Ming, Z. Zhong-Tai, Sensors and Actuators, 19 (1989) 71-81.
[44] R.A. Bucur, A.I. Bucur, S. Novaconi, I. Nicoara, Journal of alloys and compounds, 542 (2012) 142-146.

[45] O. Prokopalo, Ferroelectrics, 14 (1976) 683-685.
[46] B. Ostrick, M. Fleischer, H. Meixner, Journal of the American Ceramic Society, 80 (1997) 2153-2156.
[47] B. Ostrick, M. Fleischer, U. Lampe, H. Meixner, Sensors and Actuators B: Chemical, 44 (1997) 601-606.
[48] J. Cerdà, J. Arbiol, G. Dezanneau, R. Díaz, J.R. Morante, Sensors and Actuators B: Chemical, 84 (2002) 21-25.
[49] U. Lampe, J. Gerblinger, H. Meixner, Sensors and Actuators B: Chemical, 25 (1995) 657-660.
[50] S. Manorama, C.G. Reddy, V. Rao, Applied surface science, 174 (2001) 93-105.
[51] M. Aguas, L. Morris, I. Parkin, Journal of materials science, 37 (2002) 375-379.
[52] C.V.G. Reddy, S.V. Manorama, V.J. Rao, A. Lobo, S.K. Kulkarni, Thin Solid Films, 348 (1999) 261-265.
[53] X. Chu, Materials Science and Engineering: B, 106 (2004) 305-307.
[54] S. Manorama, V. Rao, Journal of Materials Science: Materials in Electronics, 12 (2001) 137-142.
[55] S. Tao, F. Gao, X. Liu, O.T. Sørensen, Sensors and Actuators B: Chemical, 71 (2000) 223-227.
[56] J.-M. Herrmann, M.R. Nunes, F.M. da Costa, Journal of the Chemical Society, Faraday Transactions 1: Physical Chemistry in Condensed Phases, 78 (1982) 1983-1991.
[57] G. Larramona, C. Gutiérrez, I. Pereira, M.R. Nunes, F.M.A. da Costa, Journal of the Chemical Society, Faraday Transactions 1: Physical Chemistry in Condensed Phases, 85 (1989) 907-916.
[58] R. Cava, B. Batlogg, R. van Dover, P. Gammel, J. Krajewski, W. Peck Jr, L. Rupp Jr, Looking for new high-T c superconductors, in: AIP Conference Proceedings, American Institute of Physics, 1991, pp. 55-64.
[59] D. Singh, D. Papaconstantopoulos, J. Julien, F. Cyrot-Lackmann, Physical Review B, 44 (1991) 9519.
[60] R. Claessen, M.G. Smith, J.B. Goodenough, J.W. Allen, Physical Review B, 47 (1993) 1788-1793.
[61] H. Mizoguchi, P. Chen, P. Boolchand, V. Ksenofontov, C. Felser, P.W. Barnes, P.M. Woodward, Chemistry of Materials, 25 (2013) 3858-3866.
[62] A. Kumar, R.N.P. Choudhary, B.P. Singh, A.K. Thakur, Ceramics International, 32 (2006) 73-83.
[63] B. Ramdas, R. Vijayaraghavan, Bulletin of Materials Science, 33 (2010) 75-78.
[64] O. Parkash, D. Kumar, K. Srivastav, R. Dwivedi, Journal of materials science, 36 (2001) 5805-5810.
[65] M. Yasukawa, Y. Hamada, T. Kono, K. Ueda, H. Yanagi, S.W. Kim, H. Hosono, Journal of the Japan Society of Powder and Powder Metallurgy, 58 (2011) 149-154.

[66] S. Upadhyay, O. Parkash, D. Kumar, Materials Letters, 49 (2001) 251-255.
[67] K. Balamurugan, N.H. Kumar, J.A. Chelvane, P. Santhosh, Journal of alloys and compounds, 472 (2009) 9-12.
[68] K. Balamurugan, E. Senthil Kumar, B. Ramachandran, S. Venkatesh, N. Harish Kumar, M.S. Ramachandra Rao, P.N. Santhosh, Journal of Applied Physics, 111 (2012) 074107.
[69] R. Köferstein, F. Yakuphanoglu, Journal of alloys and compounds, 506 (2010) 678-682.
[70] K. Balamurugan, N.H. Kumar, B. Ramachandran, M.R. Rao, J.A. Chelvane, P. Santhosh, Solid state communications, 149 (2009) 884-887.
[71] -.Z. Peng, -.L. Qin-Zhuang, -.S. Fu-Hai, -.L. Qiang-Chun, -.L. Zhe, -.S. Wen-Hai, -.D. Jian-Ming, - Acta Physica Sinica, - 62 (2013) - 027101.
[72] P. Singh, C.P. Sebastian, D. Kumar, O. Parkash, Journal of alloys and compounds, 437 (2007) 34-38.
[73] A. Kumar, B. Singh, R. Choudhary, A.K. Thakur, Materials chemistry and physics, 99 (2006) 150-159.
[74] Y. Hinatsu, K. Tezuka, Journal of Solid State Chemistry, 138 (1998) 329-333.
[75] A. Kumar, R. Choudhary, Journal of materials science, 42 (2007) 2476-2485.
[76] A. Kumar, B. Singh, R. Choudhary, A.K. Thakur, Materials Letters, 59 (2005) 1880-1888.
[77] Y.Z. Wang, E. Bevillon, A. Chesnaud, G. Geneste, G. Dezanneau, The Journal of Physical Chemistry C, 113 (2009) 20486-20492.
[78] É. Bévillon, G. Geneste, Physical Review B, 77 (2008) 184113.
[79] M. Trari, J.-P. Doumerc, P. Dordor, M. Pouchard, G. Behr, G. Krabbes, Journal of Physics and Chemistry of Solids, 55 (1994) 1239-1243.
[80] K. Hyung Joon, K. Useong, K. Hoon Min, K. Tai Hoon, M. Hyo Sik, J. Byung-Gu, H. Kwang Taek, L. Woong-Jhae, J. Chanjong, K. Kee Hoon, C. Kookrin, Applied Physics Express, 5 (2012) 061102.
[81] S. Ismail-Beigi, F.J. Walker, S.-W. Cheong, K.M. Rabe, C.H. Ahn, APL Materials, 3 (2015) 062510.
[82] J. Henriques, E. Caetano, V. Freire, J. Da Costa, E. Albuquerque, Journal of Physics: Condensed Matter, 19 (2007) 106214.
[83] W. Zhang, J. Tang, J. Ye, Chemical physics letters, 418 (2006) 174-178.
[84] T. Maekawa, K. Kurosaki, S. Yamanaka, Journal of alloys and compounds, 416 (2006) 214-217.
[85] B.G. Kim, J. Jo, S.-W. Cheong, Journal of Solid State Chemistry, 197 (2013) 134-138.
[86] R.D. Shannon, Acta Crystallographica Section A, 32 (1976) 751-767.
[87] Kumar Upendra, Ansaree Jawed, Upadhyay Shail, Processing and Application of Ceramics, 11 (2017) 177 - 184.

[88] W.J. Lee, H.J. Kim, E. Sohn, T.H. Kim, J.Y. Park, W. Park, H. Jeong, T. Lee, J.H. Kim, K.Y. Choi, K.H. Kim, Applied Physics Letters, 108 (2016) 082105.
[89] E. Moreira, J.M. Henriques, D.L. Azevedo, E.W.S. Caetano, V.N. Freire, U.L. Fulco, E.L. Albuquerque, Journal of Applied Physics, 112 (2012) 043703.
[90] B. Monserrat, C.E. Dreyer, K.M. Rabe, Physical Review B, 97 (2018) 104310.
[91] D.O. Scanlon, Physical Review B, 87 (2013) 161201.
[92] S. Lany, A. Zunger, Physical Review B, 78 (2008) 235104.
[93] A. Janotti, C.G.V.d. Walle, Applied Physics Letters, 87 (2005) 122102.
[94] F. Oba, A. Togo, I. Tanaka, J. Paier, G. Kresse, Physical Review B, 77 (2008) 245202.
[95] S. Lany, A. Zunger, Physical Review B, 81 (2010) 205209.
[96] A.K. Singh, A. Janotti, M. Scheffler, C.G. Van de Walle, Physical Review Letters, 101 (2008) 055502.
[97] J.B. Varley, J.R. Weber, A. Janotti, C.G. Van de Walle, Applied Physics Letters, 97 (2010) 142106.
[98] P. Ágoston, K. Albe, R.M. Nieminen, M.J. Puska, Physical review letters, 103 (2009) 245501.
[99] S. Limpijumnong, P. Reunchan, A. Janotti, C.G. Van de Walle, Physical Review B, 80 (2009) 193202.
[100] H. Peng, J.-H. Song, E.M. Hopper, Q. Zhu, T.O. Mason, A.J. Freeman, Chemistry of Materials, 24 (2012) 106-114.
[101] M. Burbano, D.O. Scanlon, G.W. Watson, Journal of the American Chemical Society, 133 (2011) 15065-15072.
[102] M.A. Green, K. Prassides, P. Day, J.K. Stalick, Journal of the Chemical Society, Faraday Transactions, 92 (1996) 2155-2159.
[103] D.A. Muller, N. Nakagawa, A. Ohtomo, J.L. Grazul, H.Y. Hwang, Nature, 430 (2004) 657-661.
[104] Y. Li, L. Zhang, Y. Ma, D.J. Singh, APL Materials, 3 (2015) 011102.
[105] Y. Tang, Y. Zhu, Y. Zhang, Z. Zhang, X. Ma, Journal of Materials Research, 28 (2013) 1692.
[106] T. Suzuki, Y. Nishi, M. Fujimoto, Journal of the American Ceramic Society, 83 (2000) 3185-3195.
[107] C. Lu, L. Bendersky, K. Chang, I. Takeuchi, Philosophical Magazine, 83 (2003) 1565-1595.
[108] W.Y. Wang, Y.L. Tang, Y.L. Zhu, J. Suriyaprakash, Y.B. Xu, Y. Liu, B. Gao, S.W. Cheong, X.L. Ma, Scientific Reports, 5 (2015) 16097.
[109] H. Mun, U. Kim, H.M. Kim, C. Park, T.H. Kim, H.J. Kim, K.H. Kim, K. Char, Applied Physics Letters, 102 (2013) 252105.
[110] K. Young Mo, P. Chulkwon, K. Useong, J. Chanjong, C. Kookrin, Applied Physics Express, 9 (2016) 011201.
[111] J. Park, U. Kim, K. Char, C.R. J., B. B., K.J. J., F. R., R.L. W., W.A. E., S. K., P.W. F., K. T., Applied Physics Letters, 108 (2016) 092106.

[112] A. Prakash, P. Xu, A. Faghaninia, S. Shukla, J.W. Ager Iii, C.S. Lo, B. Jalan, Nature Communications, 8 (2017) 15167.
[113] D. Phelan, F. Han, A. Lopez-Bezanilla, M.J. Krogstad, Y. Gim, Y. Rong, J. Zhang, D. Parshall, H. Zheng, S.L. Cooper, M. Feygenson, W. Yang, Y.-S. Chen, Journal of Solid State Chemistry, 262 (2018) 142-148.
[114] S.S. Shin, E.J. Yeom, W.S. Yang, S. Hur, M.G. Kim, J. Im, J. Seo, J.H. Noh, S.I. Seok, Science, 356 (2017) 167-171.
[115] S.S. Shin, E.J. Yeom, W.S. Yang, S. Hur, M.G. Kim, J. Im, J. Seo, J.H. Noh, S.I. Seok, Science, 356 (2017) 167-171.
[116] B.B.N. Anchal, P. Singh, R. Pyare, Materials Today: Proceedings, 18 (2019) 1310-1316.
[117] A.A. Kumar, J. Singh, D.S. Rajput, A. Placke, A. Kumar, J. Kumar, Materials Science in Semiconductor Processing, 83 (2018) 83-88.
[118] K. Hu, S. Wang, M. Zhang, F. Huang, X. Kong, Q. Liu, Journal of Materials Science: Materials in Electronics, 30 (2019) 15420-15428.
[119] H.J. Kim, U. Kim, T.H. Kim, J. Kim, H.M. Kim, B.-G. Jeon, W.-J. Lee, H.S. Mun, K.T. Hong, J. Yu, K. Char, K.H. Kim, Physical Review B, 86 (2012) 165205.
[120] X. Luo, Y.S. Oh, A. Sirenko, P. Gao, T. Tyson, K. Char, S.-W. Cheong, Applied Physics Letters, 100 (2012) 172112.
[121] H.J. Cho, T. Onozato, M. Wei, A. Sanchela, H. Ohta, APL Materials, 7 (2019) 022507.
[122] M. wu, S. Yu, L. He, L. Yang, W. Zhang, The Role of Annealing Process in Ag-Based BaSnO3 Multilayer Thin Films, 2016.
[123] S. Yu, D. Yoon, J. Son, Applied Physics Letters, 108 (2016) 262101.
[124] H.J. Kim, J. Kim, T.H. Kim, W.-J. Lee, B.-G. Jeon, J.-Y. Park, W.S. Choi, S.H. Lee, J. Yu, T.W. Noh, Physical Review B, 88 (2013) 125204.
[125] Z. Galazka, R. Uecker, K. Irmscher, D. Klimm, R. Bertram, A. Kwasniewski, M. Naumann, R. Schewski, M. Pietsch, U. Juda, Journal of Physics: Condensed Matter, 29 (2016) 075701.
[126] H. Wang, Q. Liu, F. Chen, G. Gao, W. Wu, X. Chen, Transparent and conductive oxide films with the perovskite structure: La-and Sb-doped Ba Sn O 3, in, American Institute of Physics, 2007.
[127] Q. Liu, J. Liu, B. Li, H. Li, G. Zhu, K. Dai, Z. Liu, P. Zhang, J. Dai, Applied Physics Letters, 101 (2012) 241901.
[128] U. Kim, C. Park, T. Ha, Y.M. Kim, N. Kim, C. Ju, J. Park, J. Yu, J.H. Kim, K. Char, APL Materials, 3 (2015) 036101.
[129] M. White, M. Tsai, F. Wu, J. Speck, Journal of Vacuum Science & Technology A: Vacuum, Surfaces, and Films, 26 (2008) 1300-1307.
[130] T. Nakajima, T. Tsuchiya, T. Kumagai, Japanese journal of applied physics, 46 (2007) L365.
[131] T. Watahiki, W. Braun, H. Riechert, Journal of Vacuum Science & Technology B: Microelectronics and Nanometer Structures Processing, Measurement, and Phenomena, 27 (2009) 262-265.

[132] K. Sasaki, A. Kuramata, T. Masui, E.G. Víllora, K. Shimamura, S. Yamakoshi, Applied Physics Express, 5 (2012) 035502.
[133] R. Lamoreaux, D. Hildenbrand, L. Brewer, Journal of physical and chemical reference data, 16 (1987) 419-443.
[134] S.K. M. Veith, Journal of Material Science Letters, 13 (1994) 335-337.
[135] H.A. Meinema, K. Timmer, H.L. Linden, C.I. Spee, MRS Online Proceedings Library Archive, 335 (1993).
[136] G. Kunte, S. Shivashankar, A. Umarji, Measurement Science and Technology, 19 (2008) 025704.
[137] A. Abrutis, G. Valincius, G. Baltrunas, L. Parafionovic, A. Valiuniene, Z. Saltyte, Thin Solid Films, 515 (2007) 6817-6823.
[138] J. Sundqvist, M. Ottosson, A. Hårsta, Chemical Vapor Deposition, 10 (2004) 77-82.
[139] Z. Zhu, J. Ma, C. Luan, L. Kong, Q. Yu, Journal of luminescence, 131 (2011) 88-91.
[140] L. Tien, D.P. Norton, J.D. Budai, Materials Research Bulletin, 44 (2009) 6-10.
[141] A. Bartasyte, V. Plausinaitiene, A. Abrutis, T. Murauskas, P. Boulet, S. Margueron, J. Gleize, S. Robert, V. Kubilius, Z. Saltyte, Applied Physics Letters, 101 (2012) 122902.
[142] J.-P. Senateur, J. Lindner, F. Weiss, C. Dubourdieu, C. Jiménez, A. Abrutis, Application of Pulsed Injection MOCVD to the Deposition of Dielectric and Ferroelectric Oxide Layers and Superlattices, 2011.
[143] S.A. Chambers, T.C. Kaspar, A. Prakash, G. Haugstad, B. Jalan, K.H. J., K. U., K.H. M., K.T. H., M.H. S., J. B.-G., H.K. T., L. W.-J., J. C., K.K. H., C. K., Applied Physics Letters, 108 (2016) 152104.
[144] S.N. Ruddlesden, P. Popper, Acta Crystallographica, 10 (1957) 538-539.
[145] B. Pödör, physica status solidi (b), 16 (1966) K167-K170.
[146] U. Gebhardt, N. Kasper, A. Vigliante, P. Wochner, H. Dosch, F. Razavi, H.U. Habermeier, Formation and Thickness Evolution of Periodic Twin Domains in Manganite Films Grown on SrTiO 3 (001) Substrates, 2007.
[147] C.Z. Chen, C.B. Cai, Z.Y. Liu, L. Peng, B. Gao, F. Fan, Y.M. Lu, R. Zeng, Z.P. Guo, W.X. Li, S.X. Dou, Solid State Communications, 150 (2010) 66-69.
[148] H. Wei, M. Jenderka, M. Grundmann, M. Lorenz, physica status solidi (a), 212 (2015) 1925-1930.
[149] J.B. Varley, J.R. Weber, A. Janotti, C.G.V.d. Walle, Applied Physics Letters, 108 (2016) 039901.
[150] P. Ágoston, C. Körber, A. Klein, M.J. Puska, R.M. Nieminen, K. Albe, Journal of Applied Physics, 108 (2010) 053511.
[151] S. Miyoshi, J.-O. Hong, K. Yashiro, A. Kaimai, Y. Nigara, K. Kawamura, T. Kawada, J. Mizusaki, Solid State Ionics, 161 (2003) 209-217.
[152] R. Lukose, V. Plausinaitiene, M. Vagner, N. Zurauskiene, S. Kersulis, V. Kubilius, K. Motiejuitis, B. Knasiene, V. Stankevic, Z. Saltyte, M. Skapas,

A. Selskis, E. Naujalis, Beilstein Journal of Nanotechnology, 10 (2019) 256-261.
[153] R.U. Chandrasena, W. Yang, Q. Lei, M.U. Delgado-Jaime, K.D. Wijesekara, M. Golalikhani, B.A. Davidson, E. Arenholz, K. Kobayashi, M. Kobata, F.M.F. de Groot, U. Aschauer, N.A. Spaldin, X. Xi, A.X. Gray, Nano Letters, 17 (2017) 794-799.
[154] A.P. Nono Tchiomo, W. Braun, B.P. Doyle, W. Sigle, P. van Aken, J. Mannhart, P. Ngabonziza, APL Materials, 7 (2019) 041119.
[155] A.V. Sanchela, M. Wei, H. Zensyo, B. Feng, J. Lee, G. Kim, H. Jeen, Y. Ikuhara, H. Ohta, Applied Physics Letters, 112 (2018) 232102.
[156] H.J. Kim, U. Kim, T.H. Kim, J. Kim, H.M. Kim, B.-G. Jeon, W.-J. Lee, H.S. Mun, K.T. Hong, J. Yu, Physical Review B, 86 (2012) 165205.
[157] Z. Lebens-Higgins, D. Scanlon, H. Paik, S. Sallis, Y. Nie, M. Uchida, N. Quackenbush, M. Wahila, G. Sterbinsky, D.A. Arena, Physical Review Letters, 116 (2016) 027602.
[158] T. Murauskas, V. Kubilius, Z. Saltyte, V. Plausinaitiene, Thin Solid Films, 692 (2019) 137575.
[159] L. Qinzhuang, L. Bing, L. Jianjun, L. Hong, L. Zhongliang, D. Kai, Z. Guangping, Z. Peng, C. Feng, D. Jianming, EPL (Europhysics Letters), 98 (2012) 47010.
[160] D. Fuchs, M. Adam, P. Schweiss, S. Gerhold, S. Schuppler, R. Schneider, B. Obst, Journal of Applied Physics, 88 (2000) 1844-1850.

CURRICULUM VITAE

PERSONAL INFORMATION		
Name, Surname	Tomas Murauskas	
Date of birth	1991-09-05	
Address	Eišiškių pl. 26-28, Vilnius	
Phone number	+370 60837502	
E-mail	tomas.murauskas@chf.vu.lt	
ACADEMIC EDUCATION		
2010 – 2014	Bachelor of Science in Chemistry, Vilnius University	
2014 – 2016	Master of Science in Chemistry, Vilnius University	
ACADEMIC/SCIENTIFIC AFFILIATIONS		
2011-09 – 2015-09	Department of General and Inorganic Chemistry, Vilnius University	Laboratory assistant
2015-06 – 2016-03	Department of General and Inorganic Chemistry, Vilnius University	Senior specialist
2016-03 – 2020-01	National public health surveillance laboratory (NPHSL)	Head of Instrumental research department
2020-01 – iki dabar	Institute of Chemistry, Vilnius University	Junior researcher
TRAINING SCHOOLS		
2016-10-17 – 2016-10-21	Training of general competencies of young researchers	
2019-05-27 – 2019-05-31	Conference –school “The 2019 Spring Meeting of the European Materials Research Society (E-MRS)”, Nice, France	
2020-08-24 – 2020-08-28	22nd international school Advanced materials and technologies, Palanga, Lietuva	
ADDITIONAL ACTIVITIES		
2016-03 – 2020-01	NPHSL Horison2020 Joint actions project coordinator, a representative in the European Commission	

SANTRAUKA

ĮVADAS

Ši disertacija yra dedikuota perovskito tipo lantanu legiruotam bario stanatui La:$BaSnO_3$ (LBSO) ir jo sintezės PI-MOCVD būdu išvystimui. Medžiagos, turinčios perovskito tipo struktūrą, pasižymi įvairiomis fizinėmis savybėmis – fotoelektriniu efektu [2, 3], superlaidumu [4-7], magnetovarža [8, 9], feroelektriniu efektu [10, 11] ir multiferoizmu [12, 13]. Siekiant panaudoti tokias įvairiapuses fizines savybes atlikti plataus masto tyrimai plonų plėvelių ir jų heterostruktūrų srityje [14, 15]. Perovskito tipo oksidinės medžiagos buvo ypač tiriamos šviesai skaidrių ir elektrai laidžių medžiagų srityje. Plačiausiai ištirti perovskitiniai oksidai yra legiruoti $SrTiO_3$ ir $KTaO_3$, kurių elektronų judrio μ vertės esant ∼2 K siekė 32667 $cm^2V^{-1}s^{-1}$ ir 23000 $cm^2V^{-1}s^{-1}$ [16-20], tačiau kambario temperatūroje šie perovskitiniai oksidai pasižymėjo labai mažu judriu (1 – 30 $cm^2V^{-1}s^{-1}$). Tai stipriai apribojo jų pritaikymo galimybes. Kita vertus, 2012 metais didelis judris (320 $cm^2V^{-1}s^{-1}$) buvo atrastas LBSO kristale [1]. Tokios judrio vertės buvo palyginamos su III-grupės nitridų puslaidininkiais. Tai sukėlė naują susidomėjimo bangą oksidinėje elektronikoje. Taip pat dėl LBSO ir kitų medžiagų suderinamumo, atvėrė duris naujoviškam įvairių perovskitinių medžiagų pritaikymui įvairiose srityse.

Legiruoto bario stanato kristalų elektrinės savybės yra labai perspektyvios. Tačiau įvairiuose prietaisuose reikalingų plonų sluoksnių, didelis judris kambario temperatūroje išlieka iššūkiu. Iki šiol nusodinti ploni sluoksniai pasižymėjo kur kas mažesniu elektronų judriu. Nelegiruoto bario stanato (BSO) ir legiruoto BSO plėvelės buvo nusodintos naudojant magnetroninio dulkinimo [21, 22], impulsinio lazerinio nusodinimo (PLD) [23] ir molekulinės pluošto epitaksijos (MBE) metodais [24, 25]. Paik ir bendraautorių susintetintų plonų LBSO sluoksnių ant $DyScO_3$ padėklų judrio vertės siekė net 183 $cm^2V^{-1}s^{-1}$ [26]. Gerus rezultatus - 150 $cm^2V^{-1}s^{-1}$ ir 100 $cm^2V^{-1}s^{-1}$ – taip pat pasiekė Raghavan su bendraautoriais naudodami $PrScO_3$ ir $SrTiO_3$ padėklus. Sumažėjęs judris LBSO sluoksniuose pirmiausia buvo siejamas su substrato sukeltomis nesutapimo/sraigtinėmis dislokacijomis [27], veikiančiomis kaip krūvininkų sklaidos centrai kristalitų sandūros ribose. Blogesnėmis elektrinėmis savybėmis LBSO plėvelės taip pat pasižymėjo dėl taškinių defektų, susidariusių nukrypstant nuo stechiometrijos (Sn / (Ba + La) = 1).

Nestechiometrija lėmė reikšmingą n-tipo krūvininkų koncentracijos ir judrio sumažėjimą dėl susidariusių taškinių defektų krūvio konpensavimo

[28]. Krūvį kuriantys La_{Ba} donorai yra kompensuojami akceptorinio tipo Ba ir Sn vanacijomis arba pakeistiniais La_{Sn} defektais. Būtent galimybė tiksliai valdyti sluoksnių sudėtį ir, tuo pačiu, susidarančių taškinių bei struktūrinių defektų koncentracijas potencialiai leistų nusodinti didelio judrio LBSO sluoksnius MOCVD būdu. La_{Sn} defektų neigiama įtaka teoriškai galėtų būti sumažinta didelio kationų pertekliaus ir deguonies trūkumo sąlygomis remiantis Weston et al. teoriniais skaičiaviais [28]. Be to, kontroliuojant veiksnius, tokius kaip padėklo struktūra, sluoksnių mikrostruktūra ir stechiometrija, būtų pasiektos geresnės elektrinės savybės. Gerai optimizuotomis nusodinimo sąlygomis puikūs rezultatai buvo pasiekti PLD ir MBE metodais. Kita vertus, rezultatų atkartojamumas buvo gana prastas. Sluoksniai nusodinti tais pačiais metodais ir sąlygomis pasižymėjo dideliais elektrinių savybių skirtumais, ypatingai skirtingomis judrio vertėmis. Tai galėjo būti susiję su stechiometrijos valdymo sunkumais minėtuose fizikiniuose metoduose. Naudojant MBE ir PLD metodus pateikta labai mažai informacijos apie sluoksnių sudėtis ir jos lemiamas savybes.

Šios disertacijos tikslas – pritaikyti PI-MOCVD metodą plonų bario stannato sluoksnių nusodinimui ir ištirti plonų plėvelių savybes bei nusodinimo sąlygų įtaką struktūrinėms ir elektrinėms savybėms. Šioje disertacijoje didelis dėmesys skiriamas plonų LBSO sluoksnių išsamiam MOCVD sintezės metodo optimizavimui ir su stechiometrija susijusių savybių tyrimui. Disertacijos darbas pradedamas nuo alavo, bario bei lantano metalorganinių pirmtakų parinkimo ir jų termogravimetrinės analizės. Alavo pirmtakai išbandomi, nusodinant plonus alavo oksido sluoksnius įvairiomis sąlygomis. Šių sluoksnių mikrostruktūra ir skilimo proceso kinetika aprašoma temperatūrų intervale nuo 400 °C iki 900 °C. Sluoksiai charakterizuoti Rentgeno spinduliu difracinės analizės metodais, atominės jėgos mikroskopija bei skenuojančia elektronine mikroskopija.

Atrinkus tinkamus $Sn(thd)_2$, $Ba(thd)_2$*triglimas bei $La(thd)_3$*monoglimas pirmtakus, atliktas plonų (~160 nm) nelegirtuotų ir lantanu legiruotų bario stanato sluoksnių nusodinimas. Pagrindinės nusodinimo sąlygos lemiančios struktūrines, optines bei elektrines savybes aptariamos tolesniuose disertacijos skyriuose. Didėjančio gardelės parametro įtaka tiriama naudojant vis didesnio gardelės parametro padėklus $LaAlO_3$ (*l*00), $SrTiO_3$ (*l*00), ir Al_2O_3 (0006).

Paskutinėje didertacijos rezultatų dalyje aptariami optimizuoto nusodinimo proceso rezultatai nusodinant jau storesnius (~380 nm) plonus sluoksnius. Šiam darbui panaudojami $SrTiO_3$ (*l*00) ir MgO(*l*00) padėklai. Aprašomi detalūs plonų sluoksnių morfologijos mikrostruktūros ir elektrinių savybių sąryšiai su sluoksnių stechiometrija gerokai siauresniame sudėties

intervale. Aptariami galimi kompensacijos mechanizmai ir stebimi struktūriniai pokyčiai. Aprašoma be galo svarbi stechiometrijos rolė elektrinėms ir struktūrinėms sluoksnių savybėms.

Disertacijos darbui atlikti suformuluoti šie uždaviniai:

1. Atrinkti ir palyginti tinkamus metaloorganinius pirmtakus plonų LBSO sluoksnių nusodinimui iš cheminės metaloorganinių garų fazės (MOCVD) būdu.
2. Ištirti ir aprašyti bei palyginti plonų alavo oksidų sluoksnių savybes bei nusodinimo proceso kinetiką naudojant komercinius, sintetintus, bei naujos struktūros alavo pirmtakus.
3. Sukurti ir optimizuoti tinkamas nusodinimo sąlygas ploniems bario stanato sluoksniams optimizuojant esminius nusodinimo parametrus: temperatūrą, padėklo struktūrą, Sn/Ba santykį.
4. Pasiekti n-tipo elektrinį laidumą lantanu legiruotuose plonuose bario stanato sluoksniuose ir ištirti elektrines savybes naudojant Van der Pauw keturių kontaktų metodą bei Hall'o matavimus.
5. Ištirti Sn/Ba nestechiometrijos įtaką plonų LBSO sluoksnių mikrostruktūrai, morfologijai ir elektrinėms savybėms.
6. Pasiekti dideles judrio vertes palyginamas su fizikiniais metodais nusodinamų sluoksnių judrio vertėmis.

EKSPERIMENTO METODIKA

Visi sluoksniai šiame darbe buvo sintetinami impulsinio-injekcinio metaloorganinių garų nusodinimo iš cheminės garų fazės (PI-MOCVD) metodu. Šiame metode metaloorganinių medžiagų tirpalai injektuojami į vakuumo zoną, kurioje yra išgarinami. Garai, dujų srautais, nešami į reakcijos zoną, skyla prie padėklo paviršiaus ir suformuoja atitinkamą oksidinį sluoksnį valdomos temperatūros bei dujinės aplinkos zonoje.

Atlikus plačias pirmtakų paieškas ir įvertinus jų tinkamumą pagrindiniais metaloorganiniai pirmtakais šiame darbe buvo panaudoti $Sn(thd)_2$, $Ba(thd)_2$*triglimas bei $La(thd)_3$*monoglimas. Šios medžiagos buvo tirpinamos grynintame dimetoksietane. Pradžioje buvo ruošiamas tik vienas tirpalas. Vėlesnėje darbo eigoje alavo pirmtakas atskirtas nuo bario ir lantano kitame tirpale. Nusodinimui buvo parinkti $SrTiO_3$ (*l*00), $LaAlO_3$ (*l*00), Al_2O_3 (0006) bei MgO (*l*00) kristaliniai padėklai. Plonų sluoksnių nusodinimui naudotos 1 lentelėje pateikiamos sintezių sąlygos.

1 lentelė. SnO_2, BSO/LBSO, LBSO sluoksnių nusodinimo sąlygos injekcinio impulsinio metaloorganinių garų nusodinimo iš cheminės fazės būdu sąlygos.

Medžiaga	Tirpiklis	Tirp. tūris, (ml)	Konc., (M)	Garintuvo T, (°C)	Padėklo T, (°C)	$Ar+O_2$ slėgis, (Torr)	O_2 dalinis slėgis, (Torr)	Injekcijos dažnis, (Hz)	Injektoriai	Dujų srautas, (ml/min)
SnO_2	DME	10-15	0,01	200	400-900	10	2	2	1	1000
BSO LBSO	DME	10-15	0,01	200	800-900	10	2	2	1	1000
LBSO	DME	40	0,019	200	850	10	1	2	2	1200

Prieš atliekant sluoksnių sintezę, kiekvienas metaloorganinis pirmtakas buvo tiriamas naudojant termogravimetrinę analizę (TGA). Ji buvo atlikta naudojant STA 6000 (PerkinElmer) prietaisą. Nusodintų sluoksnių Rentgeno spindulių difrakcinė (XRD) analizė atlikta naudojant Rigaku MiniFlex II difraktometrą bei D8 Advance (Bruker) su vario anodu (CuK_α, λ=1,5418 Å). θ-2θ difraktogramos užrašytos Bragg-Brentano geometrijoje. Tekstūros analizė ir polių figūros išmatuotos, naudojant Schultz geometriją ir monochromatizuotą spinduliuotę. Slystančio kampo Rentgeno matavimai atlikti naudojant 0,45 ° kritimo kampą.

Sluoksnių morfologija buvo tiriama skenuojančiu elektroniniu mikroskopu (SEM) Hitachi SU70. Elementinė analizė buvo atliekama SEM su Rentgeno spindulių energijos dispersijos spektrometru (EDX). Vidinė sluoksnių struktūra ir padėklo/sluoksnio sandūra tirta naudojant peršviečiamąjį elektroninį mikroskopą Tecnai G2 F20 X-TWIN (Fei) (TEM). Paviršiaus lygumas įvertintas naudojant Nanoscope III (Veeco) atominės jėgos mikroskopą (AFM). Sluoksnių storis ir optinės savybės tirtos kintamo kampo spektroskopinės elipsometrijos (M-2000, J. A. Wollam) ir UV-regimosios spektroskopijos (Lambda 35, Perkin Elmer) pagalba.

REZULTATAI IR JŲ APTARIMAS

Metaloorganinių kompleksų parinkimas ir jų kokybės tyrimai

Didelę įtaką sėkmingam MOCVD technologijų pritaikymui daugiakomponenčių oksidų sluoksnių sintezei turi MO pirmtakų parinkimas. Daugiakomponenčių oksidų sluoksnių atveju, metaloorganinių (MO) kompleksų garų skilimo greičiai bei terminiai stabilumai yra skirtingi. Nuo jų suderinamumo priklauso garų fazės, o tuo pačiu ir sluoksnio sudėtis. Pagrindiniai MO junginių kriterijai yra: lakumas, terminis stabilumas bei suderinamumas tarpusavyje tirpale. Lakumui bei terminiam patvarumui įvertinti buvo naudojamas TGA metodas.

Bario pirmtaku buvo pasirinktas plačiai naudojamas aukštatemperatūrinių superlaidininkų Y-Ba-Cu-O sintezėje [6, 131] β-diketonatų grupės kompleksas: $Ba(thd)_2$*aduktas. Šiuo atveju aduktas (H_2O, triglimas, tetraglimas) prisotina bario koordinacinę sferą ir stabilizuoja molekulę. Kompleksas tampa patvaresnis ilgalaikiam saugojimui, tai lemia geresnį sluoksnių pasikartojamumą. Be to, šis pirmtakas puikiai tirpsta 1,2-dimetoksietane (DME). Susintetintų kompleksų TGA tyrimai parodė (Pav. 13 (a), 38 psl), kad didėjant temperatūrai visų trijų junginių masės netekties procesas susiseda iš dviejų pakopų. Pirmos pakopos atveju atskyla aduktas. Priklausomai nuo pradinės medžiagos – H_2O, triglimo arba tetraglimo molekulė. Šio proceso temperatūriniai intervalai yra atitinkamai: 60 – 127 °C, 95 – 220 °C, 120 – 250 °C. Šioje aduktų eilutėje poslinkis į aukštesnę temperatūrą bei didesnę masės netektį susiję su molekulinės masės ir tuo pačiu su virimo temperatūros didėjimu [136]. Antros pakopos atveju stebimi dvejopi, garavimo bei nežymaus skilimo, procesai. Tokia išvada buvo padaryta remiantis tuo, jog $Ba(thd)_2$*$2H_2O$, $Ba(thd)_2$*triglimas, $Ba(thd)_2$*tetraglimas pirmtakai turi tik nedidelį 15,1 %, 13,2 %, 6,6 % masės likutį. Nors $Ba(thd)_2$*tetraglimo kompleksas garuoja efektyviau, nes turi mažesnį likutį, tolimesniems eksperimentams buvo pasirinktas $Ba(thd)_2$*triglimo pirmtakas. Tokį pasirinkimą nulėmė DME tirpalo stabilumas bei suderinamumas su $Sn(thd)_2$*triglimas pirmtaku (Pav. 13 (b), 38 psl.). Pastarasis kompleksas kartu su $La(thd)_3$*DME (Pav. 13 (c), 38 psl) yra sėkmingai naudojami magnetovaržinių sluoksnių sintezėje PI-MOCVD būdu [152] ir sintetinami VU MOCVD laboratorijoje. Minėtų kompleksų suderinamumas atveria perspektyvas užauginti PI-MOCVD būdu ir legiruotus $BaSnO_3$ sluoksnius, kurie gali būti įdomūs, tiriant didelio judrio prigimtį stanatuose.

Alavo pirmtakų atveju buvo tiriami įvairūs komerciniai ($Sn(OtBu)_4$, $Sn(AcO)_2(Bu)_2$, $Sn(Bu)_2(acac)_2$), partnerių iš Čekijos ($Sn(OtBu)_2(PTFP)_2$ (PODA) bei $Sn(OtBu)_2(OTFP)_2$ (PODB)), bei pačių ($Sn(thd)_2$) sintetinti kompleksai. $Sn(OtBu)_4$, $Sn(AcO)_2(Bu)_2$ junginiai pasižymėjo dideliu jautrumu drėgmei bei orui, bei jų tirpalai buvo itin nestabilūs. Tirpinant $Sn(acac)_2(Bu)_2$ junginį su kitais bario ir lantano pirmtakais, susidarė skaidrūs tirpalai. Tačiau šis kompleksas yra skystas kambario temperatūroje ir apsunkina tirpalų gamybą. Tuo tarpu, PODA, PODB bei $Sn(thd)_2$ yra kietos medžiagos ir patogios naudojimui. Be to, TGA tyrimai parodė (Pav. 13 (b)), kad PODB bei $Sn(thd)_2$ junginiai yra lakūs (jų likutis yra labai nežymus: 5,5 % bei 2,2 %,) ir gali būti naudojami MOCVD procese.

Termogravimetrinės analizės rezultatai yra labai naudingi įvertinant MO pirmtakus. Tačiau TGA tyrimai buvo atlikti aplinkos (760 Torr.) slėgyje. Tuo tarpu PI-MOCVD procese slėgis paprastai yra keičiamas nuo 2 iki 10 Torr. Tokiu atveju pirmtakų garavimo bei terminio patvarumo pobūdis gali keistis. Alavo pirmtakų ($Sn(Bu)_2(acac)_2$, PODA, PODB bei $Sn(thd)_2$) pritaikymo galimybių įvertinimui PI-MOCVD procese buvo atlikti kinetiniai bei morfologijos tyrimai (Pav. 14, 41 psl., Pav. 15 42 psl).

Šiems tyrimams atlikti buvo užauginami SnO_2 sluoksniai, esant įvairioms nusodinimo temperatūroms. Kadangi sluoksnio augimo greičio priklausomybė nuo nusodinimo temperatūros yra Arenijaus tipo, toks tyrimas leido nustatyti ne tik limituojančios stadijos pobūdį, esant tam tikrai temperatūrai, bet ir įvertinti naudotų pirmtakų terminį stabilumą. Cheminių garų nusodinimo iš garų fazės (CVD) procesuose paprastai išskirtos trys sluoksnio augimą limituojančios stadijos: 1) žematemperatūrinė, kai kompleksų cheminė skilimo reakcija vyksta lėtai ir dėl šios priežasties ši stadija jautri temperatūrai; 2) mažai priklausanti nuo temperatūros stadija, kai lėčiausias procesas yra garų difuzija prie padėklo paviršiaus; 3) esant dar aukštesnėms nusodinimo temperatūroms, kai augimo greitis mažėja, nes prasideda komplekso skilimas tūryje.

Iš pateikto grafiko matyti, kad komercinis $Sn(acac)_2(Bu)_2$ pasižymi mažiausiu terminiu stabilumu ir šis pirmtakas yra labiau tinkamas, esant žemoms nusodinimo temperatūroms (Pav. 15, 42 psl.). Auginant $BaSnO_3$ sluoksnius fizikiniais (PLD bei MBE) metodais naudota aukšta ($T \geq 750$ °C) nusodinimo temperatūra. Taigi tikėtina, kad ir MOCVD proceso metu stanatų fazės susidarymas vyks gana aukštoje nusodinimo temperatūroje. Tokiu būdu, tinkamiausia šiam procesui būtų naudoti PODA, PODB arba $Sn(thd)_2$ pirmtakus. Iš šių trijų pirmtakų galiausiai tolimesniems tyrimams buvo pasirinktas $Sn(thd)_2$ kompleksas. Taigi, bario stanatų sluoksnių PI-MOCVD

būdu auginimui bei jų legiravimui buvo pasirinkti $Sn(thd)_2$, $Ba(thd)_2$*triglimas, bei $La(thd)_3$*DME pirmtakai.

Nusodinimo sąlygų įtaka nelegiruotų plonų $BaSnO_3$ sluoksnių savybėms

Pasirinkus MO pirmtakus, kitas žingsnis buvo ištirti PI-MOCVD proceso parametrų įtaką nelegiruotiems bario stanato sluoksnių savybėms. Šiame etape buvo svarbu surasti sąryšius tarp įvairių nusodinimo sąlygų ir sluoksnių fazinės sudėties bei mikrostruktūros. Pirmiausiai, dėmesys buvo skiriamas nusodinimo temperatūrai ir tirpalo sudėčiai. Tai pagrindiniai faktoriai, leidžiantys gauti grynafazius, stechiometrinius sluoksnius. Optimizuojant nusodinimo temperatūrą, BSO sluoksniai buvo auginami skirtingose temperatūrose (800 °C ≤ T_n ≤ 900 °C), naudojant įvairius Sn/Ba molinius santykius tirpale. BSO sluoksniai buvo auginami ant $LaAlO_3$ (*l*00) (LAO), $SrTiO_3$ (*l*00) (STO) bei Al_2O_3 (0006) padėklų. Užaugintų sluoksnių storis buvo 160 – 175 nm.

XRD tyrimai parodė (Pav. 16, 44 psl.), kad užauginti BSO sluoksniai 800 °C temperatūroje yra žemo kristališkumo, net jei jų sudėtis yra artima stechiometrinei sudėčiai (Sn/Ba ~ 1). Tuo tarpu sluoksniai užauginti esant 825 °C temperatūrai jau pasižymėjo aukštos kokybės kristaline struktūra, buvo grynafaziai ir pilnai tekstūruoti (*l*00) kryptimi padėklo atžvilgiu. Šių sluoksnių apskaičiuotos gardelės parametro reikšmės (0,4118 ± 0,0006 nm) buvo labai artimos mokslinėje literatūroje pateiktoms reikšmėms [104].

Nors aukštesnėse nei 825 °C temperatūrose užaugintų BSO sluoksnių difraktogramos buvo panašaus pobūdžio, SEM ir AFM analizė parodė skirtingą šių sluoksnių morfologiją (Pav. 17, 45 psl). Sluoksniams, užaugintiems žemesnėse nei 850 °C temperatūrose, būdingas šiurkštus paviršius su išsikišusiais piramidės formos chaotiškai išsidėsčiusiais kristalitais. Tuo tarpu lygiausios matricos sluoksniai užauginti esant 850 °C temperatūrai. Būtent dėl šios priežasties tolimesniems tyrimams buvo pasirinkta 850 °C nusodinimo temperatūra.

Vis dėlto pagrindinis dėmesys buvo skiriamas siekiant išsiaiškinti nestechiometrijos įtaką tiek nelegiruotų, tiek legiruotų BSO sluoksnių savybėms. Būtent su nestechiometrija susiję eksperimentai yra mažai tyrinėta sritis. Fizikiniai metodai nėra lankstūs tokiems tyrimams, keičiant nusodinimo sąlygas sluoksniuose pasiekiamas tik nedidelis nuokrypis nuo stechiometrijos. Tuo tarpu PI-MOCVD metodas leidžia keisti sluoksnių sudėtį plačiame

intervale tik pakeitus MO pirmtakų santykį tirpale. Šie tyrimai turėtų būti ypač aktualūs perovskitinių stanatų srityje, nes tokios jų savybės kaip, krūvininkų koncentracija bei jų judris, ypač jautrios įvairiems defektams.

Norint išsiaiškinti nestechiometrijos įtaką nelegiruotų BSO sluoksnių savybėms, buvo nusodinta serija BSO plėvelių, keičiant Sn/Ba santykį tirpale nuo 0,3 iki 0,7. EDX analizės metodo matavimai parodė, kad užaugintų sluoksnių sudėtis (Sn/Ba) kito atitinkamai nuo 0,54 iki 1,3. θ-2θ difraktogramos parodė (Pav. 18, 46 psl), kad nepriklausomai nuo padėklo, sluoksniai, kurių sudėtis artima stechiometrinei arba pasižymėjo Ba pertekliumi, buvo grynafaziai. Tuo tarpu esant Ba trūkumui sluoksniuose egzistuoja dviejų $BaSnO_3$ bei SnO_2 fazių mišinys.

Nustatyta ir padėklo įtaka. Užauginti BSO sluoksniai ant LAO ir STO padėklų, nepriklausomai nuo Sn/Ba santykio, buvo ne tik tekstūruoti a-ašimi, bet ir epitaksiniai. Tačiau sluoksnių, užaugintų ant Al_2O_3 padėklų, kristalitai buvo orientuoti chaotiškai. Be to, epitaksinių sluoksnių difraktogramose pastebėta tendencija: didėjant bario kiekiui sluoksniuose charakteringos (*l00*) smailės tapdavo vis platesnės ir esant Sn/Ba santykiui mažesniam nei 0,97, buvo stebimas jau dvigubas šių smailių pobūdis. Toks efektas gali būti susijęs arba su Ruddlesden-Popper (RP) fazių atsiradimu, arba/ir su likutiniais įtempimais sluoksniuose.

Kadangi BSO priklauso perovskito tipo struktūrai, papildomas BaO sluoksnių įterpimas gali būti toleruojamas [108] ir tokiu būdu gali formuotis sluoksniuota $Ba_{n+1}Sn_nO_{3n+1}$ struktūra. Šioje hipotetinėje struktūroje n – tai nuosekliai viršūnėmis sujungtų SnO_6 oktaedrų sluoksnių skaičius, atskirtas BaO sluoksnių. Dvimatės Ba_2SnO_4 struktūros atveju (n=1), kai gardelės tūris yra didžiausias, struktūra aprašoma tetragonine simetrija (a=4,1411 Å, c=13,27 Å [104]). Didėjant n skaičiui, įsiterpusių BaO sluoksnių tampa vis mažiau, ir esant $n=\infty$, t.y. perovskito tipo kubinėje struktūroje, gardelės parametras turėtų pasiekti minimumą (a=4,117 Å [23, 87, 88]). Tokia teorija paaiškintų tolygų gardelės parametrų didėjimą mažėjant Sn/Ba santykiui sluoksniuose (Pav. 19, 48 psl.), jei tik RP fazė augtų c-ašimi statmenai padėklui. Tačiau paaiškinti smailių dubletą tokia teorija nelabai tinkama.

Kita vertus, dvigubas smailių atsiradimas difraktogramose gali būti susijęs su likutiniais įtempimais gana plonuose (160 – 175nm) BSO sluoksniuose. Nors STO ir LAO yra perovskito tipo struktūros padėklai, jų gardelės parametrai nesutampa su BSO parametru, ir šis nesutapimas yra atitinkamai ~5% ir ~8%. Esant tokiam gana dideliam nesutapimui, dalis sluoksnio gali būti įtempta, o kita dalis egzistuoti relaksuotoje būsenoje.

Panašus efektas buvo stebimas ir gana storuose 560 nm perovskito tipo $LaNiO_3$ sluoksniuose, užaugintuose PLD būdu [148]. Papildomas argumentas likutinių įtempimų naudai galėtų būti ir nustatyta tendencija, kad kuo didesnis nesutapimas tarp padėklo ir gardelės, tuo mažesnis smailių išsiskyrimas difraktogramose. Polikristaliniams sluoksniams ant Al_2O_3 (0006) padėklų šis efektas nebuvo būdingas.

Sluoksnių, užaugintų ant LAO ir STO padėklų epitaksijos patikrinimui buvo atlikti tekstūros matavimai. Šiam tikslui buvo matuotos (110) ir (200) polių figūros (Pav. 20, 49 psl.). Tyrimai parodė, kad sluoksniai, kurių sudėtis buvo artima stechiometrinei (Sn/Ba=1,02), užaugo epitaksiškai ir buvo orientuoti „kubas ant kubo“ padėklo atžvilgiu. Tai reikštų, kad epitaksiniai sąryšiai tarp sluoksnio ir padėklo buvo BSO(*l*00)||STO(*l*00) ir BSO(*l*00)||LAO(*l*00). Jų svyravimo kreivių (ω) plotis pusėje aukščio (FWHM) bei ϕ-skenavimo kreivių FWHM reikšmės buvo atitinkamai 0,3 ° ir 0,8 °. Tuo tarpu sluoksniuose su didesniu bario kiekiu (Sn/Ba=0,81) šios reikšmės buvo didesnės: 1,0 ° ir 1,5 °. Tai reikštų didesnį kristalitų išsibarstymą sluoksniuose ir statmenai padėklui, ir padėklo plokštumoje. Tikėtina, toks efektas susijęs su konkurencingos {221} kristalitų orientacijos didėjimu. Šios orientacijos silpni atspindžiai buvo vos matomi sluoksnių polių figūrose ant LAO padėklų (Pav. 20 (c,d), 49 psl.). Ba pertekliaus tolerancija BSO sluoksniuose stebima gana plačiame intervale be jokių papildomų fazių susidarymo.

Optinių BSO sluoksnių savybių įvertinimui buvo matuojami šviesos pralaidumo spektrai UV ir regimosios spinduliuotės srityje. Šiam tikslui buvo naudojami sluoksniai, užauginti ant Al_2O_3 (0006) padėklų (Pav. 22 , 53 psl). Tyrimai rodo, kad šie sluoksniai pasižymi didesniu nei 80 % regimosios šviesos pralaidumu. Be to, aiškiai matoma sluoksnių sudėties įtaka optinio pralaidumo kraštui ultravioletinėje srityje. Stebima tendencija, kad didėjant Ba kiekiui sluoksnyje, didėja ir optinės draustinės energijos juostos pločio vertė (E_g). Paskaičiuotos E_g reikšmės yra didesnės (E_g > 3,42 eV) nei stechiometriniam kristalui įvertintos literatūroje minimos reikšmės (E_g = 3,33 eV) [1]. Tokie rezultatai gali būti paaiškinti tuo, kad netiesioginis draustinis juostos plotis glaudžiai susijęs su medžiagos struktūra ir yra jautrus cheminiam gardelės plėtimuisi [153]. Tokiu būdu, anksčiau aptartas gardelės parametro kitimas nuo Sn/Ba santykio sluoksnyje koreliuoja su atitinkamu E_g reikšmių pokyčiu.

Nestechiometrijos įtaka lantanu legiruotų plonų $BaSnO_3$ sluoksnių savybėms

Tiriant nestechiometrijos įtaką lanatanu legiruotų BSO sluoksnių savybėms buvo nusodintos dvi sluoksnių serijos – ploni (~160 nm) ir stori (~380 nm) sluoksniai.

Pirmos serijos atveju, keičiant Sn/(Ba+La) santykį tirpale/sluoksnyje LBSO plėveles buvo auginamos 160 – 175 nm storio. La kiekis sluoksniuose, nustatytas EDX metodu, buvo 2,5 ± 0,2 $\%_{atominiai}$. Šios serijos tikslas buvo palyginti gautus rezultatus su nelegiruotų BSO sluoksnių savybėmis. Sluoksniai buvo auginami ant LAO, STO ir Al_2O_3 padėklų. XRD tyrimai parodė, kad La legiravimas nedaro įtakos nei nustatytai tendencijai keičiant Sn/Ba santykį, nei sluoksnių epitaksijai, nei gardelės parametrams ant LAO ir STO padėklų. Tačiau gardelių parametrų padidėjimas, esant tam pačiam Sn/Ba santykiui sluoksnyje, buvo aiškiai stebimas tik polikristaliniuose LBSO||Al_2O_3 sluoksniuose. Tikėtina, kad gardelių parametrų padidėjimas iš dalies turėjo įtakos ir optinėms LBSO sluoksnių savybėms (Pav. 22, 53 psl). Nustatyta, kad esant tam pačiam Sn/Ba santykiui, legiruotose sluoksniuose E_g reikšmės yra didesnės.

Įdomi tendencija buvo stebima ir lyginant legiruotų, ir nelegiruotų sluoksnių morfologiją. BSO sluoksnių atveju galima buvo išskirti tris charakteringus morfologijos tipus (Pav 21, 51 psl.). Esant Ba trūkumui formuojasi šiurkštus paviršius, kuris sudarytas iš mažų, atskirų kristalitų. Tuo tarpu, esant artimai stechiometrinei sudėčiai, sluoksniai pasižymi lygia matrica su gana didele dislokacijų koncentracija. Ba pertekliaus atveju formuojasi paviršius, kuriame lygioje matricoje matomi netaisyklingos tetraedrinės formos kristalitai būdingi {221} orientacijai. Mažėjant Sn/Ba santykiui sluoksniuose šių struktūrinių defektų tankis didėjo. Panašūs trys charakteringi morfologijos tipai būdingi ir LBSO sluoksniams tik su nedideliu sudėties poslinkiu į Ba pertekliaus pusę. Šiuo atveju, lygūs LBSO sluoksniai gaunami esant Sn/(Ba + La) santykiui ~0,90. Šių sluoksnių TEM ir HRTEM tyrimai parodė, kad augimo pradžioje (~70 nm) sluoksnis auga epitaksinis, pagal sluoksnis-po-sluoksnio mechanizmą. Tačiau esant didesniam storiui, stebimas koloninis augimas su tokiais struktūriniais defektais kaip kristalitų sandūros bei dislokacijos. Tokiu būdu, sluoksniai yra mišraus, įtempto bei relaksuoto tipo.

LBSO sluoksnių Hall‘o matavimai parodė, kad Sn/(Ba + La) santykis daro įtaką elektrinėms savybėms (Pav 22 (b,c,d), 52 psl). Nors krūvininkų

koncentracija buvo pakankamai didelė ($2,6 \times 10^{20}$ cm^{-3}), maksimalus, palyginant nedidelis, krūvininkų judris (~20 $cm^2V^{-1}s^{-1}$) buvo išmatuotas, kai Sn/(Ba + La) santykis sluoksniuose buvo 0,97. Krūvininkų judris paprastai susijęs su sluoksnių morfologija. Šių sluoksnių paviršius buvo sudarytas iš suraizgytų lygios matricos takelių (Pav 21, 51 psl). Tuo tarpu, lygaus paviršiaus sluoksnių judris buvo mažesnis.

Nestechiometrijos įtaka lantanu legiruotų storų $BaSnO_3$ sluoksnių savybėms

Auginant antrąja nusodinimų seriją (~380 nm) buvo sprendžiamos pasiekto mažo krūvininkų judrio problemos. Mokslinėje literatūroje pasiūlyti keli šios problemos sprendimo būdai. Vienas iš variantų galėtų būti buferinio sluoksnio įvedimas tarp LBSO sluoksnio ir padėklo. Tai galėtų būti $BaSnO_3$ [26] arba $SrZrO_3$ [154] pasluoksniai, kurie panaikina ar gerokai sumažina kristalinių gardelių nesutapimą. Manoma, kad būtent kristalinių gardelių nesutapimo dislokacijos, nusodintuose sluoksniuose, yra atsakingos dėl daug mažesnių judrio verčių nei kristaluose. Esant tokiam įterptam buferiniam pasluoksniui vyksta nesutapimo dislokacijų anihiliacija ir LBSO sluoksniuose pasiekiamos patrauklios krūvininkų judrio ~140 $cm^2V^{-1}s^{-1}$ reikšmės. Kita vertus, A. Sanchela ir kiti [155], įvertindami nusodinto sluoksnio storio įtaką LBSO sluoksnių savybėms, padarė išvadą, kad nei dislokacijų tankis, nei padėklo prigimtis nedaro tokios didelės įtakos krūvio nešėjų judriui lyginant su sluoksnio storiu. Be to, jų priklausomybės nuo sluoksnio storio tyrimai parodė, kad LBSO sluoksnių ant STO ir MgO padėklų atveju, sluoksnio storiui esant didesniam nei 350 nm, judrio reikšmės ~ 95 – 100 $cm^2V^{-1}s^{-1}$ nebesikeičia. Šiame kontekste, pakankamai storiems sluoksniams būtų naudingas nestechiometrijos tyrimas, nes galėtų atskleisti defektų įtaką bei LBSO sluoksnių ypatybes. Storų sluoksnių nusodinimo procesui ir geresniam sudėties valdymui naudoti du injektoriai.

Morfologijos tyrimai parodė, kad anksčiau aprašyti trys charakteringi morfologijos tipai priklausomai nuo sudėties, būdingi ir storiems LBSO sluoksniams užaugintiems ant STO ir MgO padėklų (Pav. 23, 55 psl.). Lygiausi LBSO sluoksniai, nepriklausomai nuo padėklo prigimties, buvo gauti esant Sn/Ba santykiui apie 0,98. Labai lygus paviršius (R_a = 0,28 nm) buvo gautas LBSO||STO sluoksnių atveju, nors sluoksnių augimo greitis buvo

gana didelis ~5 nm/min. Tuo tarpu paviršius ant MgO padėklų buvo daug šiurkštesnis (R_a ~ 5 nm).

XRD tyrimai parodė, kad visi užauginti LBSO sluoksniai, ant MgO ir STO padėklų, nepriklausomai nuo Sn/Ba sudėties, buvo grynafaziai ir epitaksiniai. Svarbiausias šių tyrimų rezultatas buvo epitaksinių LBSO sluoksnių sąryšis tarp morfologijos, gardelės parametrų kitimo bei elektrinių savybių. Apskaičiuoto LBSO sluoksnių kubinės gardelės parametro statmenai padėklui priklausomybė nuo Sn/Ba santykio pateikta Pav. 24 (b) (57 psl.). Kaip ir morfologijos atveju, galima išskirti tris charakteringas sritis: Sn pertekliaus, nedidelė Ba pertekliaus sritis su gardelės parametro lūžio tašku, bei sritis su staigiu gardelės parametro didėjimu.

Sn pertekliaus srityje, LBSO sluoksnių užaugintų ant STO padėklų gardelės parametras buvo $4{,}117 \pm 0{,}001$ Å. Tokios gardelės parametro reikšmės yra būdingos ir LBSO didesnių dimensijų keramikai, esant La kiekiui apie $2 - 3\ \%_{\text{atominiai}}$ [65, 79]. LBSO perovskito struktūra mažai toleruoja perteklinį Sn atomų/jonų kiekį, todėl gardelės parametrai beveik nekinta ir susidaro pašalinė SnO_2 fazė [26].

Pakankamai didelio Ba pertekliaus srityje, LBSO sluoksnių gardelės parametras akivaizdžiai didėja. Šiuo atveju, perteklinis bario kiekis įsiterpia į LBSO perovskito struktūrą BaO sluoksnių pavidalu. Susidaro Ruddlesden-Popper fazės. Pažymėtina, kad LBSO||STO ir LBSO||MgO sluoksnių gardelių parametrai šioje srityje sutampa, esant tam pačiam Sn/Ba santykiui sluoksnyje.

Vis dėlto įdomiausia sritis yra ties Sn ir Ba perteklinių sričių susikirtimu. Šiam atvejui apibūdinti labiausiai tiktų stechiometrijos sąvoka. Tačiau, ji sąmoningai nevartojama dėl dviejų priežasčių. Pirma – La jonų (atomų) pasiskirstymas perovskito struktūroje gali būti dvejopas ir, esant nedideliam jo kiekiui, energetiškai naudingiausia užimti Ba poziciją. Tačiau, esant nukrypimui nuo stechiometrijos, situacija gali keistis ir dalis La atomų/jonų gali užimti ir Sn poziciją. Kita priežastis yra susijusi su lūžio taško poslinkiu į perteklinio Ba pusę (~0,98), net neįskaičiuojant legiravimo lantanu. Toks Ruddlesden-Popper (RP) fazių atsiradimo uždelsimas, priklausomai nuo stechiometrinės sudėties, yra būdingas ir $SrTiO_3$ perovskito tipo struktūrai [160]. Stroncio titanato struktūros atveju, esant nedideliam pertekliniam Sr kiekiui $0{,}95 \leq Sr/Ti < 1$, vyksta ne SrO sluoksnių įsiterpimas į perovskito struktūrą, o Ti pozicijų pakeitimas Sr atomais kartu susidarant deguonies vakansijų defektams. Pagal analogiją, galima būtų įtarti, kad ir LBSO struktūroje vyksta panašus mechanizmas. Tačiau, šiuo atveju legirantas La užima Sn poziciją. Tai ir gali lemti minėtą poslinkį. Svarbu paminėti tai,

kad būtent ties RP fazių atsiradimo tašku, kai Sn/Ba santykis yra ~0,98, LBSO||STO sluoksniai pasižymėjo ne tik lygiausia morfologija, bet ir didžiausiomis krūvio nešėjų judrio reikšmėmis – μ=120,5 ± 0,6 $cm^2V^{-1}s^{-1}$.

LBSO sluoksnių mikrostruktūros tyrimai parodė, kad Sn/Ba santykis sluoksnyje daro įtaką ir kristalinės orientacijos laipsniui. Pastarasis apibūdinamas dviem parametrais: tai svyravimo kreivių (ω) pusplotis pusėje aukščio (FWHM), rodantis sluoksnio kristalitų išsibarstymo laipsnį statmenai padėklui (Pav. 24 (c), 57 psl.) ir φ-skenavimo kreivių FWHM reikšmės, rodančios kristalitų išsibarstymo laipsnį lygiagrečiai padėklui. Abiejų šių parametrų kitimas nuo sluoksnio sudėties buvo asimetrinis su aiškiu minimumu ties Sn/Ba santykiu ~0,98. Net mažiausios reikšmės rodo, kad ir LBSO||STO (ω_{FWHM} = 0,30 °; ϕ_{FWHM} = 0,60 °) ir LBSO||MgO (ω_{FWHM} = 0,36 °; ϕ_{FWHM} = 0,55 °) sluoksniai nepasižymėjo tobula mikrostruktūra, lyginant su monokristaliniais padėklais (STO: ω_{FWHM}=0,13 °; ϕ_{FWHM} = 0,90 °; MgO: ω_{FWHM} = 0,14 °; ϕ_{FWHM} = 0,20 °).

Hall'o matavimai kambario temperatūroje parodė glaudų sąryšį tarp sluoksnių elektrinių savybių ir sudėties (Pav. 25, 59 pls.). Šių tyrimų dėka buvo nustatytos ne tik didelės krūvininkų koncentracijos (~ 4,5 × 10^{20} cm^{-3}), bet ir dideli krūvio nešėjų judriai: μ=120,5 ± 0,6 $cm^2V^{-1}s^{-1}$ ant STO padėklų bei μ=84,6 ± 0,2 $cm^2V^{-1}s^{-1}$ LBSO||MgO atveju. Tokios gautos vertės gali būti palygintos su geriausiais molekulinių pluoštų epitaksijos (MBE) metodu gaunamais rezultatais, nors sluoksniai buvo užauginti gana dideliu augimo greičiu (~5 nm/min), kurių mikrostruktūra nebuvo tobula.

Elektrinių savybių tyrimų rezultatai parodo labai stiprią nestechiometrijos įtaką. Geriausi krūvio nešėjų judrio rezultatai buvo gauti gana siaurame intervale, esant Sn/Ba santykiui apie ~0,98. Tuo tarpu krūvininkų koncentracijos kitimas nuo Sn/Ba sudėties pasižymėjo gana plačia parabolinio tipo priklausomybe su maksimumu ties Sn/Ba ≈ 1. Gana didelis krūvininkų koncentracijos išbarstymas iš dalies gali būti susijęs su nemažu La legiravimo išsibarstymo laipsniu. Kita vertus, krūvininkų koncentracijos kitimo pobūdis yra glaudžiai susijęs su įvairiais kitais nestechiometrijos defektais. Šių nestechiometrinių defektų įtaka aprašoma trimis tikėtinais krūvio kompensacijos mechanizmais (59 – 60 psl.)

Apibendrinant visus atliktus tyrimus galima teigti, jog PI-MOCVD metodas buvo sėkmingai optimizuotas ir pritaikytas plonų SnO_2, $BaSnO_3$, La:$BaSnO_3$ sluoksnių sintezei. Ištirtos La-Ba-Sn-O oksidinės sistemos sluoksnių morfologijos ir mikrostruktūros priklausomybės nuo mažai nagrinėjamo veiksnio – stechiometrijos. Optimizuojant ir derinant nusodinimo sąlygas bei padėklus, pasiektos didelės krūvininkų judrio vertės

palyginamos su fizikinių metodų rezultatais. Gautieji rezultatai yra svarbūs atliekant tolimesnius tyrimus, dėl galimo šių medžiagų platesnio pritaikymo įvairioje funkcinių oksidų elektronikoje.

IŠVADOS

1. Iš daugelio alavo metaloorganinių junginių atrinkti keturi potencialūs alavo pirmtakai LBSO sintezei MOCVD būdu: PODA, PODB, $Sn(thd)_2$, $Sn(Bu)_2(acac)_2$. Kinetiniai tyrimai, nusodinant alavo oksido sluoksnius, atlikti skirtingose temperatūrose, parodė, kad lakių pirmtakų terminis stabilumas gali būti išdėstytas šia tvarka: PODA > PODB > $Sn(thd)_2$ > $Sn(Bu)_2(acac)_2$.
2. Lakūs, termiškai stabilūs, bei tarpusavyje suderinami $Sn(thd)_2$, $Ba(thd)_2$*triglimas ir $La(thd)_3$*monoglimas metaloorganiniai pirmtakai tinkami plonų nelegiruotų ir lantanu legiruotų bario stanato sluoksnių PI-MOCVD sintezei.
3. Pirmą kartą, PI-MOCVD metodas buvo pritaikytas nelegiruoto bario stanato ir La-legiruoto bario stanato sluoksnių sintezei ant įvairių padėklų. Esant 850 °C nusodinimo temperatūrai, epitaksiniai sluoksniai užauginti ant $LaAlO_3$ (*l*00), $SrTiO_3$ (*l*00), MgO (*l*00) padėklų. Polikristaliniai - ant Al_2O_3 (0006) padėklų.
4. Keičiant Sn/Ba santykį epitaksiniuose sluoksniuose nustatytos trys skirtingos sluoksnių morfologijos: 1) šiurkštaus paviršiaus, sudaryto iš atskirų kristalitų, esant Sn pertekliui; 2) lygios matricos arba „takelių“ morfologija, esant artimos stechiometrijai sudėties atveju; 3) lygios matricos su piramidės formos ({221} orientacijos) kristalitais paviršiuje, esant Ba pertekliui.
5. Nustatyta, kad BSO ir LBSO sluoksnių gardelės parametras akivaizdžiai didėjo, didėjant bario kiekiui, kai Sn/Ba < 0,98. Tuo tarpu gardelės parametras 0,98 < Sn/Ba < 1,10 srityje kito nereikšmingai.
6. XRD ir TEM tyrimai parodė dvejopą plonų (~160 nm) BSO ir LBSO sluoksnių mikrostruktūros prigimtį esant Sn/Ba < 1. Augimo pradžioje (< 70 nm) sluoksnis auga epitaksinis ir yra įtemptas iki ~70 nm. Likusi sluoksnio dalis yra atpalaiduota, pasižyminti koloniniu augimu bei struktūriniais defektais, tokiais kaip kristalitų sandūros bei dislokacijos.
7. Keičiant Sn/Ba santykį BSO sluoksniuose kito ir sugertis UV srityje. Buvo stebimas hipsochrominis sugerties krašto poslinkis bei draustinės energijų juostos pločio (E_g) didėjimas, mažinant Sn/Ba santykį sluoksniuose.

LBSO sluoksniai pasižymėjo didesnėmis E_g vertėmis nei nelegiruoti BSO sluoksniai.

8. Nustatyta, kad LBSO sluoksnių nusodintų ant $SrTiO_3$ padėklų storis (160 – 380 nm) neturi įtakos jų morfologijai bei mikrostruktūrai. Kita vertus, ~380 nm sluoksnių sudėtis (Sn/Ba) stipriai lemia sluoksnių elektrines savybes.

9. n-tipo LBSO sluoksnių krūvininkų koncentracijos kitimas nuo Sn/Ba sudeties pasižymėjo plačia parabolinio tipo simetrine priklausomybe. Didžiausios krūvio nešėjų koncentracijos vertės pasiektos, esant Sn/Ba≈1 sudėčiai: $n=3\div5\times10^{20}$ cm^{-3}. Tuo tarpu, krūvininkų judriui reikšmingą įtaką darė sluoksnių morfologija. Didžiausios judrio vertės, palyginamos su MBE gautų sluoksnių judrio vertėmis, nustatytos esant lygiausios morfologijos sluoksniams siauroje Sn/Ba≈0,98 srityje: $\mu=120,5 \pm 0,6$ $cm^2V^{-1}s^{-1}$ bei $\mu=84,6 \pm 0,2$ $cm^2V^{-1}s^{-1}$ atitinkamai, ant STO ir MgO padėklų.

GYVENIMO APRAŠYMAS

ASMENINĖ INFORMACIJA	
Vardas, pavardė	Tomas Murauskas
Gimimo data	1991-09-05
Adresas	Eišiškių pl. 26-28, Vilnius
Telefono numeris	+370 608 37502
El. pašto adresas	tmurauskas1991@gmail.com

IŠSILAVINIMAS IR KVALIFIKACIJA	
2010 – 2014	Chemijos bakalauro kvalifikacinis laipsnis, Vilniaus universitetas
2014 – 2016	Chemijos magistro kvalifikacinis laipsnis, Vilniaus universitetas

DARBO PATIRTIS		
2011-09 – 2015-09	Vilniaus universiteto, Bendrosios ir neorganinės chemijos katedra	laborantas
2015-06 – 2016-03	Vilniaus universiteto Neorganinės chemijos laboratorija	Vyresnysis specialistas
2016-03 – 2020-01	Nacionalinė visuomenės sveikatos priežiūros laboratorija	Instrumentinių tyrimų poskyrio vedėjas
2020-01 – iki dabar	Vilniaus universitetas, Chemijos institutas	Jaunesnysis mokslinis darbuotojas

DALYVAVIMAS MOKYMUOSE IR TARPTAUTINĖSE MOKYKLOSE	
2016-10-17 – 2016-10-21	Jaunųjų mokslininkų bendrųjų kompetencijų gebėjimų mokymai
2019-05-27 – 2019-05-31	Konferencija – mokykla “The 2019 Spring Meeting of the European Materials

	Research Society (E-MRS)", Nica, Prancūzija
2020-08-24 – 2020-08-28	22nd international school Advanced materials and technologies, Palanga, Lietuva
PAPILDOMA VEIKLA	
2016-03 – 2020-01	Nacionalinės visuomenės sveikatos laboratorijos Horizon 2020 projektų koordinatorius, Jungtinių veiksmų projektų Lietuvos atsovas Europos komisijoje

ACKNOWLEDGEMENTS

I am very honored and extremely grateful to write this chapter, which to me seems as one of the most difficult chapters to write. As I think about all of the possible input of the wonderful people involved in the past years, it is truly and whole-heartedly difficult to describe the sheer efforts people have put in my personal development. The care, attention, patience, trust, belief and many more words would be necessary to describe the support which others showered me with in this long journey.

I would like to express the most profound gratitude to my supervisor, **Assoc. Prof. Dr. Valentina Plaušinaitienė** for her unparalleled conviction and investment of her precious time in passing down the knowledge and the unique outlook on science. Her encouragement and guidance were most important for this work to proceed in the right direction and to be successfully realized.

I am particularly grateful to the closest colleagues for all the help, encouragement, joyous, and challenging moments together. For long and different-sided discussions with Virgaudas Kubilius, support and friendship-bearing moments, and homely working atmosphere with Milita Vagner and Sabina Kuprėnaitė, challenging and improvement encouraging moments with former supervisor professor Adulfas Abrutis.

I wish to extend my warmest thanks to all colleagues from Faculty of Chemistry and Geoscience for their support and assistance with the multitude of measurements and experiments undertaken during these years. Their provided opportunities, willingness to share knowledge and trust in my abilities has provided many opportunities for personal development as a young scientist.

Finally, I would like to acknowledge the support, care and love from my family and friends through all the challenging moments. Their support kept me going despite any obstacles. This work could not be finished without their aid. My deepest gratitude to goes to them.

LIST OF PUBLICATIONS

Articles in journals included in the thesis

I. J. Podhorsky, T. Murauskas, C. Hegemann, D. Graf, T. Fischer, M. Babiak, J. Pinkas, V. Plausinaitiene, S. Mathur, A. Abrutis, Z. Moravec, Preparation of Heteroleptic Tin(IV) N,O-β-heteroarylalkenolate Complexes and Their Properties as PI-MOCVD Precursors for SnO_2 Deposition, *European Journal of Inorganic Chemistry*, 10.1002/ejic.201800913 (2018).

II. T. Murauskas, V. Kubilius, Z. Saltyte, V. Plausinaitiene, Metalorganic chemical vapor deposition and investigation of nonstoichiometry of undoped $BaSnO_3$ and La-doped $BaSnO_3$ thin films, *Thin Solid Films*, 692 (2019) 137575.

Articles in journals not included in the thesis

I. A. Bartasyte, V. Plausinaitiene, A. Abrutis, T. Murauskas, P. Boulet, S. Margueron, J. Gleize, S. Robert, V. Kubilius, and Z. Saltyte, Residual stresses and clamped thermal expansion in $LiNbO_3$ and $LiTaO_3$ thin films, *Applied Physics Letters*, 101 (2012) 122902.

II. S. Kuprenaite T. Murauskas, A. Abrutis, V. Kubilius, Z. Saltyte, V. Plausinaitiene, Properties of In-, Ga-, and Al-doped ZnO films grown by aerosol-assisted MOCVD: Influence of deposition temperature, doping level and annealing, *Surface Coatings and Technology*, 271 (2015) 156-164.

III. S.Kuprenaite, A. Abrutis,V. Kubilius, T. Murauskas, Z. Saltyte, V.Plausinaitiene, Effects of annealing conditions and film thickness on electrical and optical properties of epitaxial Al-doped ZnO films, *Thin Solid Films*, 599 (2016) 19-26.

IV. A. Abrutis, L. Silimavicius, V. Kubilius, T. Murauskas, Z. Saltyte, V. Plausinaitiene, Doped zinc oxide films grown by hot-wire chemical vapour deposition, *Thin Solid Films*, 576 (2015) 88-97.

V. A. Valiūnienė, Ž. Margarian, I. Gabriūnaitė, V. Matulevičiūtė, T. Murauskas, G. Valinčius, Cadmium Stannate Films for Immobilization of Phospholipid Bilayers, *Journal of Electrochemical Society*, 163 (2016) H762-H767.

VI. A. Abrutis, L. Silimavicus, V. Kubilius, T. Murauskas, Z. Saltyte, S. Kuprenaite, V. Plausinaitiene, On the possibility to grow zinc oxide-based transparent conducting oxide films by hot-wire chemical vapor deposition, *Journal of Vacuum Science & Technology A*, 32 (2014) 020602.

VII. S. Kuprenaite, A. Abrutis, V. Plausinaitiene, A. Arkhangelskiy, V. Kubilius, L. Silimavicius, T. Murauskas, Z. Saltyte, Properties of Al-doped ZnO films grown by atmospheric pressure MOCVD on different orientation sapphire substrates, *Integrated Ferroelectrics*, 173 (2016) 128-139.

Published contributions to academic conferences

1. T. Murauskas, V. Plaušinaitienė, PI-MOCVD DEPOSITION AND INVESTIGATION OF UNDOPED BARIUM STANATE THIN FILMS, *61st International Conference for Students of Physics and Natural Sciences Open Readings 2018*, April 20 – 23, 2018, Vilnius, Lithuania.
2. G. Gaidamavičienė, T. Murauskas, A. Žalga, Thermoanalytical and structural studies on alkaline earth metals substituted $La_2Mo_2O_9$ materials, *61st International Conference for Students of Physics and Natural Sciences Open Readings 2018*, April 20 – 23, 2018, Vilnius, Lithuania.
3. G. Gaidamavičienė, T. Murauskas, P. Normantas, V. Aleksa, A. Žalga, Spectroscopic study of La-RE-Mo-O tartrate precursors and $La_{2-x}RE_xMo_2O_9$ (RE=Nd, Sm, Eu, Dy) ceramics obtained by sol-gel method, *61st International Conference for Students of Physics and Natural Sciences Open Readings 2018*, April 20 – 23, 2018, Vilnius, Lithuania.
4. G. Gaidamavičienė, Ž. Gricius, T. Murauskas, M. Smolianskis, V. Aleksa, A. Žalga, Raman and infrared study of $La_{2-x}Y_xMo_2O_9$, *61st International Conference for Students of Physics and Natural Sciences Open Readings 2018*, April 20 – 23, 2018, Vilnius, Lithuania.
5. G. Gaidamavičienė, J. Gadeikis, T. Murauskas, Ž. Tokarevas, V. Aleksa, A. Žalga, Raman spectroscopic study on the structure of

$La_{2-x}Dy_xMo_2O_9$, *61st International Conference for Students of Physics and Natural Sciences Open Readings 2018*, April 20 – 23, 2018, Vilnius, Lithuania.

6. T. Murauskas, V. Plaušinaitienė, V. Kubilius. BARIUM STANATE: PI-MOCVD THIN FILM DEPOSITION AND NONSTOICHIOMETRY ISSUES, *62nd International Conference for Students of Physics and Natural Sciences Open Readings 2018*, April 20 – 23, 2018, Vilnius, Lithuania.
7. T. Murauskas, V. Plaušinaitienė, V. Kubilius, BARIUM STANATE: PI-MOCVD THIN FILM DEPOSITION AND NONSTOICHIOMETRY ISSUES, *62nd International Conference for Students of Physics and Natural Sciences Open Readings 2019*, April 19 – 22, 2019, Vilnius, Lithuania.
8. T. Murauskas, V. Plaušinaitienė, PI-MOCVD deposition of thin barium stannate films. Investigation of film nonstoichiometry, *Spring Meeting of the European Materials Research Society (E-MRS),* May 27 – 31, 2019, Nice, France.
9. T. Murauskas, M. Levulis, V. Plaušinaitienė, V. Kubilius, INVESTIGATION OF THIN PEROVSKITE La:$BaSnO_3$ FILMS' PROPERTIES USING DIFFERENT SUBSTRATES, *Advanced Materials and Technoloigy 2020*", August 24-28, 2020, Palanga, Lithuania.

1

Preparation of Heteroleptic Tin(IV) N,O-β-heteroarylalkenolate Complexes and Their Properties as PI-MOCVD Precursors for SnO_2 Deposition

J. Podhorsky, T. Murauskas, C. Hegemann, D. Graf, T. Fischer, M. Babiak, J. Pinkas,V.Plausinaitiene, S. Mathur, A. Abrutis, Z. Moravec

ChemPubSoc Europe

DOI: 10.1002/ejic.201800913

EurJIC European Journal of Inorganic Chemistry

Full Paper

MOCVD Precursors

Preparation of Heteroleptic Tin(IV) N,O-β-Heteroarylalkenolate Complexes and Their Properties as PI-MOCVD Precursors for SnO_2 Deposition

Jan Podhorsky,[a] Tomas Murauskas,[b] Corinna Hegemann,[c] David Graf,[c] Thomas Fischer,[c] Michal Babiak,[a,d] Jiri Pinkas,[a,d] Valentina Plausinaitiene,[b] Sanjay Mathur,*[c] Adulfas Abrutis,*[b] and Zdenek Moravec*[a]

Abstract: We have successfully prepared and structurally characterized five novel tin(IV) heteroleptic N,O-β-heteroarylalkenolates containing $-CF_3$ groups. The synthetic route used reactions of $Sn(OtBu)_4$ with 3,3,3-trifluoro(pyridin-2-yl)propen-2-ol (PyTFPH), 3,3,3-trifluoro(dimethyl-1,3-oxazol-2-yl)propen-2-ol (DMOTFPH), and 3,3,3-trifluoro(1,3-benzthiazol-2-yl)propen-2-ol (BTTFPH) in dry aprotic solvents leading to elimination of *tert*-butanol and formation of $Sn(OtBu)_2(PyTFP)_2$ (**1**), $Sn(OtBu)_2(DMOTFP)_2$ (**2**), and $Sn(OtBu)_2(BTTFP)_2$ (**3**). The chelating ligands employed a bidentate N∩O donor set. The reactivity of O*t*Bu groups in the obtained $Sn(OtBu)_2(N\cap O)_2$ complexes was further investigated in reactions with fluorinated alcohols, 2,2,2-trifluoroethanol (TFEH) and 1,1,1,3,3,3-hexafluoro-2-propanol (HFPH). Two complexes $Sn(TFE)_2(DMOTFP)_2$ (**4**) and $Sn(HFP)_2(PyTFP)_2$ (**5**) were obtained and structurally characterized. Thermal behavior of complexes **1**–**5** was studied by thermogravimetry and differential scanning calorimetry (TG/DSC). The most volatile compounds $Sn(OtBu)_2(PyTFP)_2$ (**1**) and $Sn(OtBu)_2(DMOTFP)_2$ (**2**) were chosen and tested in a PI-MOCVD process for the SnO2 growth on sapphire-C substrates. Film growth rates at different temperatures (500–900 °C), crystalline quality, surface roughness, transparency in UV/Vis-mid-IR spectral ranges have been investigated. The results showed that these two compounds are suitable precursors for MOCVD deposition of high quality SnO_2 films. Fabricated films displayed good response to CO and NO_2 in chemo-resistive gas sensing measurements.

Introduction

In recent years, tin dioxide is drawing extreme attention in academic and industrial research due to its versatility, stability, chemical, electronic and optical properties. Undoped SnO_2 is a wide band gap n-type semiconductor, owing to its lattice containing oxygen vacancies and tin interstitials.[1] Two important properties of tin dioxide - low electric resistance, combined with high optical transparency in the visible range of electromagnetic spectrum[2] have led to its use as an important component in advanced applications, such as photocatalytic systems,[3] solar cells,[4] or as anode materials for lithium and sodium ion batteries.[5] Another notable use of SnO_2 is in gas sensing area for both inorganic and organic gases.[6] While tin dioxide is naturally occurring as tetragonal cassiterite, as well as in orthorhombic and hexagonal forms,[7] advanced applications demand a large number of synthetic, processing, fabrication, and tailoring procedures. Among them are both chemical and physical approaches. Examples include various deposition techniques,[8] mechanochemical treatments,[9] microwave syntheses,[10] and hydrolytic[11] or non-hydrolytic[12] sol-gel methods.

One of the methods used for preparation of oxidic thin-films is metal-organic chemical vapor deposition (MOCVD) process. Typically, MOCVD process uses sublimation or evaporation in order to transfer solid or liquid precursors into the gas phase. The thermal properties of precursors, such as volatility and decomposition temperature, play a crucial role. In order to bypass the precursor volatility issue and to precisely control volatilization process, techniques, such as single liquid source pulsed injection MOCVD (PI-MOCVD), were developed.[13] This technique is based on flash-evaporation of micro-doses of precursor solution in light organic solvent such as THF, monoglyme, or hexane, injected sequentially into a hot evaporator under vacuum. The technique allows homogeneous and reproducible mixing of precursors in solution and vapor, and therefore it was often used for preparations of various mixed functional oxides, such as $SrTiO_3$, $La(Sr)MnO_3$, $LiNbO_3$, and $LiTaO_3$.[14]

[a] *Masaryk University, Faculty of Science, Department of Chemistry, Kotlarska 2, 611 37 Brno, Czech Republic*
E-mail: hugo@chemi.muni.cz
http://www.sci.muni.cz/en/SCI/
[b] *University of Vilnius, Faculty of Chemistry and Geosciences, Institute of Chemistry, Naugarduko 24, 03225 Vilnius, Lithuania*
E-mail: adulfas.abrutis@chf.vu.lt
http://www.chgf.vu.lt/en/
[c] *University of Cologne, Faculty of Mathematics and Natural Sciences, Department of Chemistry,*
Greinstraße 6, 50939 Köln, Germany
E-mail: sanjay.mathur@uni-koeln.de
http://www.mathnat.uni-koeln.de/?&L=1
[d] *Masaryk University, CEITEC MU,*
Kamenice 5, 62500 Brno, Czech Republic
Supporting information and ORCID(s) from the author(s) for this article are available on the WWW under https://doi.org/10.1002/ejic.201800913.

In bottom-up chemical preparations of metal oxides, precursor chemistry is of crucial importance. Molecular metal-organic compounds are commonly used as precursors for processing and decomposition towards desired materials by the MOCVD technique. Notable among such molecular precursors for thin-layer oxidic materials are compounds containing β-diketonate ligands. Generally less soluble than metal alkoxides, β-diketonates are poorly hydrolyzable and thus less susceptible towards degradation by air humidity when compared to the metal alkoxides. Thus the main interest in metal β-diketonates focuses on their volatility which is essential for their use as precursors for obtaining thin films by MOCVD. By contrast with the M–OR bond, M–β-diketonate bonding is more stable; tailoring is thus mostly achieved via ligand substituent groups. Bulky substituents (*t*Bu) and fluorinated alkyls have a beneficial effect of increasing volatility of the obtained complexes.[15] Simple β-diketonates have been used intensively as MOCVD precursors for a wide range of oxidic materials, including oxides of alkaline earths, lanthanides, both transition and main group metals.[16]

In order to tailor the β-diketonate ligands and further enhance their properties, various modifications of β-diketonates were described, beginning with trifluoroacetylacetonates of metals.[17] Metal complexes with bidentate O,O- and N,O-ligands with $–CF_3$ groups are now commonly used in wide variety of applications, ranging from MOCVD to ring opening polymerizations of lactones.[18] Interestingly, the introduction of fluorine into an alkoxy group can influence the behavior of obtained metal fluoroalkoxide; such modifications enhance volatility, Lewis acidity, as well as steric control over reactivity.[19] The hydrophobic nature of the $–CF_3$ groups can be exploited for the control of hydrolysis rates of moisture sensitive compounds, such as Sn(O*t*Bu)$_4$, and provides more hydrolytically stable precursors, that are easier to handle.[20] The properties of metal fluoroalkoxides make them attractive as a CVD precursors.[21] Fluoroalkoxy compounds of main group elements such as aluminium,[22] gallium,[23] and tin[24] were used in preparations of thin films.

Trifluoroacetonylazines (Scheme 1) are examples of N,O-β-heteroarylalkenolates which were first synthetized in 1998 by Kawase et al.[25] They possess several interesting properties for they use as ligands in coordination chemistry. In their chelating ligand–metal bonding, a high stability is typical, because of the +I effect of the aromatic part of ligand and the –I effect of the $–CF_3$ group.[26] The nitrogen containing aromatic donor part of the ligand and stabilizing chelating effects lead to metal organic complexes with a high thermal stability during vaporization, high chemical stability due to a six-coordinate metal center, a low tendency to form dimers caused by high N–M π-bonding contribution, and increased volatility imparted by highly electronegative outer periphery owing to the presence of fluorine atoms in the trifluoromethyl groups.[27] Another notable feature of the trifluoroacetonylazine ligand class is that so far, no incorporation of fluorine into deposited materials was observed due to thermolysis.[28–32] This can be explained by a high stability of C–F bonding, combined with electronic effects from the aromatic core, creating conjugated system, thus preventing ligand fragmentation during thermal treatment.

Since early 2010's metal trifluoroacetonylazine complexes attracted attention as practical MOCVD precursors. Trifluoroacetonylazine ligands have been successfully used to prepare oxides of uranium,[28] iron,[29] or cobalt.[30] While N,O-β-heteroarylalkenolates of Sn^{II} are known,[31] so far no studies have dealt with Sn^{IV} N,O-β-heteroarylalkenolates.

Our goal in this work, in addition to the synthesis of Sn^{IV} N,O-β-heteroarylalkenolates, their structural characterization and investigation of their properties, was to examine selected reactions of fluorinated alcohols with remaining O*t*Bu groups in the obtained complexes. These exchange reactions, introduced already in early 1950s by Bradley, Mehrotra, and Wardlaw[32] and commonly used in alkoxide chemistry, represent a facile route for derivatization of these complexes with the aim of increasing their volatility. Furthermore we investigated the thermal behavior of synthesized compounds and tested them as potential precursors in a pulsed liquid injection MOCVD process for thin-layer SnO_2 preparations. The fabricated sensors were used for detection CO and NO_2 gases.

Results and Discussion

The synthesis of heteroleptic complexes Sn(O^{t}Bu)$_2$(PyTFP)$_2$ (**1**), Sn(O^{t}Bu)$_2$(DMOTFP)$_2$ (**2**), and Sn(O^{t}Bu)$_2$(BTTFP)$_2$ (**3**) was carried out by reactions of Sn(O*t*Bu)$_4$ with 3,3,3-trifluoro(pyridin-2-yl)propen-2-ol (PyTFPH), 3,3,3-trifluoro(dimethyl-1,3-oxazol-2-yl)propen-2-ol (DMOTFPH), and 3,3,3-trifluoro(1,3-benzthiazol-2-yl)propen-2-ol (BTTFPH) in dry aprotic solvents. The crystalline products **1**–**3** were obtained in high yields. The heteroarylalkenols (N∩OH, Scheme 1) act as N,O-chelating ligands and substitute two O*t*Bu groups on Sn(O*t*Bu)$_4$. The reaction pathway is described in Equation (1):

$$Sn(OtBu)_4 + 2\ N{\cap}OH \rightarrow Sn(OtBu)_2(N{\cap}O)_2 + 2\ tBuOH \quad (1)$$

As for purification of crude products, sublimation (≈ 10^{-3} Torr) at 120 °C leads to removal of unreacted ligands as well as Sn(O*t*Bu)$_4$, leaving pure products (according to NMR), which themselves sublime at relatively high temperatures above 200 °C.

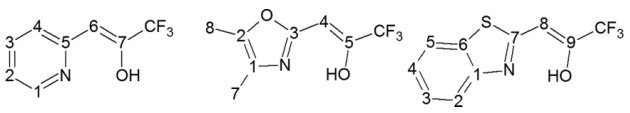

Scheme 1. Trifluoroacetonylazine ligands with atom numbering scheme (from left to right): 3,3,3-trifluoro(pyridin-2-yl)propen-2-ol (PyTFPH), 3,3,3-trifluoro(dimethyl-1,3-oxazol-2-yl)propen-2-ol (DMOTFPH) and 3,3,3-trifluoro(1,3-benzthiazol-2-yl)propen-2-ol (BTTFPH).

The tin(IV) centers in the obtained complexes **1**–**3** are six-coordinate, forming a deformed octahedron (Figure 1, Figure 2, and Figure 3), with two N,O-β-heteroarylalkenolate ligands and two remaining O*t*Bu groups. Only the $Sn(OtBu)_2(N\cap O)_2$ stoichiometry was obtained regardless of the type of ligand, reagent molar ratio (from 1:1 to 1:3), and the reaction temperature (from room temp. to 80 °C). The systems seem interesting from the stereochemical point of view, as in solution five stereoisomers are expected for the $Sn(OtBu)_2(N\cap O)_2$ complexes (Figure 4).

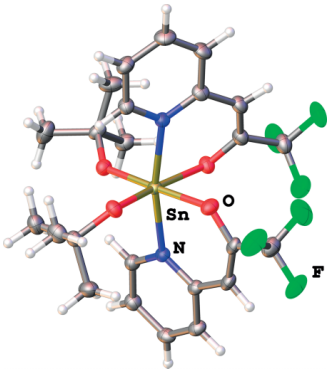

Figure 1. Molecular structure of $Sn(O^tBu)_2(PyTFP)_2$ (**1**).

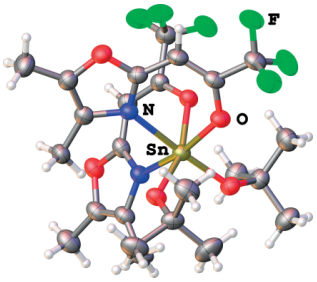

Figure 2. Molecular structure of $Sn(OtBu)_2(DMOTFP)_2$ (**2**).

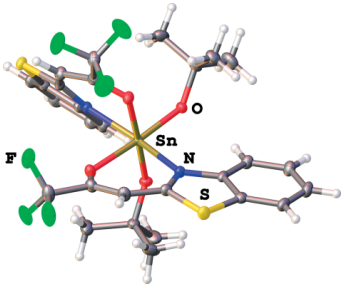

Figure 3. Molecular structure of $Sn(OtBu)_2(BTTFP)_2$ (**3**).

Crystallographic data and structure refinement parameters for all obtained compounds are summarized in Table S1. The molecular structures (Figure 1, Figure 2, and Figure 3) are shown as temperature ellipsoid plots at 50 % probability level. Hydrogen atom representations do not reflect atomic displacement parameters. A comparison of selected bond lengths and bond angles is shown in Table S2. An interesting observation is the dependence of the *cis*/*trans* orientation of the monodentate ligands. While *cis* positions were observed for complexes **1**–**3** containing the O*t*Bu group, the fluorinated alkoxo groups in **5** and **6** (see below) showed preference for *trans* positioning. The possible explanation is a high electron density and subsequent repulsion between the CF_3 groups. While the bond lengths of Sn–O in N∩O are similar to the comparable Sn^{II} compounds with N,O-β-heteroarylalkenolates,[31] the Sn–N bond is somewhat shorter, averaged around 2.2 Å, as compared with 2.4 Å in the Sn^{II} compounds. The Sn–OR bond length remains virtually unchanged and compares with $Sn(OtBu)_4$.[33]

The BTTFPH ligand has a very low solubility in all common solvents and this property has been carried over to the resulting complex **3**, which also shows extreme low solubility in both coordinating (THF) and non-coordinating solvents (toluene). This severely limits utility of this complex in PI-MOCVD, since good solubility in respective solvents is crucial for a PI-MOCVD precursor.

Five resonances in the ^{19}F NMR spectrum (Figure S1) confirmed the presence of five stereoisomers, although these cannot be unequivocally assigned by conventional NMR techniques. For $MX_2(N\cap O)_2$ type of octahedral complex, five stereoisomers are possible, with three of them being present as pairs of enantiomers.[34] Based on molecular symmetry (C_1, $2 \times C_2$, C_{2v}, C_{2h}) of the five stereoisomers, six resonances are expected in the ^{19}F NMR spectra, but only five were resolved. A situation encountered here, when a specific isomer is preferentially separates during the crystallization process is well-known and used for purification and enantiomer separation.[35]

The ^{119}Sn NMR spectra display high upfield shifts at around –700 ppm (Figure S2A and S2B) attributed to six-coordinate tin. ^1H and ^{13}C chemical shifts are comparable to analogous complexes with the N∩O ligands.[31] In the ^{13}C NMR spectra, resonances at ≈ 70 ppm for tertiary carbon atoms and at around 30 ppm for CH_3 groups confirm the presence of the O*t*Bu ligands attached to tin.

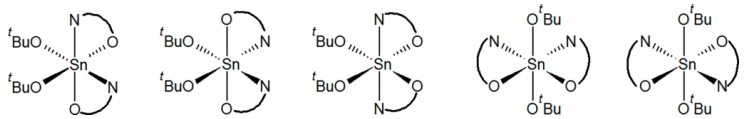

Figure 4. Five stereoisomers of $Sn(OtBu)_2(N\cap O)_2$.

The vibrational spectroscopy of the obtained $Sn(OtBu)_2(N\cap O)_2$ crystals have shown strong bands in the area of metal alkoxo group vibrations ν(Sn–O–C) in the range of 1000–1200 cm^{-1}, as well as ν(C_{sp3}–H) (2850–3000 cm^{-1}), that are further confirming bonding of O*t*Bu groups to tin. The ligand presence and its bonding to tin is substantiated by bands in the area of ν(C_{sp2}–H) (3000–3100 cm^{-1}) and strong bands in the area of C=C–Ar (1600–1700 cm^{-1}), in addition to skeletal C–C vibrations at 600–800 cm^{-1}, and Sn–N (400–500 cm^{-1}). The fragments found by mass spectrometry have included $[Sn(OtBu)(N\cap O)_2]^+$, $[Sn(N\cap O)_2]^+$ and $[Sn(N\cap O)]^+$. The higher relative intensities are typical for fragments with Sn–N∩O ligand bonding, rather than for Sn–O*t*Bu, suggesting, that this bond undergoes cleavage more easily.

The calculated residual masses for thermal decomposition of the complexes **1**, **2**, and **3** to SnO_2 are 23 %, 22 %, and 20 %, respectively. According to TG/DSC analysis of obtained $Sn(OtBu)_2(N\cap O)_2$ complexes (Figure 5), there is a very similar behavior between $Sn(OtBu)_2(PyTFP)_2$ (**1**) and $Sn(OtBu)_2(DMOTFP)_2$ (**2**). Both of them exhibit a very steep weight loss accompanied by an endothermic effect starting at 200 °C. The residual masses at 1000 °C are very low, 6.73 % for **1** and 4.49 % for **2**. There is virtually no difference, whether the TG/DSC analysis was performed under dry synthetic air or nitrogen atmosphere. The significantly lower residual masses than the ones calculated for conversion to SnO_2 further suggest high volatility. The complex **3**, however, exhibits a rather different behavior (Figure S3A–S3C), with a larger residual mass (17.03 %) and with several mass loss steps, the first one starting at 150 °C is associated with an endothermic effect, and during the second one at around 400 °C, exothermic effects occur. This different behavior of the complex **3** could be attributed to the sulfur heteroatom in the ligand, as it was observed in other complexes of sulfur-containing trifluoroacetonylazine ligands.[27]

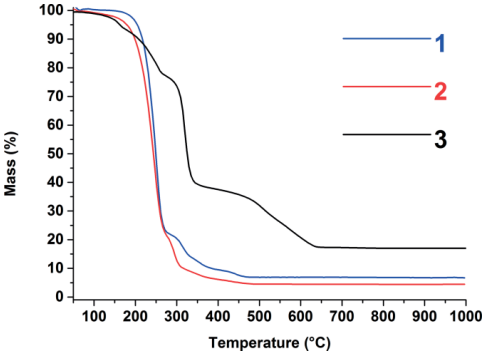

Figure 5. Comparison of TG curves of $Sn(OtBu)_2(PyTFP)_2$ (**1**), $Sn(OtBu)_2(DMOTFP)_2$ (**2**) and $Sn(OtBu)_2(BTTFP)_2$ (**3**).

The HT-XRD measurements have shown, that obtained complexes **1**–**3** maintain their crystallinity to 100–150 °C (Figure S4A). At temperatures of 150–300 °C, an unidentified crystalline phase with diffractions at 9° and 11°2θ was observed. Above 300 °C, the resulting solid is completely amorphous, and approximately at 600 °C, a slow, gradual crystallization of cassiterite SnO_2 (PDF 95–500–0225) starts (Figure S4B).

The reactions with representative fluorinated alcohols, 2,2,2-trifluoroethanol (TFEH) and 1,1,1,3,3,3-hexafluoro-2-propanol (HFPH), were investigated with the aim of substituting O*t*Bu groups and increasing volatility of the Sn^{IV} complexes. As it was expected that only O*t*Bu groups would undergo substitution, rather than the bidentate heteroarylalkenolate ligands, an excess of fluorinated alcohol of was used, in order to achieve full substitution of the O*t*Bu groups. Fluorinated alcohols are compounds with significantly acidic OH hydrogens ($pK_a \approx 12.4$ for TFEH and 9.3 for HFPH), and their reactions with **2** and **1** have led to complexes $Sn(TFE)_2(DMOTFP)_2$ (**4,** Figure 6) and $Sn(HFP)_2(PyTFP)_2$ (**5,** Figure 7) with O*t*Bu groups replaced with

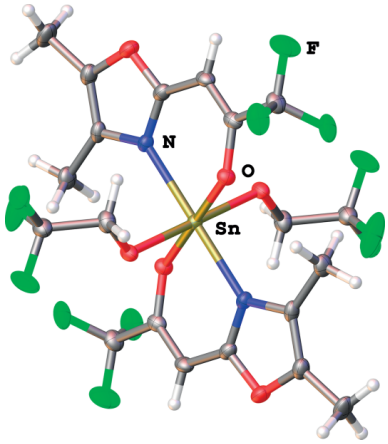

Figure 6. Molecular structures of $Sn(TFE)_2(DMOTFP)_2$ (**4**).

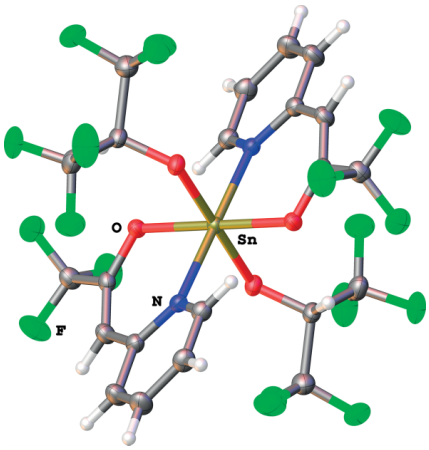

Figure 7. Molecular structures of $Sn(HFP)_2(DMOTFP)_2$ (**5**).

OCH_2CF_3 and $OCH(CF_3)_2$, respectively. The two chelating ligands retained their bonding to the Sn centers [Equation (2)].

$$Sn(OtBu)_2(N\cap O)_2 + 2\ R^FOH \rightarrow Sn(OR^F)_2(N\cap O)_2 + 2\ tBuOH \quad (2)$$

The reactions with non-fluorinated alcohols containing less acidic hydrogens, such as 1,4-butanediol or decan-1-ol, did not provide desired stoichiometric replacement of the O*t*Bu groups. No reaction was observed at ambient temperature while a mixture of products was obtained when heated.

The signals in the ^{19}F NMR spectra indicated the presence of CF_3 group as trifluoroalkoxo-tin species (from –75 to –76 ppm, compared with –73 to –74 ppm for CF_3 of the chelating ligand). The ^{119}Sn NMR spectra displayed high upfield shifts at around –700 ppm attributed to six-coordinate tin. Signals typical for O*t*Bu group attached to tin (at around 30 ppm for CH_3) were not found; therefore full exchange of the O*t*Bu groups for OR^F is suggested.

In the mass spectra, similarly to **1**–**3**, the fragments with high relative intensities possess intact Sn–N∩O ligand bonding, while the OR^F groups seem to undergo cleavage more easily.

The obtained TG/DSC curves, however, do not show any significant improvement of volatility and thermal properties (Figure S5A–S5C), despite increasing the number of volatility-improving CF_3 groups to four for $Sn(TFE)_2(DMOTFP)_2$ (**4**) and to six for $Sn(HFP)_2(PyTFP)_2$ (**5**). The residual masses also significantly increased, when compared to the parent compounds **2** and **1**, for the TFE derivative **4** to 14.67 % and for the HFP complex **5** to 21.06 %. An interesting point is, that the main weight loss at 300 °C is accompanied with exothermic effects, rather than endothermic, in contrast to the situation in $Sn(OtBu)_2(N\cap O)_2$. The implementation of fluorinated alkoxide groups into the complexes thus failed to improve their potential MOCVD properties.

According to the thermal behavior of complexes **1**–**5** revealed by the TG/DSC method, $Sn(OtBu)_2(PyTFP)_2$ (**1**) and $Sn(OtBu)_2(DMOTFP)_2$ (**2**) were chosen for further testing as MOCVD precursors. The MOCVD experiments were conducted at temperatures ranging from 350 to 900 °C. Thin films of SnO_2 were deposited on Sapphire-C substrates using low pressure PI-MOCVD. To compare the new precursors to already available ones, a typical commercially available diketonate-based MOCVD precursor di-*n*-butyltinbis(acetylacetonate) $Sn(Bu)_2(acac)_2$ and tin *tert*-butoxide $Sn(OtBu)_4$ (both from Strem Chemicals) were chosen. $Sn(Bu)_2(acac)_2$ solutions were stable in dimethoxyethane, whereas the $Sn(OtBu)_4$ precursor formed turbid solutions, not suitable for depositions. Even though the solvent was distilled from metallic sodium, the undesired hydrolysis reaction was most likely caused by residual moisture in the DME solvent. Considering the encountered problem with $Sn(OtBu)_4$, only the $Sn(Bu)_2(acac)_2$ precursor was finally selected. It was previously used as a successful Sn-precursor for the $CdSnO_3$ deposition.[36]

In MOCVD process, the thermal stability of precursors is an important factor determining the film growth rate at different temperatures. Figure 8 shows the SnO_2 growth rate (v, nm/min) as a function of the substrate temperature, presented as Arrhenius plots. Two regions might be visible in these graphs. At lower temperatures, the growth rate rapidly increases with temperature. In this kinetic region the film growth rate is mainly determined by thermally activated decomposition process of precursors at the substrate surface. At higher temperatures, the film growth rate becomes less dependent on temperature and is limited mainly by diffusion of precursor molecules to the substrate surface. The positions of the kinetic regions in the temperature scale show that the thermal stability of the new synthesized precursors **1** and **2** is higher, so the film growth requires higher temperatures than when using the commercial $Sn(Bu)_2(acac)_2$. A higher thermal stability of new precursors may be a useful property in the case of deposition of complex tin-containing perovskite materials (e.g. stannates), which usually require high deposition temperatures. Both new precursors showed rather comparable thermal behavior in the MOCVD process, with a slightly higher thermal stability for **1**.

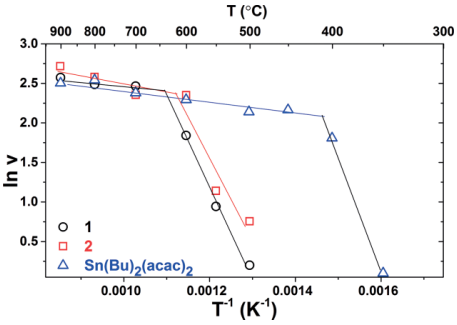

Figure 8. Dependences of the growth rate (v, nm/min) on the growth temperature, presented in the form of Arrhenius plots for $Sn(OtBu)_2(PyTFP)_2$ (**1**), $Sn(OtBu)_2(DMOTFP)_2$ (**2**), and $Sn(Bu)_2(acac)_2$.

The main properties of SnO_2 films deposited at different temperatures are presented in Table 1. Films grown from all three precursors in the temperature range 600–900 °C were well crystallized and contained (100) textured and in-plane oriented crystallites. This is demonstrated in Figure 9a taking as an example the films grown from **1**. Presented XRD patterns show clearly dominating (200) and (400) peaks of tetragonal SnO_2 phase. A shift of the peaks to the left may be visible when the growth temperature increases, which demonstrates the increase of the lattice a-parameter, which gradually approaches the value of the bulk stoichiometric SnO_2 (4.74 Å). A similar effect was observed in other reports,[37] where the authors explain it by either an increased strain relaxation of the films at higher deposition temperatures, or that films grown at lower temperatures are oxygen deficient. A good in-plane orientation of SnO_2 crystallites may be visible in XRD φ-scans for (101) reflection, presented in Figure 9b. Very similar XRD results were obtained for SnO_2 films, grown on sapphire-C substrates by pulsed laser deposition.[38] Full width at half maximum (FWHM) values of XRD rocking curves (ω-scans) for SnO_2 (200) reflection varied in the range of 0.15–0.4°, without any clear dependency on precursor and deposition temperature (Table 1). The films obtained from the new precursors exhibited slightly smaller FWHM

values of peaks in (101) φ-scans compared to the films from the commercial precursor. The films from **1** and **2** grown at 900 °C had the best in-plane orientation among deposited films, however the surface of all films grown at such high temperature was rough (AFM roughness average R_a > 10 nm, Table 1). The lowest surface roughness (R_a ≈ 2–3 nm) was measured for the films deposited from **1** and **2** at 700–800 °C.

Table 1. Properties of SnO_2 films grown at different temperatures.

Precursor	T °C	d[a] nm	GR nm/min	R_a, nm	a Å	ω deg	φ deg	E_g eV
1	600	151	6.4	3.3	4.682	0.176	4.72	4.06
	700	152	11.9	2.8	4.705	0.263	5.59	4.07
	800	172	11.7	2.5	4.730	0.342	6.85	4.07
	900	168	13.2	> 10	4.745	0.155	1.43	4.06
2	600	91	10.6	6.6	4.695	0.328	4.13	3.89
	700	152	10.6	2.2	4.696	0.202	5.60	4.10
	800	185	13.3	2.5	4.729	0.301	7.26	4.09
	900	238	15.3	> 10	4.745	0.225	1.3	3.73
$Sn(Bu)_2(acac)_2$	600	160	10.0	3.3	4.687	0.288	4.63	4.01
	700	166	10.9	4.7	4.715	0.242	6.71	4.04
	800	150	12.8	6.9	4.738	0.406	7.61	4.07
	900	244	12.4	> 10	4.737	0.272	4.88	4.08

[a] d = Film thickness, GR = growth rate, R_a = AFM average roughness, ω = FWHM SnO_2(200), φ = FWHM SnO_2(101).

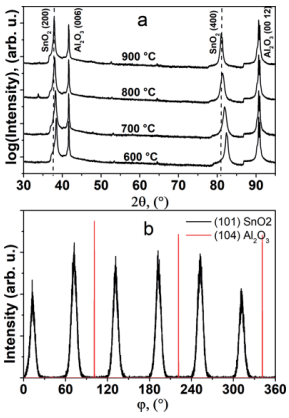

Figure 9. XRD data for SnO_2 films grown from **1**: a) $\theta/2\theta$ scans of films grown at different temperatures [dashed lines show positions of (200) and (400) peaks of bulk SnO_2, PDF Card 00–041–1445], b) φ-scans of SnO_2 (101) and Al_2O_3 (104) reflections, measured for SnO_2 films, grown at 800 °C.

The UV/Vis-IR spectroscopy measurements showed, that deposited layers are highly transparent (> 90 %) in the visible and mid-IR (up to λ = 5.5 μm) spectral ranges. After transformation of UV/Vis spectra into Tauc plots, they were used for the calculation of direct optical band gaps (E_g) of SnO_2 films, which varied in the range of 3.7–4.1 eV (Figure 10 and Table 1).

Crystalline SnO_2 films were directly sprayed on a hot sensor platform by using **1** at 800 °C for chemo-resistive gas sensing measurements (Figure 11). The sensing response of the n-type

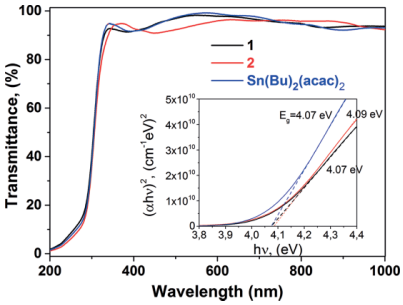

Figure 10. UV/Vis spectra for SnO_2 films grown from different precursors at 800 °C. Corresponding Tauc plots are presented in the inset.

semiconductor towards reducing (CO) or oxidizing (NO_2) gases was defined as the relative change in resistance of the deposited film, which is expressed in Equation (3).

$$\text{response (\%)} = \frac{R_{air} - R_{gas}}{R_{air}} \times 100 \quad (3)$$

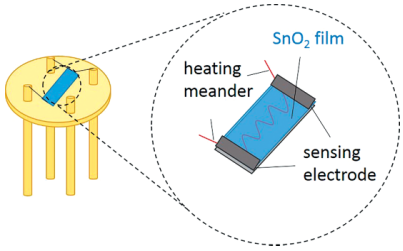

Figure 11. Scheme of the used sensor chip platform that consists of alumina substrate, is provided with Pt interdigitates electrical readout on the top side and a Pt-meander on the back side as a heating element, which were connected to Keithley source meters.

The change in resistance against different CO concentrations (25 to 150 ppm) in synthetic air and sensing temperatures (200 to 300 °C) were investigated. The measurements displayed the typical decrease in resistance upon CO exposure (Figure 12a), which reacts with the chemisorbed oxygen species on the SnO_2 surface.

The shift in the baselines can be attributed to the dissociated molecular O_2 to atomic O^{2-} species in the temperature range of 200–300 °C.[39] The response as a function of CO concentrations at 250 °C and 300 °C revealed the difference of the chemisorbed O^{2-} species (Figure 12b), due to the increased base resistance (119 kΩ at 200 °C, 135 kΩ at 250 °C and 157 kΩ at 300 °C) on one side and higher response at 300 °C (40 % at δ = 150 ppm) on the other side. These resulted from a higher amount of O^{2-} species at higher temperatures, which leads to an increase in number of charge captures from the semiconductor and thus to an increase of the resistance.[40] However, the fabricated chemo-resistive gas sensor revealed a response limit at 200 °C, due to the strong baseline drift and high signal-to-noise ratio. The sensor drift of the sample measured at 300 °C

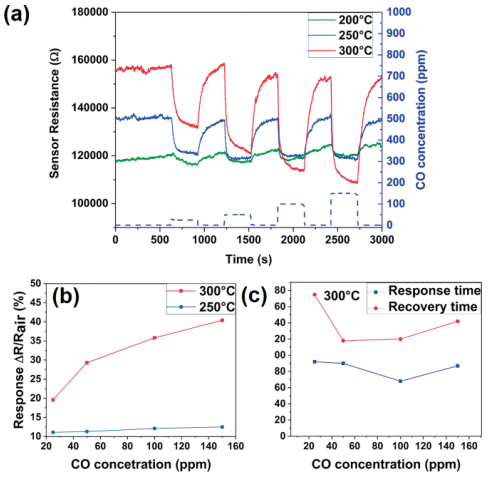

Figure 12. Response of SnO_2 thin films deposited at 800 °C towards different CO concentrations and temperatures as a function of concentration at different temperatures (a). Dependency of response (b) and response and recovery times t_{90} at 300 °C (c) on CO concentrations.

exhibits a decrease in resistance of 10 % of the initial resistance output after 24 h, possibly due to chemical and physical interaction processes of the chemical analytes at SnO_2 film, such as reorganization of the sensor surface or microstructure.[41]

The response and recovery times (t_{90}) have been defined as the time required to reach a 90 % variation in the resistance upon the introduction or removal of the target analyte gas. The response and recovery times are displayed as a function of CO concentrations and are in a similar range of SnO_2 thin films (Figure 12c).

The response to the oxidizing gas NO_2 at 250 °C and 300 °C shows the typically increase of the resistance of n-type semiconductor SnO_2. There was no significant change of the response to varying temperatures (Figure 13). The sensor signal

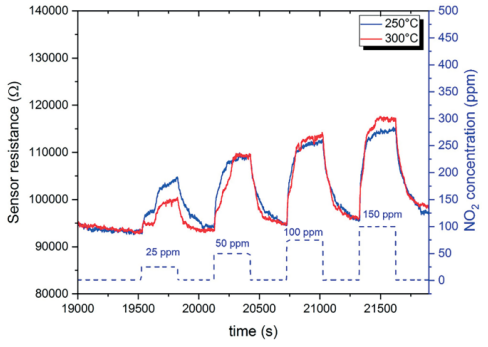

Figure 13. Response of SnO_2 thin films deposited at 800 °C towards different NO_2 concentrations and temperatures.

of the 25 ppm NO_2 pulse exhibits a "weird"deformed shape, due to a measuring artefact during dilution of the analyte gas with dry synthetic air.

Conclusions

We have obtained three novel complexes with the $Sn(OtBu)_2(N\cap O)_2$ ($N\cap O$ = PyTFP, DMOTFP, BTTFP) structural motive containing octahedrally coordinated Sn^{IV}. These compounds are according to HT-XRD and TG/DSC analyses suitable precursors for further processing to SnO_2. We have also investigated reactivity of the O*t*Bu groups with reagents containing OH groups. The reactions with alcohols containing strongly acidic hydrogen, such as CF_3CH_2OH and $(CF_3)_2CHOH$, led by alkoxide exchange to well defined structures with both O*t*Bu groups completely replaced with fluoroalkoxides. We have also successfully tested two of the complexes, $Sn(OtBu)_2(PyTFP)_2$ (**1**) and $Sn(OtBu)_2(DMOTFP)_2$ (**2**), as MOCVD precursors for the preparation of thin SnO_2 films. Films deposited on sapphire-C substrates exhibited high crystalline quality, good surface smoothness and transparency in the whole VIS region as well as in NIR up to 5500 cm^{-1}, what demonstrate the suitability of such precursors for MOCVD depositions. Film growth rate dependencies on temperature showed a rather high thermal stability of the new precursors. So, the new compounds may be attractive precursors for deposition of mixed perovskite oxides usually requiring higher deposition temperatures. The in-plane oriented films showed good response to CO and NO_2 gases in chemo-resistive gas sensing measurements.

Experimental Section

General Procedures: The $Sn(OtBu)_4$ was synthesized from $SnCl_4$ (Carlo Erba) after Hampden-Smith et al.[42] The TFEH and HFPH were dried with Na wire, distilled, and stored under N_2 atmosphere. The PyTFPH, DMOTFPH, and BTTFPH ligands were prepared after Kawase et al.[25] and vacuum dried for 24 h prior to reactions. Solvents were dried with conventional methods using solvent purification system (MBraun SPS-800). All reactions were carried out under N_2 atmosphere using Schlenk techniques or in an M. Braun dry box with both H_2O and O_2 levels below 1 ppm.

CVD Experiments: Pulsed injection MOCVD depositions were carried out in a low-pressure hot-wall reactor equipped with a pulsed liquid injection system. A metal-organic precursor was dissolved in DME (c = 0.01 mol L^{-1}) and precise micro-doses (several µL) of the solution were sequentially injected by a special computer-controlled electromagnetic injector into a hot (200 °C) evaporation zone, where flash evaporation of micro-doses occurred under vacuum. The formed mixture of precursor and solvent vapors was carried into the deposition zone with a Ar/O_2 (4:1) gas mixture. Injection frequency was 2 Hz. Depositions were performed on sapphire-C substrates at 10 Torr pressure, in the temperature range of 350–900 °C.

Sensor Characterization

The chemo-resistive gas response experiments were carried out with a customized gas sensing system. The set-up consists of four electronic mass-flow controllers (Aero), a sensor chamber, a sensor chip platform and two Keithley source meters for heating and meas-

uring the change of electrical resistance of the SnO_2 thin films. Electrical measurements and flowing gas concentrations were controlled using self-developed LabView software.

The atmosphere composition was preassigned by means of electronic mass-flow controllers, mixing flows coming from certified bottles containing a given amount of the target gas diluted in dry synthetic air as the background flow. For all the gas measurements, a constant flow of 1000 sccm was kept. The sensing material was characterized towards carbon monoxide (CO) and nitrogen dioxide (NO_2) at different concentrations (25 to 150 ppm) and temperatures (200 to 300 °C).

Characterization Methods and Analytical Data: See Supporting Information for details.

Synthesis of Sn(O*t*Bu)$_2$(PyTFP)$_2$ (1): Sn(O*t*Bu)$_4$ was weighted and dissolved in a selected solvent. Into this solution, PyTFPH was added. For particular reaction parameters see Table S3. The mixture was stirred at room temperature for 2 h, then the solvent and volatiles were removed under vacuum (10^{-3} mbar, 25 °C). In all cases, yellow solids were obtained. Vacuum sublimation was carried out at 140–150 °C. Yield (PyTFP9, Table S3): 2.889 g; 91.3 %. Colorless single crystals of **1** were obtained by crystallization at –28 °C from THF.

Synthesis of Sn(O*t*Bu)$_2$(DMOTFP)$_2$ (2): Sn(O*t*Bu)$_4$ (3.03 mmol; 1.247 g) was dissolved in 10 cm^3 of toluene. Into this solution DMOTFPH (6.06 mmol; 1.256 g) was added. The mixture was left stirring at room temperature for 2 h, then solvent and volatiles were removed via distillation under reduced pressure (10^{-3} mbar, 25 °C). A white solid was obtained, yield 1.865 g; 90.7 %. The obtained solid was recrystallized at room temperature from 0.5 cm^3 of THF. Solid colorless crystals of **2** were obtained.

Synthesis of Sn(O*t*Bu)$_2$(BTTFP)$_2$ (3): Sn(O*t*Bu)$_4$ (1.48 mmol; 0.610 g) was dissolved in 10 cm^3 of toluene. Into this solution, BTTFPH (2.97 mmol; 0.727 g) in 10 cm^3 of THF (suspension, poorly soluble) was added. The mixture was left stirring at room temperature for 24 h, then solvent and volatiles were removed via distillation under reduced pressure (10^{-3} mbar, 25 °C). A beige solid was obtained, yield 1.062 g; 95.3 %. Obtained solid was sublimed at 150 °C. White crystals of **3** were obtained.

Synthesis of Sn(TFE)$_2$(DMOTFP)$_2$ (4): Sn(O*t*Bu)$_2$(DMOTFP)$_2$ (0.422 g, 0.62 mmol) was dissolved in 10 cm^3 of toluene. Into this solution, TFE (0.14 cm^3, 1.86 mmol) was added. The mixture was left stirring at room temperature for 24 h, then solvent and volatiles were removed via distillation under reduced pressure (10^{-3} mbar, 25 °C). Obtained white solid (yield: 0.390 g; 85.9 %) was dissolved in 0.5 cm^3 of THF and crystallized at –20 °C.

Synthesis of Sn(HFP)$_2$(PyTFP)$_2$ (5): Sn(O*t*Bu)$_2$(PyTFP)$_2$ (0.297 g, 0.46 mmol) was dissolved in 10 cm^3 of toluene. Into this solution, HFPH (0.15 cm^3, 1.42 mmol) was added. The mixture was left stirring at room temperature for 24 h, then solvent and volatiles were removed via distillation under reduced pressure (10^{-3} mbar, 25 °C). Yield: 0.313 g; 82.1 %. Obtained white solid was dissolved in 0.5 cm^3 of THF and crystallized at –20 °C.

CCDC 1866886 (for **1**), 1854639 (for **2**), 1866887 (for **3**), 1866888 (for **4**), and 1866889 (for **5**) contain the supplementary crystallographic data for this paper. These data can be obtained free of charge from The Cambridge Crystallographic Data Centre.

Acknowledgments

The results of this research have been acquired with the financial contribution made by the MEYS CR within the National Program for Sustainability II project CEITEC 2020 (LQ1601). Funded by MEYS CR of the CIISB research infrastructure project LM2015043 is gratefully acknowledged for the financial support of the measurements at the CF X-ray Diffraction and Bio-SAXS and the Josef Dadok National NMR Centre. The authors thank Dr. P. Bezdicka for HT-XRD data, Dr. A. Styskalik and P. Machac for MS measurements.

Keywords: Chemical vapor deposition · Fluorinated ligands · Sensors · Thin films · Tin dioxide

[1] C. Kilic, A. Zunger, *Phys. Rev. Lett.* **2002**, *88*, 095501.
[2] M. Batzill, U. Diebold, *Prog. Surf. Sci.* **2005**, *79*, 47.
[3] a) H. Zhang, G. Chen, D. W. Bahnemann, *J. Mater. Chem.* **2009**, *19*, 5089; b) M. T. Uddin, Y. Nicolas, C. Olivier, T. Toupance, L. Servant, M. M. Müller, H. J. Kleebe, J. Ziegler, W. Jaegermann, *Inorg. Chem.* **2012**, *51*, 7764; c) S. Zhang, X. Xu, B. Feng, J. Hu, Y. Pang, G. Zhou, L. Tong, Y. Zhou, *ACS Appl. Mater. Interfaces* **2014**, *6*, 613.
[4] a) S. Gubbala, V. Chakrapani, V. Kumar, M. K. Sunkara, *Adv. Funct. Mater.* **2008**, *18*, 2411; b) P. Tiwana, P. Docampo, M. B. Johnston, H. J. Snaith, L. M. Herz, *ACS Nano* **2011**, *5*, 5158; c) I. Concina, A. Vomiero, *Small* **2015**, *11*, 1744.
[5] a) T. Brousse, R. Retoux, U. Herterich, D. M. Schleich, *J. Electrochem. Soc.* **1998**, *145*, 1; b) Z. Wei, Q. Wang, Q. Zhiang, J. Li, *Adv. Funct. Mater.* **2007**, *17*, 2772; c) M. S. Park, G. X. Wang, Y. M. Kang, D. Wexler, S. X. Dou, H. K. Liu, *Angew. Chem. Int. Ed.* **2007**, *46*, 750–767; *Angew. Chem.* **2007**, *119*, 764.
[6] a) N. Barsan, U. Weimar, *J. Electroceram.* **2001**, *7*, 143; b) A. Kolmakov, Y. Zhang, G. Cheng, M. Moskovits, *Adv. Mater.* **2003**, *15*, 997; c) T. Hübert, L. Boon-Brett, G. Black, U. Banach, *Sensors Actuat. B* **2011**, *157*, 329; d) K. Wetchakun, T. Samerjai, N. Tamaekong, C. Liewhiran, C. Siriwon, V. Kruefu, A. Wisitsoraat, A. Tuantranont, S. Phanichphant, *Sensors Actuat. B* **2011**, *160*, 580; e) L. Wang, Y. Wang, K. Yu, S. Wang, Y. Zhang, C. Wei, *Sensors Actuat. B* **2016**, *232*, 91.
[7] H. Remy, *Lehrbuch der Anorganischen Chemie*, Geest & Portig, Leipzig, **1957**, pp. 629.
[8] a) S. Raghunath Reddy, A. K. Mallik, S. R. Jawalekar, *Bull. Mater. Sci.* **1986**, 357; b) O. T. Inal, M. Bengisu, J. Guardian, *J. Mater. Sci.* **1993**, *28*, 1155; c) L. S. Parshina, O. A. Novodvorsky, O. D. Khramova, I. A. Petukhov, V. A. Mikhalevsky, A. A. Lotin, E. A. Cherebilo, V. Ya. Panchenko, *Opt. Quantum Electron.* **2016**, *48*, 316.
[9] X. Xiang, D. Zhu, D. Wang, *J. Mater. Sci. Mater. Electron.* **2016**, *27*, 7425.
[10] A. Cirera, A. Vila, A. Cornet, J. R. Morante, *Mater. Sci. Eng. C* **2001**, *15*, 203.
[11] W. Lada, A. Deptula, T. Olczak, W. Torbicz, D. Pijanowska, A. Di Bartolomeo, *J. Sol-Gel Sci. Technol.* **1994**, *2*, 551.
[12] A. Aboulaich, B. Boury, P. H. Mutin, *Eur. J. Inorg. Chem.* **2011**, *2011*, 3644.
[13] J. P. Senateur, C. Dubourdieu, F. Weiss, M. Rosina, A. Abrutis, *Adv. Mater. Opt. Electron.* **2000**, *10*, 155.
[14] a) Y. Rozier, B. Gautier, G. Hyvert, A. Descamps, C. Plossu, C. Dubourdieu, F. Duceoquet, *Thin Solid Films* **2009**, *517*, 1868; b) A. Abrutis, V. Plausinaitiene, V. Kubilius, A. Teiserskis, Z. Saltyte, R. Butkute, J. P. Senateur, *Thin Solid Films* **2002**, *413*, 32; c) A. Bartasyte, V. Plausinaitiene, A. Abrutis, T. Murauskas, P. Boulet, S. Margueron, J. Gleize, S. Robert, V. Kubilius, Z. Saltyte, *Appl. Phys. Lett.* **2012**, *101*, 122902.
[15] L. G. Hubert-Pfalzgraf, *Appl. Organomet. Chem.* **1992**, *6*, 627.
[16] M. Tiitta, L. Niinisto, *Chem. Vapor. Depos.* **1997**, *3*, 167.
[17] J. C. Reid, M. Calvin, *J. Am. Chem. Soc.* **1950**, *72*, 2948.
[18] J. F. Carpentier, *Dalton Trans.* **2010**, *39*, 37.
[19] C. Campbell, S. G. Bott, R. Larsen, W. G. Van der Sluys, *Inorg. Chem.* **1994**, *33*, 4950.
[20] S. Mishra, S. Daniele, *Chem. Rev.* **2015**, *115*, 8379.
[21] a) J. A. Samuels, E. B. Lobkovsky, W. E. Streib, K. Folting, J. C. Huffman, J. W. Zwanziger, K. G. Caulton, *J. Am. Chem. Soc.* **1993**, *115*, 5093; b) J. A. Samuels, W. C. Chiang, C. P. Yu, E. Apen, D. C. Smith, D. V. Baxter, K. G. Caulton, *Chem. Mater.* **1994**, *6*, 1684.

[22] L. Miinea, S. Suh, S. G. Bott, J. R. Liu, W. K. Chu, D. M. Hoffman, *J. Mater. Chem.* **1999**, *9*, 929.
[23] M. Valet, D. M. Hoffman, *Chem. Mater.* **2001**, *13*, 2135.
[24] K. C. Molloy, J. E. Stanley, *Appl. Organomet. Chem.* **2009**, *23*, 62.
[25] M. Kawase, M. Teshima, S. Saito, S. Tani, *Heterocycles* **1998**, *48*, 2103.
[26] L. Bruckmann, W. Tyrra, S. Stucky, S. Mathur, *Inorg. Chem.* **2012**, *51*, 536.
[27] L. Appel, R. Fiz, W. Tyrra, S. Mathur, *Dalton Trans.* **2012**, *41*, 1981.
[28] L. Appel, J. Leduc, C. L. Webster, J. W. Ziller, W. J. Evans, S. Mathur, *Angew. Chem. Int. Ed.* **2015**, *54*, 2209–2241; *Angew. Chem.* **2015**, *127*, 2237.
[29] G. Fornalczyk, M. Valldor, S. Mathur, *Cryst. Growth Des.* **2014**, *14*, 1811.
[30] M. Büyükyazi, C. Hegemann, T. Lehnen, W. Tyrra, S. Mathur, *Inorg. Chem.* **2014**, *53*, 10928.
[31] a) I. Giebelhaus, R. Muller, W. Tyrra, I. Pantenburg, T. Fischer, S. Mathur, *Inorg. Chim. Acta* **2011**, *372*, 340; b) T. Heidemann, S. Mathur, *Eur. J. Inorg. Chem.* **2014**, *2014*, 506.
[32] D. C. Bradley, R. C. Mehrotra, W. Wardlaw, *J. Chem. Soc.* **1952**, 2027.
[33] M. J. Hampden-Smith, T. A. Wark, C. J. Brinker, *Coord. Chem. Rev.* **1992**, *112*, 81.
[34] M. North, *Principles and Applications of Stereochemistry*, CRC Press, Cheltenham, **1998**, p. 61.
[35] a) R. M. Secor, *Chem. Rev.* **1963**, *63*, 297; b) R. A. Foster, C. G. Laspe, *US2662879A Patent* **1953**.
[36] A. Abrutis, G. Valincius, G. Baltrunas, L. Parafionovic, A. Valiuniene, Z. Saltyte, *Thin Solid Films* **2007**, *515*, 6817.
[37] a) J. Sundqvist, M. Ottosson, A. Harsta, *Chem. Vap. Deposition* **2004**, *10*, 77; b) Z. Zhu, J. Ma, C. Luan, L. Kong, Q. Yu, *J. Lumin.* **2011**, *131*, 88.
[38] L. C. Tien, D. P. Norton, J. D. Budai, *Mater. Res. Bull.* **2009**, *44*, 6.
[39] a) A. Gurlo, *ChemPhysChem* **2006**, *7*, 2041; b) N. Yamazoe, J. Fuchigami, M. Kishikawa, T. Seiyama, *Surf. Sci.* **1979**, *86*, 335.
[40] a) D. Degler, S. Wicker, U. Weimar, N. Barsan, *J. Phys. Chem. C* **2015**, *119*, 11792; b) N. Barsan, M. Schweizer-Berberich, W. Göpel, *Fresenius J. Anal. Chem.* **1999**, *365*, 287.
[41] A. Vergara, S. Vembu, T. Ayhan, M. A. Ryan, M. L. Homer, R. Huerta, *Sens. Actuators B* **2012**, *166*, 320.
[42] M. J. Hampden-Smith, T. A. Wark, A. Rheingold, J. C. Huffman, *Can. J. Chem.* **1991**, *69*, 121.

Received: July 23, 2018

2

Metalorganic chemical vapor deposition and investigation of nonstoichiometry of undoped $BaSnO_3$ and La-doped $BaSnO_3$ thin films

T. Murauskas, V. Kubilius, Z. Saltyte, V. Plausinaitiene

Thin Solid Films 692 (2019) 137575

Contents lists available at ScienceDirect

Thin Solid Films

journal homepage: www.elsevier.com/locate/tsf

Metalorganic chemical vapor deposition and investigation of nonstoichiometry of undoped $BaSnO_3$ and La-doped $BaSnO_3$ thin films

Tomas Murauskas, Virgaudas Kubilius, Zita Saltyte, Valentina Plausinaitiene*

Institute of Chemistry, Faculty of Chemistry and Geosciences, Vilnius University, LT- 03225 Vilnius, Lithuania

ARTICLE INFO

Keywords:
Metalorganic chemical vapor deposition
Perovskite
Lanthanum doped barium stannate
Stoichiometric composition
Optoelectronic

ABSTRACT

Wide bandgap (~3 eV) perovskite transparent conductive oxide material exhibiting superior electric properties is highly desired in today's optoelectronics. Just recently La-doped barium stannate (LBSO) bulk n-type semiconductor with outstanding carrier mobility (~320 $cm^2\ V^{-1}\ s^{-1}$) at high carrier density ($10^{20}\ cm^{-3}$) has been discovered. Highly conductive thin LBSO film synthesis has been challenging due to large lattice mismatch and nonstoichiometry as being the least investigated. Therefore, in this work, the Pulsed injection metalorganic chemical vapor deposition method was used for the growth of undoped $BaSnO_3$ (BSO) and La-doped $BaSnO_3$ thin films. Film depositions were carried out on monocrystalline $LaAlO_3$, $SrTiO_3$, Al_2O_3 substrates in wide stoichiometric range. Deviation from stoichiometric composition in BSO (Sn/Ba) and LBSO (Sn/(Ba + La)) had a significant impact on microstructure, optical, and electric properties while maintaining cubic symmetry. Near-stoichiometric films even grown at a high rate of ~10 nm/min showed sufficient electric properties.

1. Introduction

Wide bandgap perovskite oxide materials ABO_3 (A = Ba, Sr, Ca; B = Sn), doped in A or B positions, have drawn interest as perspective n-type transparent conductive materials (TCO) [1, 2]. Recent reports of high room-temperature (r.t.) mobility in bulk La-doped single-crystal $BaSnO_3$ (LBSO) have resulted in significant interest in doped perovskite barium stannate (BSO) as a high-performance transparent conductor. Mobility values of 320 $cm^2\ V^{-1}\ s^{-1}$ at a carrier density of $8 \times 10^{19}\ cm^{-3}$ were reported, surpassing the long-standing perovskite limits of Nb:$SrTiO_3$ 32 $cm^2\ V^{-1}\ s^{-1}$ at $7.9 \times 10^{17}\ cm^{-3}$ [3]. Exceptional conductive properties, outstanding r.t. carrier mobility and superior thermal stability make doped BSO a potential key material for the use in oxide electronics [4]. Similar structural properties and similar bandgap offset allows the BSO use in heterostructures with other perovskite oxides ($SrTiO_3$, $LaAlO_3$, $LaInO_3$) [5], giving access to rich physics and functionality exhibited by the perovskites [6] and offering the possibility of forming various all-perovskite oxide-based devices [7]

However, obtaining high room mobility in thin films at r.t. remains a challenge. So far obtained films have demonstrated significantly lower mobilities compared to bulk BSO. Undoped and doped BSO films have been deposited using magnetron sputtering [8, 9], pulsed laser deposition (PLD) [10], and molecular beam epitaxy (MBE) [11, 12] methods. The best results in terms of mobility were obtained by MBE. Highest mobility values were demonstrated by Paik et al. achieving the highest mobility of 183 $cm^2\ V^{-1}\ s^{-1}$ in MBE grown LBSO films on $DySnO_3$ [13]. High mobilities of 150 $cm^2\ V^{-1}\ s^{-1}$ and 100 $cm^2\ V^{-1}\ s^{-1}$ were also achieved by Raghavan et al. on $PrScO_3$ and $SrTiO_3$, respectively.

The reduced mobilities in LBSO films have been primarily attributed to the substrate-induced misfit/threading dislocations in films [14] acting as charge carrier scattering centers at the grain boundaries. In addition, point defects formed due to deviation from stoichiometry (Sn/(Ba + La) = 1) in LBSO films are responsible for worse electrical properties. Deviations from stoichiometry results in a significant reduction in the concentration and mobility of *n*-type carriers due to formed compensating point defects in this material [12,15]. La_{Ba} donors can be compensated by acceptor-type native point defects, such as Ba or Sn vacancies, or by anti-site defects La_{Sn} as self-compensation acceptors. Thus, the possibility to control composition, the concentration of non-stoichiometric compensating acceptor-type point defects, and the density of threading dislocations would possibly contribute to producing high mobility and conductivity LBSO films. La_{Sn} anti-site defect negative contribution, on the other hand, could theoretically be suppressed in cation-rich and oxygen-poor conditions in La–Ba–Sn–O system as shown in theoretical calculations by Weston et al. [15]. Also, control of factors, such as substrate structure, deposition conditions contributing to film microstructure and stoichiometry would result in

* Corresponding author.
E-mail addresses: tomas.murauskas@chf.vu.lt (T. Murauskas), virgaudas.kubilius@chf.vu.lt (V. Kubilius), vale.plausinaitiene@gmail.com (V. Plausinaitiene).

https://doi.org/10.1016/j.tsf.2019.137575
Received 20 June 2019; Received in revised form 13 September 2019; Accepted 13 September 2019
Available online 16 October 2019

better electrical properties as well. Using optimized deposition process LBSO films with excellent electrical properties were obtained by MBE and PLD methods. Although, the reproducibility of the results is not high – films grown by the same technique showed large variation in electrical properties, especially in mobility. This might be related to difficulties in controlling the precise stoichiometry of LBSO films in these techniques. In addition, little to no results are reported regarding a wide range of stoichiometry in BSO or LBSO films.

In the actual work, the possibility to grow high-quality BSO and LBSO films by metal-organic chemical vapor deposition (MOCVD) technique is investigated. Chemical vapor deposition (CVD) methods are more versatile in the control of the film composition. However, the possibilities of depositing BSO or LBSO films by CVD methods have not been studied. For the film deposition, low-pressure pulsed injection liquid CVD modification (PI-MOCVD) was used. This method was applied for the growth of various functional oxide materials, including perovskites [16,17]. PI-MOCVD, based on flash evaporation principle, precise precursor dosing into the reactor, provides easier control of thin film composition. These features are of high importance, taking into account the importance of stoichiometry control in BSO and LBSO films. In this work, deposition conditions for epitaxial BSO and LBSO films were established. The influence of deviation from stoichiometry on microstructure, morphology, optical and electrical properties was studied in a wide range of compositions.

2. Experimental details

Undoped barium stannate films were deposited using $Sn(thd)_2$, $Ba(thd)_2$ (stabilized with triglyme adduct) precursors. Whereas, additional $La(thd)_3$ precursor (thd = 2,2,6,6-tetramethyl-3,5-heptanedionate) was selected for La-doped thin film synthesis. Precursor solutions were prepared in dimethoxyethane solvent maintaining a concentration of 0.02 M. For the MOCVD process, Argon (Ar) and oxygen (O_2) gasses were supplied, maintaining a total pressure in the reactor chamber at 13 kPa. Undoped and 2.5 ± 0.2%$_{atomic}$ La-doped films of approximately 160–175 nm were grown at a rate of 10 nm/min on crystalline $LaAlO_3$ (100), $SrTiO_3$ (100), Al_2O_3 (0006) substrates – LAO, STO, Al_2O_3, respectively. Deposition time varied from 16 to 17 min. Morphology was investigated using Hitachi SU 70 Analytical scanning electron microscope (SEM) operating at 10 kV. Elemental composition was investigated using Hitachi TM3000 SEM coupled with X-ray energy dispersion spectrometer (EDS). EDS spectra were collected using accelerating voltage of 15 kV and accumulation time of 5 min. Structural high-resolution transmission electron microscopy (TEM) measurements of films formed on STO substrates were carried out by FEI Tecnai G2 F20 X-TWIN TEM operating at 200 kV. FEI Helios Nanolab 650 dual beam microscope equipped with an Omniprobe manipulator was used to prepare the cross-sectional TEM specimens. TEM lamella thickness was determined to be 60 nm by using convergent beam electron diffraction pattern analysis. Surface roughness was measured using Veeco Nanoscope II atomic force microscope. The thickness of deposited films was determined using the Taylor−Hobson profilometer. Crystalline structure was studied using Rigaku MiniFlex II tabletop X-ray diffractometer recording $\theta/2\theta$ diffractograms in Bragg–Brentano measuring geometry. While pole figures and $\theta/2\theta$ diffractograms of polycrystalline sample analysis in θ–θ, and grazing incidence geometries ($\alpha = = 0.45^{\circ}$) was carried out using Bruker D8 Advance diffractometer equipped with parallel beam monochromatizing optics. Both diffractometers operated with copper anode X-ray source (CuKα) and linear (1D) detector. Optical UV–vis spectrophotometry measurements were recorded in transmission mode measuring films on Al_2O_3. Tauc's plots were used to determine band gap (E_g) by extrapolating the absorption edge. The well-established Van der Pauw four-probe method and Hall measurements in a magnetic field of 0.6 T were also employed to investigate resistance, carrier concentration, and density temperature.

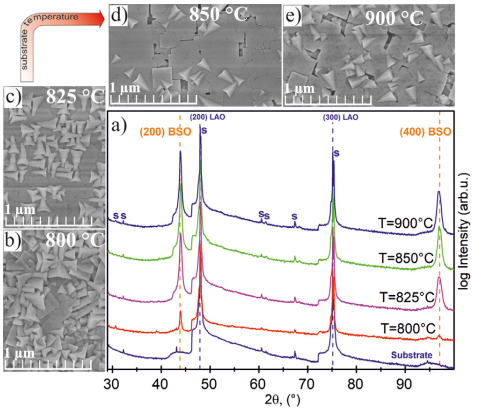

Fig. 1. (a) Xray diffraction patterns of BaSnO3 thin films deposited on LAO. Substrate temperature: 800 °C, 825 °C, 850 °C, and 900 °C. Dashed lines: BSO reflection angles, Powder diffraction file card no.: 00-042-1468; dotted lines represent the scattering pattern of LAO substrate. SEM micrographs of thin films deposited at (b) 800 °C, (c) 825 °C, (d) 850 °C, (e) 900 °C.

3. Results and discussion

3.1. Undoped $BaSnO_3$: deposition temperature

MOCVD methods are based on precursor vapor phase chemical reaction and rely on chemical species mass transport, adsorption and diffusion processes which are highly dependent on reaction conditions. Efficient mass transport was ensured using thermally stable and volatile (thd)-based precursors (used in our previous works [18,19]). Selecting the right deposition temperature during the initial experiments was also a key factor for BSO deposition. Similar substrate temperatures used in physical synthesis methods were applied (800, 825, 850, 900 °C) (Fig. 1) [13,20]. The tin and barium ratio of the solution was adjusted to achieve a near-stoichiometric ratio of the films (Sn/Ba ~ 1.00). X-ray diffraction (XRD) measurements (Fig. 1a) revealed that films deposited using 800 °C were of poor crystalline quality. In comparison, (l00) oriented pure phase BSO films were obtained at 825 °C and higher, respectively. The lattice parameter of 0.4118 ± 0.0006 nm well corresponded with reported values [21]. While XRD measurements showed similar results, SEM micrographs revealed significant morphological changes. Depositions at 825 °C resulted in a vast amount of defects, possibly different crystal orientations and chaotic morphology. In comparison, films deposited at temperatures of 850 °C and 900 °C were composed of cubic compact crystallites with protruding characteristic pyramid-shaped inclusions, suggesting the formation of textured BSO films. These results show that thin film formation is limited by BSO formation temperature rather than precursor decomposition temperature or diffusion. For further experiments, the most feasible temperature of 850 °C was chosen.

3.2. Undoped $BaSnO_3$: Sn/Ba stoichiometry influence on film phase composition

$BaSnO_3$ films are widely discussed in terms of crystalline quality, defects, doping effects, and conductance. Although attention to films in wide compositional range and its effects is discussed moderately [12]. This can be explained by the fact that tuning of the film composition requires the change of the target in physical methods. Therefore, stoichiometric targets are usually considered the most suitable option. In

respect, the liquid injection PI-MOCVD method offered a possibility to tune the film composition easily and consequently the physical/structural properties of deposited films. The primary aim of this work was to investigate the effects of wide range nonstoichiometry on film properties. Therefore, the Sn/Ba ratio in the solution was adjusted from 0.3 to 0.7, resulting in film composition with nonstoichiometric Sn/Ba ratios of 0.54 to 1.3. In attempts to further optimize the deposition process and investigate various properties affected by layer composition, films with different Sn/Ba ratio were deposited on STO, LAO, and Al_2O_3 substrates. Parameters that could influence the results, such as gas flow rate, substrate temperature, solution injection rate, precursor net concentration, and reaction chamber pressure were fixed.

XRD thin film crystal structure analysis was carried out by in Bragg–Brentano measuring geometry. Ba-poor layer composition was primarily dominated by the formation of cubic $BaSnO_3$ phase followed by residual tetragonal SnO_2 phase. Such result was well expected as additional Sn precursor was not incorporated in the formation of ternary phase.

Deposited near-stoichiometric BSO (Sn/Ba = 1.01) films were of single-phase and a-axis textured on STO and LAO substrates. Texture analysis revealed that films on either substrate were epitaxial. Polycrystalline film orientation was observed on Al_2O_3 substrate. XRD measurements of Ba-rich films showed textured (l00) orientation of the BSO films and broadening of (l00) diffraction peaks. Additionally, increasing the Ba content resulted in characteristic satellite peaks observed as Sn/Ba ratio was lower than 0.97 limit. Such peak splitting and broadening were consistent with two structural factors (Fig. 2 a):

a) Ruddlesden–Popper (RP) stacking faults are rather known to form in thin BSO films. This has been demonstrated in LBSO films deposited by PLD [23] and MBE [13] methods. RP faults are explained by periodic insertion of (BaO) periodic layers in the $BaSnO_3$ lattice on {100} planes with translational displacements of $1/2a < 111 >$ [24]. Films with extended RP defects are described by $Ba_{n+1}Sn_nO_{3n+1}$ composition where $2 > n > 1$ [13,25,26]. In the case of Sn/Ba < 1 composition, Ba_2SnO_4 (a = 4.1411 Å) phase formation is theoretically possible, increasing the lattice parameter corresponding to satellite (l00) peak [27]. Although, the theoretical increase of lattice parameter is lower than determined values (a > 4.14 Å) (Fig. 2b). This suggested that resulting satellite peaks were not caused solely due to the RP phase.

b) Substrate-film lattice mismatch at room temperature extends to ~5% and ~8% for STO/BSO and LAO/BSO, respectfully. High lattice mismatch in textured films is known to induce not only dislocations but can be responsible for residual strain as well. A detailed XRD study of similar perovskite $LaSrMnO_3$ thin films on STO substrates proposed a relevant in-plane strain relaxation model. It has been demonstrated that with the evolution of film thickness from 10 to 110 nm, periodic twin domains tilted by a slight angle with respect to surface normal are formed. Such relaxation of strain resulted in X-ray satellite reflections more distinguishable in films of higher thickness [28]. Also, peak splitting in strained perovskite films could originate from two different lattice structure along the growth direction – the strained layer near the substrate surface and relaxed above this strained layer [29]. Likewise, a study of perovskite $LaNiO_3$ thin films of 560 nm on LAO substrate reported a similar strain relaxation behavior. Reported a and c lattice parameters were dependent on substrate-lattice mismatch as well as the oxygen content in the films [30]. Higher lattice mismatch produced lower peak separation. Similar results were obtained in this study. Peak separation decreased with the larger lattice mismatch, and in the case of Al_2O_3, no separation was observed. The determined a parameter increase in Ba-rich samples could also be related to oxygen vacancy formation. Oxygen vacancy (intrinsic defect) has low formation energy compared to possible Ba^{2+}, Sn^{4+} vacancies [31]. It should be noted that this behavior is consistent with that of V_O in other wide bandgap n-type TCOs, i.e., ZnO [32–34] SnO_2 [35], Ga_2O_3 [36], and In_2O_3 [37]. Oxygen vacancy formation has been demonstrated as a possible cause of lattice parameter increase in BSO as well as other types of perovskites [38].

In order to check the phase purity of the films on STO and LAO, X-ray pole figures of the (110) and (200) reflections were measured using Schultz geometry (θ–θ) configuration (Fig. 3). Near-stoichiometric (Sn/Ba = 1.02) and Ba-rich (Sn/Ba = 0.81) samples were selected. Well-aligned thin BSO films were achieved in near stoichiometric composition corresponding to the full width at half maxima values of 0.3° and 0.8° measuring ω-scan (rocking curve) and φ-scan, respectfully. In comparison, an increase in barium resulted in the disorientation of crystallites with respective values of 1.0° and 1.5°. Epitaxial relationship of BSO(100)||STO(100) and BSO(100)||LAO(100), for both

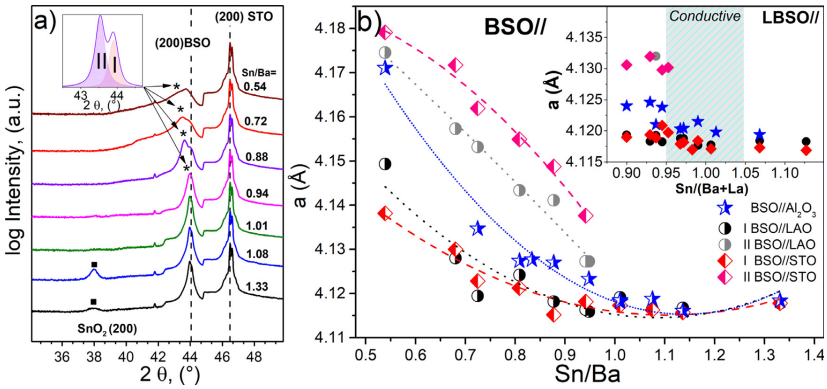

Fig. 2. Structural information of BSO films deposited at 850 °C with varying Sn/Ba ratio in the films: (a) XRD patterns thin BSO films deposited on STO substrates with Sn/Ba ratios ranging from 0.54 to 1.3. (■) marks SnO_2, (*) marks additional reflection unresolved from BSO (200). Inset: pseudo-Voigt fitting model, where I – BSO (200) reflection, II – additional unresolved reflection. (b) Pseudocubic lattice a parameter dependence on Sn/Ba ratio of thin BSO and LBSO films deposited on LAO, STO and Al_2O_3 substrates. BSO on Al_2O_3 lattice parameter was fitted using LeBail method [22]. Inset shows near-stoichiometric LBSO film lattice a parameter. The grey area represents a composition region of conductive LBSO films deposited on STO substrates.

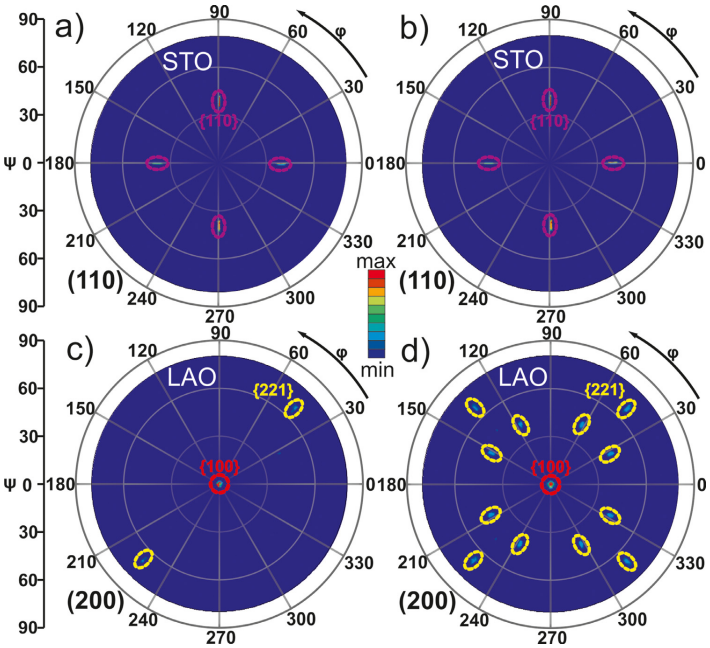

Fig. 3. (110), (200) Pole figures of thin BSO films deposited on STO, LAO substrates. (a, c) Pole figures of near-stoichiometric (Sn/Ba = 1.02). (b, d) Pole figures of Ba-rich film (Sn/Ba = 0.81).

substrates was determined. Although, different low-intensity signals of crystal orientation were detected for BSO samples on LAO substrates showing reflections of {221} crystal plane family. {221} reflections were well defined in films with higher barium content. Such orientation crystallites were clearly observed in film surfaces (Fig. 1d). It should be noted that detailed XRD analysis of near-stoichiometric and Ba-rich thin BSO films revealed no secondary phases in a wide range of composition. Furthermore, cubic symmetry was maintained significantly deviating from the ideal Sn/Ba ratio. This can be observed in either epitaxial and polycrystalline BSO thin films.

3.3. Undoped and La-doped $BaSnO_3$: comparison of morphology and phase composition

In order to compare doped and undoped film properties, a series of La-doped thin films were deposited on STO, LAO, and Al_2O_3 substrates. Films of different Sn/(Ba + La) ratios were obtained. La content was kept at a constant doping level (2.5 ± 0.2%$_{atomic}$) as determined by EDX analysis. XRD diffraction analysis in Bragg–Brentano and Schultz geometry configurations revealed that La-doped thin films were similarly epitaxial on both STO and LAO. Doping at small levels had no observable effect on the lattice parameter. Its dependence on Sn/(Ba + +La) ratio remained similar to undoped BSO films (Fig. 2, inset). Furthermore, XRD analysis of Ba-rich LBSO samples showed satellite (l00) peaks demonstrated in BSO. A clear lattice parameter increase was determined only in polycrystalline LBSO films on Al_2O_3. As La^{3+} ions radius ($R(La^{3+})$ = 1.36 Å) is smaller than Ba^{2+} ion radius ($R(Ba^{2+})$ = 1.61 Å) exchanging the A-site of ABO_3 perovskite structure would decrease the lattice parameter. However, only an increase of the unit cell was determined [39]. This phenomenon was known and explained by Sn^{4+} ion conversion into Sn^{2+} to maintain electric neutrality causing Sn–O bond extension. Similar results were demonstrated by Liu et al. [40].

To further investigate doping effects, both BSO and LBSO films deposited on STO substrates were investigated using scanning electron microscopy. In the case of Ba deficiency, BSO film surface was uneven and made of small-sized separate crystallites (Fig. 4a). Such film formation could be attributed to slower nucleation process and formation of islands. Near-stoichiometric (Sn/Ba = 1.02) BSO films were uniform and compact. Although, typically defined thread dislocations terminating at the surface were clearly visible [14]. In comparison, SEM images revealed different surfaces in case of Ba-rich composition. A uniform film matrix with protruding irregular faceted tetrahedral crystallites was observed. The density of these structural defects increased with the decreasing Sn/Ba ratio and could be attributed to increasing BSO/STO lattice mismatch and formation of (221) oriented crystallites.

LBSO films shown in Fig. 4d–f demonstrated very similar morphologies. Although a uniform and continuous film surface was achieved at Ba-rich compositions, films of Sn/(Ba + +La) = 0.97 were, in turn, the most conductive. This could be related to lower carrier scattering due to a lesser amount of visible grain boundaries and dislocation sites. The most uniform surfaces, on the other hand, were produced at slightly larger Sn/(Ba + +La) ratios (~0.90) which revealed a shift in the film composition corresponding to uniform surfaces. TEM cross-section images of the most uniform sample show columnar growth of the films typical for CVD methods [41]. It is important to notice that film is not uniform throughout its growth direction. In the Fig. 4g TEM image reveals two distinguishable growth regions: STO//LBSO interface followed by epitaxial layer and more defective morphology at film thickness higher than 70 nm. In HRTEM

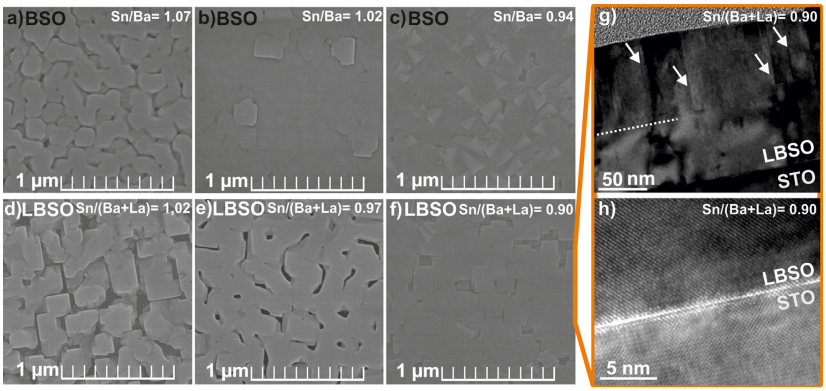

Fig. 4. Thin film, deposited on STO substrate, morphology: (a − c) SEM images of BSO film surfaces. (d − f) SEM images of LBSO film surfaces. Film composition corresponds to respective Sn/Ba (1.07; 1.02; 0.94), Sn/(Ba + +La) (1.02; 0.97; 0.90) ratios. Surface roughness determined using AFM: (a) 9.7 nm, (b) 3.79 nm, (c) 9.4 nm, (d) 27.4 nm, (e) 22.0 nm, (f) 5.1 nm. (g) TEM cross-section image of LBSO film along $[l00]_{STO}$ direction. Dotted white line separates the defective region above thickness of 70 nm. White arrows mark threading dislocations. (h) HRTEM image of epitaxial thin LBSO film-substrate interface.

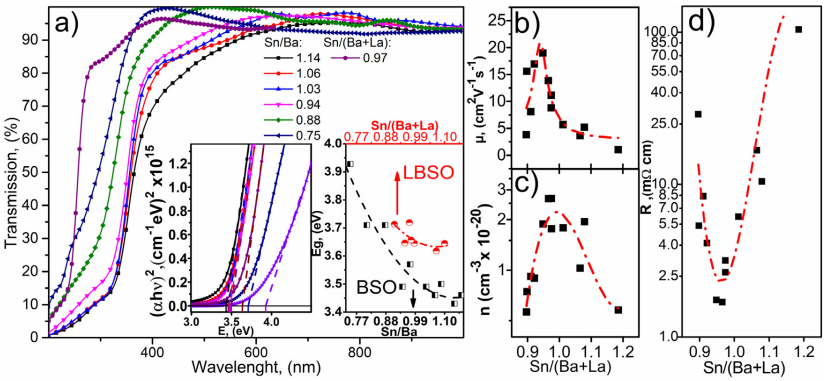

Fig. 5. Optical transmission of thin BSO and LBSO films deposited on (0006) Al_2O_3 substrates at different compositions. Left inset: Tauc plots of BSO and LBSO thin films. Right inset: band gap dependence on different BSO and LBSO film compositions. Electric properties of thin LBSO films: (b) carrier mobility (μ); (c) carrier density (n); (d) specific resistance (R).

image of film-substrate interface a well-oriented epitaxial film growth is demonstrated (Fig 4h). However, at a larger thickness region of ~70–170 nm, clearly visible threading dislocations have formed, seen as vertical contrasted lines. Dislocation formation is possibly the result of strain relaxation mechanism as lattice mismatch between film and the substrate is known to induce residual stress at similar interfaces.

3.4. Nonstoichiometry effect on optical and electric properties

Optical transmittance spectra of multiple thin BSO and LBSO films deposited on Al_2O_3 substrate were recorded (Fig. 5a). To clearly visualize the nonstoichiometry effect on optical properties distinctive data points are given. For BSO and LBSO films higher than 80% transmittance was achieved in the visible range. In the UV region, the absorption edge was highly dependent on film composition and shifted towards lower wavelengths as barium content increased. Calculated optical bandgap (E_g > 3.42 eV) values of near-stoichiometric films exceeded single crystal value of 3.33 eV [42] and increased further with higher Ba content. Resulting as-grown films could be affected by high-temperature growth conditions at low pressures generating point defects, such as oxygen vacancies. Optical bandgap representing the indirect transition from the valence to conduction band could also be linked to change in A–O and B–O bonding site characteristics, which could be attributed to ionized oxygen vacancy formation and chemical expansion of the unit cell [43]. Such a result is further supported by increasing lattice parameter tendency with increasing Ba content in the films. LBSO films showed similar E_g behavior, although an overall E_g was slightly shifted to higher energies indicating Burstein–Moss effect, observed in degenerate semiconductors (Fig. 5, right inset).

Hall measurements of thin LBSO films revealed that highest values of carrier mobility (20 $cm^2\ V^{-1}\ s)^{-1}$, as well as carrier density ($2.6 \times 10^{20}\ cm^{-3}$), were achieved at film composition corresponding to Sn/(Ba + +La) ratio of 0.97 (Fig. 5b, c). Carrier mobility is usually determined by film morphology. High values were determined in the sample Fig. 4e) of continuous channel-like flat morphology. Decreasing mobility in other samples (Fig. 4d, f, on the other hand, could be

attributed to emerging grain-like structure leading to increasing carrier scattering at multiple grain boundaries. In stoichiometric n-type LBSO films carrier density is mostly determined by La doping in A-site (La_{Ba}^{+}). In nonstoichiometric conditions with fixed La-doping level, an evident decrease of carrier density could be determined by two self-compensation mechanisms. In case of wide composition range conditions carrier compensation occurs by either V_{Ba}^{2-} (Sn/(Ba + +La) > 1) or by La_{Sn}^{-} (Sn/(Ba + +La) < 1) acceptor type defects (Fig. 5c). In addition, a slight mobility and carrier concentration shift toward Ba-rich composition could probably be related to increase of ionized oxygen vacancies in Ba-rich conditions. Highest carrier concentration and mobilities resulted in the lowest measured resistance of 1.75 mΩ cm.

4. Conclusions

In this study, thin film deposition of epitaxial thin BSO and LBSO films on by PI-MOCVD method was demonstrated. Deviation from the stoichiometry resulted in a drastic change in structural, optical, and electric properties. It was shown that the decrease in Sn/Ba and Sn/(Ba + +La) ratios in the deposited films resulted in an increase of lattice parameter and optical bandgap (E_g) for BSO and LBSO, respectively. Lowest resistance determined by high carrier mobility and concentration was achieved in the nonstoichiometric composition of LBSO films.

Declaration of Competing Interest

None.

Acknowledgments

Many thanks to the Research Council of Lithuania cordially for the support and provided funding to conduct this research. The funding was generously provided under Grant S-MIP-19-45.

References

[1] S. Ismail-Beigi, F.J. Walker, S.-W. Cheong, K.M. Rabe, C.H. Ahn, Alkaline earth stannates: the next silicon? APL Mater. 3 (2015) 062510.
[2] W.-J. Lee, H.J. Kim, J. Kang, D.H. Jang, T.H. Kim, J.H. Lee, K.H. Kim, Transparent perovskite barium stannate with high electron mobility and thermal stability, Annu. Rev. Mater. Res. 47 (2017) 391–423.
[3] J. Son, P. Moetakef, B. Jalan, O. Bierwagen, N.J. Wright, R. Engel-Herbert, S. Stemmer, Epitaxial SrTiO3 films with electron mobilities exceeding 30,000 $cm^2 V^{-1} s^{-1}$, Nat. Mater. 9 (2010) 482.
[4] A. Prakash, P. Xu, A. Faghaninia, S. Shukla, J.W. Ager Iii, C.S. Lo, B. Jalan, Wide bandgap BaSnO3 films with room temperature conductivity exceeding 104 S cm^{-1}, Nat. Commun. 8 (2017) 15167.
[5] U. Kim, C. Park, Y.M. Kim, J. Shin, K. Char, Conducting interface states at $LaInO_3$/$BaSnO_3$ polar interface controlled by Fermi level, APL Mater. 4 (2016) 071102.
[6] H.Y. Hwang, Y. Iwasa, M. Kawasaki, B. Keimer, N. Nagaosa, Y. Tokura, Emergent phenomena at oxide interfaces, Nat. Mater. 11 (2012) 103.
[7] S. Heo, D. Yoon, S. Yu, J. Son, H.M. Jang, Non-volatile ferroelectric control of room-temperature electrical transport in perovskite oxide semiconductor La:BaSnO3, J. Mater. Chem. C 5 (2017) 11763–11768.
[8] M. Wu, S. Yu, L. He, L. Yang, W. Zhang, High quality transparent conductive Ag-based barium stannate multilayer flexible thin films, Scientific Rep. 7 (2017) 103.
[9] H. Yun, K. Ganguly, W. Postiglione, B. Jalan, C. Leighton, K.A. Mkhoyan, J.S. Jeong, Microstructure characterization of $BaSnO_3$ thin films on $LaAlO_3$ and $PrScO_3$ substrates from transmission electron microscopy, Scientific Rep. 8 (2018) 10245.
[10] J. Shiogai, K. Nishihara, K. Sato, A. Tsukazaki, Improvement of electron mobility in La:BaSnO3 thin films by insertion of an atomically flat insulating (Sr,Ba)SnO_3 buffer layer, AIP Adv. 6 (2016) 065305.
[11] S. Raghavan, T. Schumann, H. Kim, J.Y. Zhang, T.A. Cain, S. Stemmer, High-mobility $BaSnO_3$ grown by oxide molecular beam epitaxy, APL Mater. 4 (2016) 016106.
[12] A. Prakash, P. Xu, X. Wu, G. Haugstad, X. Wang, B. Jalan, Adsorption-controlled growth and the influence of stoichiometry on electronic transport in hybrid molecular beam epitaxy-grown $BaSnO_3$ films, J. Mater. Chem. C 5 (2017) 5730–5736.
[13] H. Paik, Z. Chen, E. Lochocki, A.S. H., A. Verma, N. Tanen, J. Park, M. Uchida, S. Shang, B.-C. Zhou, M. Brützam, R. Uecker, Z.-K. Liu, D. Jena, K.M. Shen, D.A. Muller, D.G. Schlom, Adsorption-controlled growth of La-doped BaSnO3 by molecular-beam epitaxy, APL Mater. 5 (2017) 116107.
[14] U. Kim, C. Park, T. Ha, R. Kim, H.S. Mun, H.M. Kim, H.J. Kim, T.H. Kim, N. Kim, J. Yu, K.H. Kim, J.H. Kim, K. Char, Dopant-site-dependent scattering by dislocations in epitaxial films of perovskite semiconductor BaSnO3, APL Mater. 2 (2014) 056107.
[15] L. Weston, L. Bjaalie, K. Krishnaswamy, C.G. Van de Walle, Origins of n-type doping difficulties in perovskite stannates, Phys. Rev. B 97 (2018) 054112.
[16] A. Bartasyte, V. Plausinaitiene, A. Abrutis, T. Murauskas, P. Boulet, S. Margueron, J. Gleize, S. Robert, V. Kubilius, Z. Saltyte, Residual stresses and clamped thermal expansion in LiNbO3 and LiTaO3 thin films, Appl. Phys. Lett. 101 (2012) 122902.
[17] J.-P. Senateur, J. Lindner, F. Weiss, C. Dubourdieu, C. Jiménez, A. Abrutis, Application of pulsed injection MOCVD to the deposition of dielectric and ferroelectric oxide layers and superlattices, MRS Proc. 606 (2011) 33.
[18] R. Lukose, N. Zurauskiene, S. Balevicius, V. Stankevic, S. Keršulis, V. Plausinaitiene, R. Navickas, Hybrid graphene-manganite thin film structure for magnetoresistive sensor application, Nanotechnology 30 (2019) 355503.
[19] A. Abrutis, V. Plausinaitiene, A. Teiserskis, Z. Saltyte, V. Kubilius, A. Bartasyte, J.P. Sénateur, $YBa_2Cu_3O_{7-x}$ and $La_{1-x}Sr_xMnO_3$ thin films grown by pulsed injection MOCVD, J. Phys. IV 11 (2001) 215–219.
[20] A.S.D. Gogova, Y.A. Kuznetsova, A.F. Zatsepin, L.A. Mochalov, A. Nezhdanov, B. Szyszka, Lanthanum-doped barium stannate - a new type of critical raw materials-free transparent conducting oxide, Int. J. Adv. Appl. Phys. Res. 4 (2017) 1–8.
[21] S.A. Chambers, T.C. Kaspar, A. Prakash, G. Haugstad, B. Jalan, Band alignment at epitaxial $BaSnO_3$/$SrTiO_3$(001) and $BaSnO_3$/$LaAlO_3$(001) heterojunctions, Appl. Phys. Lett. 108 (2016) 152104.
[22] A. Le Bail, β-Ba3AlF9, a complex structure determined from conventional X-ray powder diffraction, J. Solid State Chem. 103 (1993) 287–291.
[23] S. Yu, D. Yoon, J. Son, Enhancing electron mobility in La-doped BaSnO3 thin films by thermal strain to annihilate extended defects, Appl. Phys. Lett. 108 (2016) 262101.
[24] S.N. Ruddlesden, P. Popper, New compounds of the K2NIF4 type, Acta Crystallogr. 10 (1957) 538–539.
[25] B. Pödör, Electron mobility in plastically deformed germanium, Physica Status Solidi (b) 16 (1966) K167–K170.
[26] W.Y. Wang, Y.L. Tang, Y.L. Zhu, J. Suriyaprakash, Y.B. Xu, Y. Liu, B. Gao, S.W. Cheong, X.L. Ma, Atomic mapping of Ruddlesden-Popper faults in transparent conducting $BaSnO_3$-based thin films, Scientific Rep. 5 (2015) 16097.
[27] Y. Li, L. Zhang, Y. Ma, D.J. Singh, Tuning optical properties of transparent conducting barium stannate by dimensional reduction, APL Mater. 3 (2015) 011102.
[28] U. Gebhardt, N. Kasper, A. Vigliante, P. Wochner, H. Dosch, F. Razavi, H.U. Habermeier, Formation and thickness evolution of periodic twin domains in manganite films grown on $SrTiO_3$ (001) substrates, Phys. Rev. Lett. 98 (2007) 096101.
[29] C.Z. Chen, C.B. Cai, Z.Y. Liu, L. Peng, B. Gao, F. Fan, Y.M. Lu, R. Zeng, Z.P. Guo, W.X. Li, S.X. Dou, Stress evolution and lattice distortion induced by thickness variation and lattice misfit in $La_{0.67}Sr_{0.33}MnO_{3-\delta}$ films, Solid State Commun. 150 (2010) 66–69.
[30] H. Wei, M. Jenderka, M. Grundmann, M. Lorenz, LaNiO3 films with tunable out-of-plane lattice parameter and their strain-related electrical properties, Physica Status Solidi (a) 212 (2015) 1925–1930.
[31] Y.Z. Wang, E. Bevillon, A. Chesnaud, G. Geneste, G. Dezanneau, Atomistic simulation of pure and doped $BaSnO_3$, J. Phys. Chem. C 113 (2009) 20486–20492.
[32] S. Lany, A. Zunger, Assessment of correction methods for the band-gap problem and for finite-size effects in supercell defect calculations: case studies for ZnO and GaAs, Phys. Rev. B 78 (2008) 235104.
[33] A. Janotti, C.G.V.d. Walle, Oxygen vacancies in ZnO, Appl. Phys. Lett. 87 (2005) 122102.
[34] F. Oba, A. Togo, I. Tanaka, J. Paier, G. Kresse, Defect energetics in ZnO: a hybrid Hartree-Fock density functional study, Phys. Rev. B 77 (2008) 245202.
[35] A.K. Singh, A. Janotti, M. Scheffler, C.G. Van de Walle, Sources of electrical conductivity in SnO_2, Phys. Rev. Lett. 101 (2008) 055502.
[36] J.B. Varley, J.R. Weber, A. Janotti, C.G.V.d. Walle, Erratum: "Oxygen vacancies and donor impurities in β-Ga2O3" [Appl. Phys. Lett. 97, 142106 (2010)], Appl. Phys. Lett. 108 (2016) 039901.
[37] P. Ágoston, C. Körber, A. Klein, M.J. Puska, R.M. Nieminen, K. Albe, Limits for n-type doping in In_2O_3 and SnO_2: a theoretical approach by first-principles calculations using hybrid-functional methodology, J. Appl. Phys. 108 (2010) 053511.
[38] S. Miyoshi, J.-O. Hong, K. Yashiro, A. Kaimai, Y. Nigara, K. Kawamura, T. Kawada, J. Mizusaki, Lattice expansion upon reduction of perovskite-type $LaMnO_3$ with oxygen-deficit nonstoichiometry, Solid State Ionics 161 (2003) 209–217.
[39] R.D. Shannon, Revised effective ionic radii and systematic studies of interatomic distances in halides and chalcogenides, Acta Crystallogr. A 32 (1976) 751–767.
[40] Q. Liu, J. Liu, B. Li, H. Li, G. Zhu, K. Dai, Z. Liu, P. Zhang, J. Dai, Composition dependent metal-semiconductor transition in transparent and conductive La-doped BaSnO3 epitaxial films, Appl. Phys. Lett. 101 (2012) 241901.
[41] R. Lukose, V. Plausinaitiene, M. Vagner, N. Zurauskiene, S. Kersulis, V. Kubilius, K. Motiejuitis, B. Knasiene, V. Stankevic, Z. Saltyte, M. Skapas, A. Selskis, E. Naujalis, Relation between thickness, crystallite size and magnetoresistance of nanostructured $La_{1-x}Sr_xMnyO_{3\pm\delta}$ films for magnetic field sensors, Beilstein J. Nanotechnol. 10 (2019) 256–261.
[42] K. Hyung Joon, K. Useong, K. Hoon Min, K. Tai Hoon, M. Hyo Sik, J. Byung-Gu, H. Kwang Taek, L. Woong-Jhae, J. Chanjong, K. Kee Hoon, C. Kookrin, High mobility in a stable transparent perovskite oxide, Appl. Phys. Express 5 (2012) 061102.
[43] R.U. Chandrasena, W. Yang, Q. Lei, M.U. Delgado-Jaime, K.D. Wijesekara, M. Golalikhani, B.A. Davidson, E. Arenholz, K. Kobayashi, M. Kobata, F.M.F. de Groot, U. Aschauer, N.A. Spaldin, X. Xi, A.X. Gray, Strain-engineered oxygen vacancies in $CaMnO_3$ thin films, Nano Lett. 17 (2017) 794–799.

Vilniaus universiteto leidykla
Saulėtekio al. 9, LT-10222 Vilnius
El. p. info@leidykla.vu.lt, www.leidykla.vu.lt
Tiražas 20 egz.